

INDEX-ANTIGUIDED PLANAR WAVEGUIDE LASERS WITH LARGE MODE
AREA

by

Yuanye Liu

A dissertation submitted to the faculty of
The University of North Carolina at Charlotte
in partial fulfillment of the requirements
for the degree of Doctor of Philosophy in
Optical Science and Engineering

Charlotte

2017

Approved by:

Dr. Tsing-Hua Her

Dr. Michael A. Fiddy

Dr. M. Yasin Akhta Raja

Dr. Stuart T. Smith

ABSTRACT

YUANYE LIU. Index-antiguided planar waveguide lasers with large mode area. (Under the direction of DR. TSING-HUA HER)

The on-going research and application interests with high power large-mode-area (LMA) waveguide lasers, especially in fiber geometry, at the beginning of this century drive the development of many novel waveguide designs. Index antiguiding, proposed by Siegman in 2003, is among one of them. The goal for index antiguiding is to introduce transversal modal loss with the relative simple waveguide design while maintain single transverse mode operation for good beam quality. The idea which is selectively support of fundamental mode is facilitated by involving certain level of signal regeneration inside the waveguide core. Since the modal loss is closed associated with waveguide design parameters such as core size and refractive index, the amount of gain inside the core provides active control of transverse modes inside index-antiguiding waveguide. For example, fundamental transverse mode inside such waveguide can be excited and propagate lossless when sufficient optical gain is provided. This often requires doped waveguide core and optical pumping at corresponding absorption band.

However, the involvement of optical pumping also has its consequences. Phenomena such as thermal-optic effect and gain spatial hole-burning which are commonly found in bulk lasers request attention when scaling up output power with LMA index-antiguided waveguide amplifiers and resonators. In response, three key challenges of index-antiguided planar waveguide lasers, namely, guiding mechanism, power efficiency and transverse mode discrimination, are analyzed theoretically and experimentally in this dissertation. Experiments are based on two index-antiguided planar waveguide chips,

whose core thickness are 220 μm and 400 μm respectively. The material of waveguide core is 1% Neodymium-doped Yttrium Aluminium garnet, or Nd:YAG while the cladding is made from Terbium Gallium garnet, or TGG.

Due to the face pumping and limited pump power, it is found, with 220 μm -thick-core chip, that the guidance of the fundamental transverse mode along two orthogonal directions in a transverse plane is different. Along the bounded direction, index antiguiding prevails with negligible thermal refractive focusing while along the unbounded direction, the lasing mode is guided by thermal refractive focusing with negligible quadratic gain focusing. It is also founded that the quadratic thermal focusing will dominate the mode guidance in 220 μm chip with the help of additional pump. All these discovery calls for an active thermal control.

The modal discriminative loss, though beneficial for transverse mode control, yet reduces the lasing efficiency. To model it, a 3-D lasing output power calculation model is developed based on spatial rate equations. The simulation results show good agreement with experiment data where slope efficiency curve are measured using multiple output couplers. The 10% slope efficiency with respect to incident pump power is the highest slope efficiency recorded in index-antiguided waveguide continuous-wave lasers. The model indicates more efficient pump absorption can facilitate further power scaling.

The role of the modal discriminative loss in transverse mode competition is discussed. A theoretical model based on Rigrod analysis and spatial hole-burning is developed. The simulation shows reasonable agreement with experiment results in both chips. The single fundamental mode operation up to 10 times above the lasing threshold for 220 μm chip is achieved, which is limited by the incident pump power. However, as

the core size increases, the modal distributed loss due to the index antiguiding is found to be less effective in transverse mode control. Other modal loss is needed to facilitate the suppression of higher-order modes. Based on the model, a strategy is proposed aiming to maximize the single mode output. It is also noted that the transverse mode competition model is also suitable for other lasers system with well-defined modal loss.

Based on the models and experiment data, the index-antiguided planar waveguide lasers are proved to be capable of maintaining large-mode-area single transverse mode operation with the potential of power scaling. However, it is also shown that proper waveguide design is essential. The remaining challenges are the material choices for waveguide fabrication, especially for high power applications.

DEDICATION

To my wife and parents

ACKNOWLEDGEMENTS

It is not an easy decision for me to make at 2011 to apply for graduate school oversea since it is not a prevailing career trajectory for a MS graduate in China, especially at that time I had already been offered a job. It is certainly not possible to finish this 5 years' journey without support from my parent. Though many things have changed over the last five years, their endless support endows me and I am forever grateful for their encouragement of pursuing my research interests. I also would like to thank my wife Yang Yang who is right now in Shanghai. Without your generous love, I will not achieve what I had done today.

I am also extremely lucky that I met Dr. Tsing-Hua Her at UNC Charlotte when I firstly arrived. His patience and wisdom steered me through difficult time during these years, for what I am forever grateful. I would like to express my gratitude to Dr. Lee Casperson who inspired and encouraged me pursuing truth beyond the misleading appearance. His profound knowledge in lasers provides valuable support on models discussed in this dissertation. I would like to express my gratitude to many of my friends met in US, Dr. Tao Sheng, Mr. Mark Green, Dr. Henan Liu and Dr. Jinghua Ge. Without your help, I will be lost in this foreign land. I would also like to thank Mr. Kang Ni. I really enjoy white board discussion with you on multidisciplinary topics. Finally, thanks to all my friends and colleagues in Physics and Optical Science department for their help and supports.

TABLE OF CONTENTS

LIST OF TABLES	xii
LIST OF FIGURES	xiii
CHAPTER 1 INTRODUCTION	1
1.1 Dielectric planar waveguide lasers	1
1.1.1 Introduction.....	1
1.1.2 Fabrication of dielectric planar waveguide.....	3
1.1.3 Pump scheme	5
1.1.4 Spatial mode selection	6
1.2 Large-mode-area waveguide.....	7
1.2.1 LMA design	7
1.2.2 Historical review	9
1.3 Outline of this dissertation	11
CHAPTER 2 EXPERIMENT SETUPS AND LASING EXPERIMENT RESULTS	13
2.1 Introduction.....	13
2.2 Index-antiguided planar waveguide chips	13
2.3 Experiment setups.....	16
2.4 Characterization	20
2.4.1 Lasing spectrum.....	21
2.4.2 Transverse mode	22
2.4.3 Longitudinal mode	27
2.4.4 Polarization	32
2.4.5 Beam quality factor.....	37

2.5 Summary	40
CHAPTER 3 MODE GUIDANCE INSIDE FACE PUMPED INDEX-ANTIGUIDED PLANAR WAVEGUIDE LASER.....	
3.1 Introduction.....	41
3.2 Index antiguiding	42
3.2.1 Complex $\tilde{\nu}$ number	43
3.2.2 Fundamental mode.....	46
3.2.3 High-order modes	49
3.3 Hyper guiding inside index-antiguided planar waveguides.....	52
3.3.1 Gain profile	52
3.3.2 Thermal profile	55
3.3.3 Lens-like media.....	60
3.4 Fundamental mode inside hyper guided IAG planar waveguide laser	63
3.4.1 Bounded direction.....	64
3.4.2 Unbounded direction.....	70
3.4.3 Quadratic modal loss.....	74
3.5 Summary	75
CHAPTER 4 POWER CALCULATION BASED ON SPATIAL RATE EQUATIONS	
4.1 Introduction.....	77
4.2 Theory.....	78
4.2.1 Spatial rate equation.....	79
4.2.2 Intracavity intensity	81
4.2.3 Output power calculation.....	83
4.3 Experiment results and discussion	86

	x
4.3.1 Pump absorption	86
4.3.2 Pump spatial profile	88
4.3.3 Lasing profile	89
4.3.4 Output power and efficiency	91
4.4 Summary	95
CHAPTER 5 TRANSVERSE MODE COMPETITION INSIDE INDEX-ANTIGUIDED WAVEGUIDE LASER	97
5.1 Introduction	97
5.2 Coupling loss in waveguide laser	99
5.2.1 General theory	99
5.2.2 Coupling loss in planar waveguide lasers	101
5.2.3 Coupling loss in cylindrical IAG fiber lasers	103
5.3 Transverse mode competition	105
5.3.1 Theory	105
5.3.2 TMC simulation and experiment results	115
5.4 Performance optimization	122
5.4.1 Performance matrix	123
5.4.2 Performance simulation	124
5.5 Summary	129
CHAPTER 6 CONCLUSION AND FUTURE WORK	131
6.1 Conclusion	131
6.2 Future work	132
REFERENCE	135
APPENDIX A SCANNING FABRY PEROT INTERFEROMETER	149

A.1.1 Introduction.....	149
A.1.2 Principle	150
A.1.3 Setups	151
A.1.4 Instrumental response curve.....	153

LIST OF TABLES

Table 2-1. Physical parameters for the core and cladding material for IAG planar waveguide chips.....	14
Table 2-2. Dimension of the chips and coating information.....	15
Table 2-3. Instrument parameters of the home-built confocal scanning FPI.....	30
Table 3-1. Parameters used in heat transfer simulation.....	57
Table 3-2. Parameters and corresponding value used for simulation.....	68
Table 4-1. Physical parameters used in rate equation.....	80
Table 4-2. Parameters used to solve Eq. (4.18).....	92
Table 5-1. Parameters used before solving the CDEs.....	113
Table 5-2. Parameters used in the 220 μm chip experiment.....	115
Table A-1. Specification of the home-built SFPI.....	155

LIST OF FIGURES

Figure 1-1. Schematic of disk, rod and fiber geometry.....	1
Figure 1-2. Schematic of planar waveguide.....	2
Figure 1-3. Schematic of pump arrangements for planar waveguides.....	5
Figure 2-1. Dimension and orientation definition.....	15
Figure 2-2. Animated experiment setup for IAG planar waveguide lasers.....	18
Figure 2-3. Pictures of experiments setup.....	18
Figure 2-4. Schematic diagram of pump beam delivery path.....	19
Figure 2-5. The measured amplified spontaneous emission (ASE) spectral with 808.5 nm incident pump.....	21
Figure 2-6. Measured lasing spectrum with 0.9 reflectivity output coupler.....	21
Figure 2-7. Schematic diagram of the near-field imaging.....	23
Figure 2-8. Typical measurement results of the near-field modes.....	24
Figure 2-9. Near-field intensity profiles along the x -axis and y -axis.....	25
Figure 2-10. Typical far-field mode for 220 μm chip.....	26
Figure 2-11. Far-field intensity profiles along x -axis and y -axis.....	26
Figure 2-12. Schematic diagram of the home-built scanning FPI.....	28
Figure 2-13. Transmittance of the confocal FPI.....	28
Figure 2-14. Schematic of experiment setup for scanning FPI.....	30
Figure 2-15. Measurement results of the longitudinal mode structure inside the IAG planar waveguide lasers.....	32
Figure 2-16. Schematic of experiment setup for the PER measurement.....	34
Figure 2-17. The transmitted intensity for a linear polarized laser beam at different rotation angle of PBS.....	34
Figure 2-18. PER at different lasing power for 220 μm chip.....	36

Figure 2-19. Schematic of experiment setup for M^2 measurement.....	38
Figure 2-20. M^2 measurement results.....	38
Figure 2-21. M^2 at different lasing power.....	39
Figure 3-1. Schematic illustration of the waveguide structure of IAG planar waveguide.....	43
Figure 3-2. Values for possible \tilde{w} parameters for lowest order mode.....	47
Figure 3-3. The allowed value of \tilde{u}	48
Figure 3-4. The allowed u_r of a given ΔN for the lowest order mode.....	49
Figure 3-5. Complex $\tilde{\sigma}^2$ plane and the boundaries of the modal order.....	50
Figure 3-6. Temperature distribution in transverse plane.....	58
Figure 3-7. Temperature profiles along bounded and unbounded directions.....	59
Figure 3-8. Index profile of IAG planar waveguide including thermal induced refractive index variation.....	59
Figure 3-9. The typical values of t at given w_x in the unit of a	65
Figure 3-10. Intensity profile of fundamental mode along the bounded direction with different w_x	65
Figure 3-11. The intensity FWHM of fundamental mode at given $\sqrt{2 \ln 2} \cdot w_x$	67
Figure 3-12. Near-field mode intensity profiles at lasing threshold and maximum lasing power.....	68
Figure 3-13. The intensity profiles cross-section along the x -axis at $P_{ab} = 0.5W$ and $P_{ab} = 5.75W$	69
Figure 3-14. The contour plot of $w_y \cdot (\beta_0)^{0.25}$	72
Figure 3-15. The contour plot of $R_y / (\beta_0)^{0.5}$	73
Figure 3-16. Experiment result of intensity profile along the y -axis together with calculation results with only α_{2y} , only β_{2y} and both α_{2y} and β_{2y}	74

Figure 4-1. Face-pumped planar waveguide chip used in the modeling.....	79
Figure 4-2. Lasing spectral of pump diode at 44.0A inject current and 24.0 C.....	87
Figure 4-3. Absorption coefficient (cm^{-1}) of 1% Nd:YAG crystal.....	88
Figure 4-4. Pump spatial profiles along (a) y -axis and (b) z -axis.....	89
Figure 4-5. Intensity profile at 2.0W lasing power with $R_{oc} = 0.95$ output coupler.....	90
Figure 4-6. Experiment data and simulation results for lasing power at different incident pump power with a variety of OC.....	93
Figure 5-1. Schematic drawing of the free space diffraction.....	100
Figure 5-2. Schematic drawing of mode diffraction after leaving the waveguide facets.....	102
Figure 5-3. Calculated $(1 - \Gamma)$ at different gap distance for IAG planar waveguide chips with core thickness of 220 μm and 400 μm	103
Figure 5-4. Calculated $(1 - \Gamma)$ at different gap distance for IAG fibers with 200 μm , 300 μm and 400 μm core diameter.....	104
Figure 5-5. Schematic of the plane-parallel laser resonator.....	105
Figure 5-6. Schematic for power evolution inside a laser resonator.....	107
Figure 5-7. Transverse mode overlap with gain media for FM and 1st HOM.....	112
Figure 5-8. Schematic diagram of strategy for solving coupled ODEs.....	114
Figure 5-9. The near-field mode pictures and intensity profiles along the x -axis at the mode centroid for 0.02W and 2.45W lasing power.....	116
Figure 5-10. Measured and simulated output for 220 μm chip with $R_{oc} = 0.9$	116
Figure 5-11. Measured and simulated output for 400 μm chip with $R_{oc} = 0.9$	118
Figure 5-12. The near-field mode pictures and intensity profiles along the x -axis at the mode centroid at a variety of lasing power.....	120
Figure 5-13. Modal ratio versus output for $R_{oc} = 0.7$ and $R_{oc} = 0.9$	121
Figure 5-14. Near-field mode profile along the x -axis with cosine square fitting.....	122

Figure 5-15. Typical simulation results by solving the CDEs.....	124
Figure 5-16. Simulation results for TGR, I_{\max} and η_{extr} in 1-D planar waveguide.....	125
Figure 5-17. Simulation results for TGR, I_{\max} and η_{extr} in fiber.....	126
Figure 5-18. Residual spatial gain profile for 1 st HOM in region II for 1-D IAG planar waveguide.....	127
Figure A-1. The transmission curve of the FPI in frequency domain.....	150
Figure A-2. Schematic diagram of the home-built SFPI.....	151
Figure A-3. Scanning setup configuration of SFPI.....	152
Figure A-4. The scanning triangle wave and transmitted intensity signal.....	153
Figure A-5. Individual instrument response spike measured with ECL.....	154
Figure A-6. Scanning ranges at different scanning p-p voltage.....	155

CHAPTER 1 INTRODUCTION

1.1 Dielectric planar waveguide lasers

1.1.1 Introduction

Since the invention in 1960s, lasers have been transformed from “toys” in laboratory to “labor” in industrial by on-going efforts of increasing the output power and efficiency. Among all types of lasers, solid-state lasers have experienced significant improvement in terms of output power at the beginning of this century. Largely due to the advance of infrared semiconductor lasers as pump source [1], continuous-wave solid-state lasers with 1 W to 2 kW output power have been routinely demonstrated in rod, slab and disk geometries [2, 3]. To further increase the output power, temperature and propagation loss need to be properly managed. There are two major approaches to achieve this goal: optical fiber and thin disk, the schematic of which are shown in Fig. 1-1.

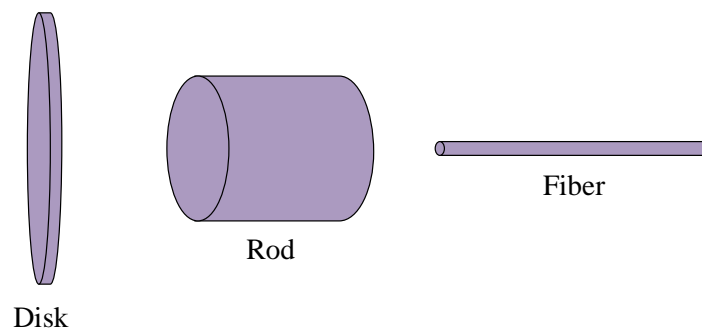


Figure 1-1. Schematic of disk, rod and fiber geometry.

For the former one, the length of the rod-shape gain media is reduced to several hundred micro meters, which is referred as thin-disk laser [4]. The interaction length between gain media and laser signal is short. Such short distance renders the thermal optical effects along the optical direction irrelevant. However, it also reduces the single-pass pump absorption leading to a low single-pass gain. Sophistic pump beam path design is required to solve this issue. Another design is to prolong the rod. With the help of waveguide effect, low loss propagation is possible in optical fibers where the doped core can be as long as 1 km [5]. The interaction between gain media and lasing signal, in fiber geometry, is substantially longer than in disk geometry. The dielectric planar waveguide is, however, combining both fiber and disk design: provide optical confinement along one transverse direction while remaining thin along another transverse direction.

Conventional step-index dielectric planar waveguide is illustrated in Fig. 1-2. As illustrated, 3 layers of material are used. Typically, the center layer formed by optical denser material is referred as waveguide core while two surrounding layers formed by optical rarer material are referred as waveguide cladding. The guiding effect provided by the total internal reflection tends to confine light signal inside the core.

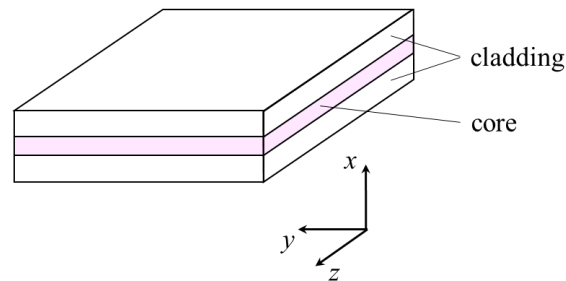


Figure 1-2. Schematic of planar waveguide.

When the core is doped and properly pumped, optical amplification of certain wavelength is achieved. The spatial overlap between pump and lasing profile due to optical confinement helps to increase the gain, promising a high power efficiency. The large surface to volume ratio helps to conduct heat towards the heat sinks which is commonly attached to the cladding surface.

In this dissertation, the dielectric planar waveguide is used as gain media and optical confinement platform for lasing study. In combination of novel guiding technology, namely index antiguiding, the planar waveguide laser is assembled with plane-plane cavity and continuous-wave (CW) lasing is achieved. Output power, lasing modes are analyzed theoretically and experimentally.

1.1.2 Fabrication of dielectric planar waveguide

The fabrication methods of dielectric planar waveguide are grouped into two categories: attach or grow two dissimilar material and induce refractive index variation of bulk material [6, 7].

Techniques used for crystal growth have been applied to the fabrication planar waveguides. Lasing operation based on planar waveguides which are fabricated by epitaxial growth methods such as liquid phase epitaxial (LPE) [8], vapor phase deposition using pulsed laser deposition (LPD) [9] and molecular beam epitaxial (MBE) [10] have been demonstrated. The major advantage for such techniques is the capability to grow single crystalline structures. The optical loss is sequentially smaller than its polycrystalline relatives [6]. Meanwhile, the single crystalline structure inherently provides good thermal conductivity, benefiting the laser operation and power scaling effort. Chemical vapor deposition, for example plasma enhanced chemical vapor deposition (PECVD) [11, 12], is

also reported for planar waveguide fabrication. However, the choice of the waveguide material is limited to particular combinations [12], limiting waveguide design. Physical methods, for example sputter [2, 3], are also reported to fabricate dielectric waveguides.

Another method for waveguide fabrication is based on already growth material, such as contact bonding [13-16] and diffusion bonding [17]. The idea for these methods are to use van der Waals' force to hold core and cladding together. To achieve good bonding, the contact surface needs to be treated to have excellent surface finish. Such requirement increases fabrication tolerance on polishing and cleaning processes. Compared with previously mentioned epitaxial growth methods, contact and diffusion bonding can provide both large core size (up to 200 μm) waveguides and low optical loss with smaller cost [18-20].

Besides, optical waveguides can also be fabricated by alternating the refractive index inside a bulk material. Methods such as ion-exchange [21, 22] and thermal ion indiffusion [23, 24] are proved to be effective to fabricate waveguides in doped crystalline material and glass material respectively. Following the on-growing interests in material processing, femtosecond laser written waveguides are demonstrated with most of the prevailing gain media such as Nd:YAG [25], Nd:YVO₄ [26] and Yb:YAG [27].

Among all these methods, material bonding is widely used to fabricate large core-size planar waveguides for lasing operation, the reason of which can be briefly summarized as follow. Firstly, the typical refractive index step for waveguides fabricated with crystal growth methods is around 10^{-3} whereas the bonding methods are capable of fabricating waveguides with refractive index step as large as 0.1 [28]. Large refractive index increase the numerical aperture (NA), which is crucial when collecting divergent pump laser

(usually diode bar or strips). Secondly, even though the planar geometry itself is beneficial for heat management, the cladding material needs to possess excellent thermal properties in order to effectively remove residual heat for high power applications. It is possible that the material choices for the core and cladding prevent the usage of any crystal growth methods. For large-core-size waveguides in particular, the bonding methods are more flexible than the material growth methods.

1.1.3 Pump scheme

Optical pump is the only feasible approach to excite the solid-state amplifiers and lasers. Thanks to the rapid development of semiconductor lasers around infrared region, the efficiency and output power of solid-state lasers undergo rapidly development while cost drops dramatically. There are 3 pumping arrangements to efficiently excite the planar waveguide with a doped core as shown in Fig. 1.3.

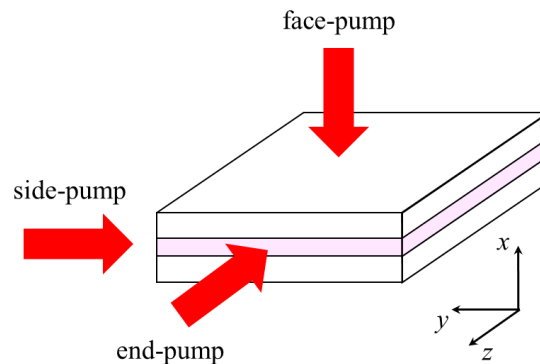


Figure 1-3. Schematic of pumping arrangements for planar waveguides. The red arrows indicate the direction of the pump light. The lasing takes place along the z -axis.

Both end and side pumping are referred as in-plane pumping. The pump irradiance from a laser diode, in either bar or strip geometry, is coupled into waveguide core by cylindrical lens or simply by proximity coupling. Both pump irradiance and lasing signal

are confined by the waveguide. The interaction between pump and lasing is thus enhanced, promising a large gain and optimized power efficiency [28-31].

For face pumping, on the other hand, the waveguide does not provide any guidance for pump irradiance. The unabsorbed pump radiance needs to be recycled in order to increase the absorption. For example, a custom designed chamber is effective in trapping the pump radiance [19]. With its help, the CW operation of a 400 μm -thick waveguide lasers was achieved with 150 W output power and 35% optical efficiency.

1.1.4 Spatial mode selection

In-plane pumping requires the NA of the waveguide to be large for effectively coupling pump laser into the core, resulting in a multimode waveguide design in the bounded direction. For the unbounded direction, there is no other mechanism to guide the lasing signal, leading to the multimode operation as well. Consequently, the output beam quality deteriorates when increasing the pump power. Facing with this challenge, various spatial mode control methods have been proposed. A brief summary is given in this section.

The double cladding structures, where an additional pair of cladding are introduced, are used [32, 33] for spatial mode selection. The structure is inherently multimode and the doped core locates only in the central region of the waveguide. Different spatial modes experience different gain due to the overlap between pump profile and lasing profile in a given transverse plane. However, the refractive index difference between the inner and outer cores should be kept below the level at which the new waveguide is formed.

Another technique referred as self-imaging is reported to successfully control the spatial mode along the bounded direction [34, 35]. Since the optical beam with certain spatial profile will reimage itself periodically after propagating a fixed distance inside the

step-index waveguide. As long as the waveguide is properly designed, this technique enables single fundamental mode operation of waveguide lasers with core size up to a few hundred micron meters [36, 37], which is one order of magnitude larger than what double cladding structure provides [28]. The conditions for latching the pump and alignment are yet critical for self-imaging waveguides. Extensive effort in cavity alignment is therefore required.

The external cavity design also provides spatial mode control for waveguide lasers whose core size can be as large as 200 μm . The waveguide modes tend to diffract in the region between cavity mirrors and waveguide facets. The diffraction is associated with modal orders [38, 39] and is used to selectively maintain single fundamental mode along both bounded and unbounded directions [18, 40] while suppress all other modes.

1.2 Large-mode-area waveguide

The confinement of light increase the optical intensity for signals inside the core. This is the case for single mode waveguide whose core size is on the order of 10 μm level. When optical power is high enough, nonlinear optical effects are triggered inside the waveguide core [25]. In fact, custom designed waveguide structures are able to provide low nonlinear threshold on purpose for effects such as second harmonic generation (SHG) [41, 42] and self-phase modulation (XPM) [26], which may be impractical otherwise. To increase the output power, however, nonlinear optical effects need to be mitigated and one of the approaches is employing large-mode-area (LMA) waveguide.

1.2.1 LMA design

Due to the rapid increasing of output power in cylindrical waveguide lasers, namely fiber lasers [43], most of the LMA waveguide designs are in fiber geometry, such as

photonic crystal fibers (PCF) [27], leakage channel fibers (LCF) [22] and large pitch fibers (LPF) [21]. The design goal of these waveguides is to maintain single fundamental transverse mode operation for excellent output beam quality, while increasing waveguide core size to reduce optical intensity. LMA designs are loosely grouped into two categories: increase modal propagation loss and delocalize modes.

The easiest way to facilitate fundamental mode operation while suppressing higher-order modes is to coil multimode step-index fibers. The conventional step-index fibers are subject to minimal NA which is 0.06 [23] imposed by the manufacturing process. The modal loss induced by bending helps strip out higher-order modes through cladding coupling [44]. It is, however, with the cost of distorted fundamental mode profile.

The fiber can also be designed such that higher-order modes possess substantially higher propagation loss than the fundamental mode [45]. Examples can be found in air-hole photonic crystal fibers [46, 47]. The geometrical arrangement of the air-hole in the transverse plane determines propagation characteristics of certain transverse modes. It provides flexibility in fiber design while sacrifices the level of ease in fabrication. The operation of photonic crystal fiber lasers is reported to be very efficient [46]. The slope efficiency for some cases is approaching the quantum defect efficiency indicating the extremely low loss [24].

Another fiber design capable of providing modal discrimination is leaky channel fibers (LCF) [13]. The fiber is made from solid core with one layer of large air or solid holes. The destroyed total internal reflection (TIR) due to the gap between holes imposes propagation loss on all modes. Similar as PCF, the geometrical arrangement of holes is used to design the propagation loss [22].

Besides introducing loss to suppress higher-order modes, coupling them into cladding or other axillary structures also help facilitating single fundamental mode operation in LMA fibers. The representative for this design methodology is chirally-coupled-core (CCC) fibers. The helical satellite cores wrapping around the main fiber core [8], stripping higher-order modes once angular momentum conservations condition is met [48]. Commercial products aiming at industrial application based on 55 μm -diameter-core CCC fibers are available [14, 17]. The idea that higher-order modes are not located inside the core is referred as modal delocalization.

Another method to delocalize higher-order modes is LPF [49]. The core design is similar as PCFs [50]. The spacing between adjacent holes is larger than their own diameters, leading to large penetrating of higher-order modes field into holed region. This design is widely used in femtosecond amplifiers [6, 10, 21], due to its excellent capability of reducing the pulse peak intensity. In addition, methods such as gain filtering [51] and tapped fibers [11] are also capable of supporting fundamental mode in LMA fibers.

Extending the idea of increasing modal loss, index-antiguinding is firstly proposed by Siegman in 2003 [52], where refractive index of the core is smaller that of the cladding. Similar as LPF, all the modes propagating inside index-antiguinded (IAG) waveguide are leaky. It has been reported that such structure, with the help of gain in the core, supports fundamental mode operation with up to 400 μm -diameter core [53].

1.2.2 Historical review

The theoretical background for IAG waveguides were proposed in 2003 [52]. It has been proved theoretically that a waveguide having larger refractive index in the cladding together with positive gain in the core region (doped material with proper excitation) is

able to support confined propagation modes. It was also referred as gain-guiding, index-antiguidded (GG-IAG) in literatures. Large-mode-area and single fundamental mode operation can be achieved by balancing the gain and loss.

First experiment demonstration of IAG fiber was done in 2006 by researchers in CREOL [54]. The fiber core was made from Neodymium (Nd) doped phosphate glass (Kigre Q100, 10% w.t.), with the core diameter of 100 μm . The excitation method was chosen to be flash pumping to avoid thermal fracture. The far-field imaging showed a round and Gaussian shape intensity profile at pump power several times above threshold. Together with a small M^2 parameter, it was determined that confined propagation of single fundamental mode is possible in IAG structure.

First IAG fiber laser was demonstrated in 2007 [55]. Different planar output couplers, together with a fixed planar higher reflector, has been used in the experiments [53]. Due to its large core size, effort was devoted to cavity alignment. Otherwise, the oscillation of parasitic modes would prevail, deteriorating output beam quality. Single fundamental mode operation has been demonstrated with 200, 300 and 400 μm -diameter-core IAG fibers.

To further improve the output power, flash lamp pumping is replaced by diode pumping. However, thermal failure was found in end pumping scheme [56], forcing pump diode lasers working in quasi continuous-wave (QCW) mode. Even though face pumping and 200 W diode arrays were used [57], reported IAG fiber lasers have to be operated in gain switching mode.

Beside conventional step-index fiber, double cladding 200 μm -diameter-core IAG fibers were also manufactured using conventional fiber drawing technique [58, 59]. The

dopant was chosen to be Ytterbium (Yb) which is widely used in high power laser oscillators and amplifiers. A D-shape inner clad design was used in the effort to increase the absorption of pump power. Experiment observation showed, however, roughly 1% amplification efficiency with Gaussian shape beams spot. Theoretical modeling of output power and efficiency of IAG fiber lasers and amplifiers were carried out [60-63]. The results suggested that multipoint distributed pumping and tapered cladding were effective in terms of avoiding the thermal failure and increasing power efficiency respectively. However, no direct experiment results echo the theoretical calculation.

In conclusion, index-antiguinding in cylindrical waveguides have been proved to be capable of supporting single fundamental mode operation with a core diameter around hundreds of micro meters. In addition, it has been proved that the thermal effects need to be managed properly for further improvement of output power. It is also clear that the continuous-wave lasing has never been reported. The theoretical calculations reinforced by experimental observations were seldom reported.

1.3 Outline of this dissertation

Facing with these challenges, the goal of the this dissertation is to provide theoretical models as well as direct experiment verifications in mode guidance, output power, lasing efficiency and transverse mode competition inside face-pumped IAG planar waveguide lasers. Following the introduction, the rest of this dissertation is organized as follows. Chapter 2 focuses on the experiment setups and characterization methods used for further analysis. Detail procedures about experiment are also recorded. Chapter 3 details the mode guidance inside a continuous wave IAG planar waveguide lasers both theoretically and experimentally. The waveguide is treated as hybrid guided structure since

the guidance along bounded and unbounded direction are different. Along the bounded direction, thermal refractive focusing and index antiguiding are considered while gain refractive focusing and thermal refractive focusing are considered along the unbounded direction. Chapter 4 covers the theoretical modeling of output power based on spatial rate equations. The model is applied to the face-pumped IAG planar waveguide laser with continuous wave output. The output power and slope efficiency results with a variety of output couplers are covered. In chapter 5, a theoretical model describing transverse mode competitions inside the IAG planar waveguide lasers is developed. Experiments based on two IAG waveguide chips are used to verify the theory. Conclusions and outlooks are presented in chapter 6.

CHAPTER 2 EXPERIMENT SETUPS AND LASING EXPERIMENT RESULTS

2.1 Introduction

The foundation of all models and experiments in this dissertation is the IAG planar waveguide lasers. Before approaching to detail discussions on unique features of the IAG waveguide lasers, the experiment setups and the output characterization methods are introduced in this chapter. The laser output characterization results including spontaneous and lasing spectral, transverse and longitudinal modes, polarization and beam quality factors are discussed, aiming to exam the general output characteristics of IAG planar waveguide lasers.

This chapter is organized in the following way: In section 2.2, the index-antiguided planar waveguide chips used in this dissertation are introduced. In section 2.3, the experiment setups are detailed followed by the laser output characterization results in section 2.4. In section 2.5 conclusion remark is made.

2.2 Index-antiguided planar waveguide chips

For IAG planar waveguides used in this dissertation, the material of the waveguide core is 1% doped Neodymium-doped Yttrium Aluminum garnet (Nd:YAG) while the cladding material is Terbium Gallium garnet (TGG). The physical parameters for these two materials are listed in table 2-1.

Many methods have been developed to join the waveguide core and cladding together as discussed in chapter 1. Aiming for excellent waveguide quality, diffusion bonding is chosen due to the small deviation of the lattice constants for these two material. The bonding process includes the following processes: polishing, heating, contacting and slowly ramping down the temperature while staying fixed by the designed fixture. The exact recipe is proprietary to the manufacturer (Northrop Grumman SYNOPTICS).

Table 2-1. Physical parameters for the core and cladding material of IAG planar waveguide chips (courtesy of Adam Dittli)

Item	Nd:YAG	TGG
Formula	$Y_{2.97}Nd_{0.03}Al_5O_{12}$	$Tb_3Ga_5O_{12}$
Crystal Structure	Cubic [1,1,1]	Cubic [1,1,1]
Melting Point	1950° C	1725° C
coefficients of thermal expansion (CTE)	$7.8 \times 10^{-6} K^{-1}$	$9.4 \times 10^{-6} K^{-1}$
Lattice Constant	12.01 angstroms	12.347 angstroms

There are two waveguide chips with different dimension used in the experiments, which are fabricated through the same processes. The dimension of the two chips are given in table 2-2 and geometrically illustrated in Fig. 2-1.

Table 2-2. Dimension of the chips and coating information

	Chip 1	Chip 2
Core thickness	220 μm	400 μm
Length	19.8 mm	15.5 mm
Width	11.0 mm	5.4 mm
Thickness	2.4 mm	3.2 mm
Surface A, B	808 nm AR	808 nm AR
Surface C, D	Grounded	Grounded
Surface E, F	1064 nm AR	1064 nm AR

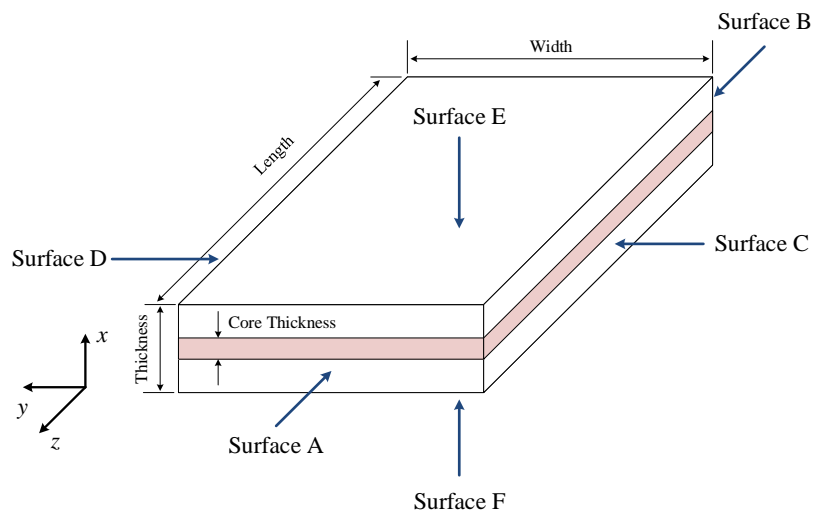


Figure 2-1. Dimension and orientation definition.

Surface irregularity of surface of A and B is 10-5 scratch dig and the parallelism is smaller than 30 arc second. The surface irregularity specification is 1 wave @ 632.8nm, a scratch-dig specification of 60-40 and a parallelism of 30 arc second. The other surfaces are optical grounded. It is noted that the optical coatings of both chips were deposited separately from

the chip fabrication process but with the chip manufacturer.

2.3 Experiment setups

The experiment setup consists of pump delivery, cooling assembly and cavity mirrors. A fiber coupled diode laser (Apollo F100) is used as the pump source. The nominal center wavelength is 808.2 nm with maximal 100 W nominal output power at 25 degree C. However, it is observed in the experiment that the pump wavelength is effected by the injection current and the cooling temperature. To insure the stable lasing, therefore the efficient pumping, the diode laser is water cooled to 16 degree C while the injection current is fixed to be 44.0 A throughout all the experiments. The thermal equilibrium inside the diode leads to a stabilized temperature of 24.5 degree C read from the diode driver. A small fluctuation of ± 0.2 degree C is observed overtime (within 2 hours) due to the fluctuation of the cooling water and the lack of close-loop feed-back temperature control. The corresponding center wavelength drift is determined to be around 0.1 nm. The output of the pump diode laser is coupled into a multimode fiber. A fiber collimator is used to expand and collimate the pump beam from the fiber end. The pump beam exiting the fiber collimator is estimated to have a diameter of 0.5 inches (full width at null).

Due to the grounded surface D and C, the only available pump configurations are end-pumping and face-pumping. For efficient end-pumping, the pump beam has to be compressed and collimated along both the bounded and unbounded direction with the beam diameter close to the thickness of the waveguide core. This adds complexity to the beam shaping and risks to reduce the pump beam transmission since more optics are involved. Alternatively, face-pumping only requires to shape the pump beam into a line along the z -axis. Besides, the focused line shape pump footprint provides the possibility to guide the

mode in the unbounded direction, which is promising for good beam quality along both bounded and unbounded directions. For the purpose to demonstrate lasing, face-pumping is chosen in this dissertation. The major disadvantage is, however, that the length of the interaction between pump and gain media is limited to the thickness of the waveguide core. Detail analysis of the power absorption is shown in chapter 4 since it plays a crucial role in determining lasing efficiencies.

The simulated the experiment setup is shown in Fig. 2-2 and the picture of the real setup is shown in Fig. 2-3. The schematic diagram of pump beam delivery path is shown in Fig. 2-4. Two mirrors, high reflectors M1 and M2, are used to direct the collimated pump beam towards the waveguide chip. The incident pump power is tuned by rotating a half-wave plate (HWP, zero order) sandwiched by two polarization beam splitters (PBS) while the chiller temperature and injection current of the pump diode is fixed. To avoid thermal failure, the PBSs are individually placed on cooling blocks. The temperature of these cooling blocks are actively maintained to be 15 degree C. The reflected linear polarized beam from PBS1 is dumped into a metal black box for safety. The optical power of the reflected beam from PBS2 is measured by a power meter (Coherent LM45), which provides pump power monitoring. The cubic nature of Nd:YAG crystal makes its absorption isotropic. Therefore, it is believed that the polarized pump light will not affect the absorption. The transmitted pump beam after PBS2 is shaped by a telescope formed by a planar-concave lens (-75mm focal length, L1) and a planar-convex lens (150 mm focal length, L2). The pump spot after L2 is estimated to be 1 inch (full width at null), which is observed using an IR card. A cylindrical lens (CYL) focuses the pump beam onto the chip with a footprint of a line along the z -axis. The intensity profile along the footprint is shown

in chapter 4.

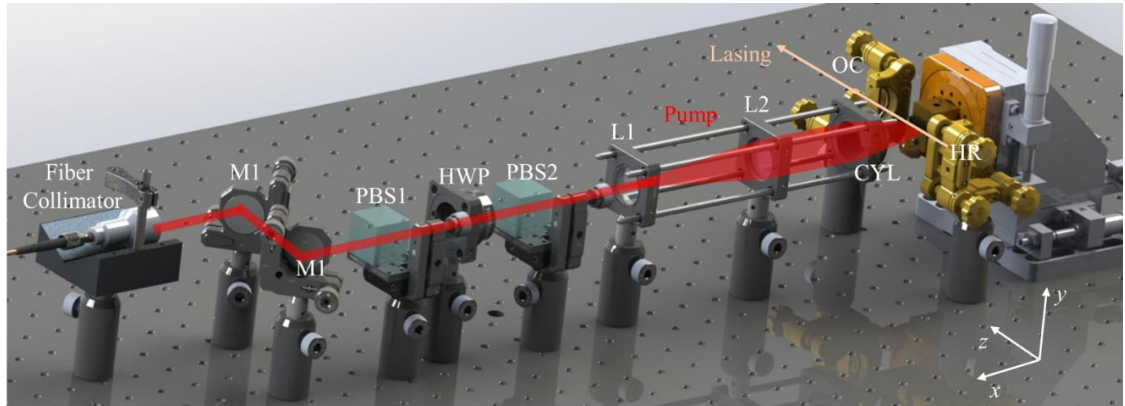


Figure 2-2. Animated experiment setup for IAG planar waveguide lasers. M1 and M2: 808 nm high reflectors; PBS: polarization beam splitter; HWP: 808 nm half wave plate; L1: 75 mm plane-concave lens; L2: 150 mm plane-convex lens, CYL: cylindrical lens; OC: output coupler; HR: 1064 nm high reflector.

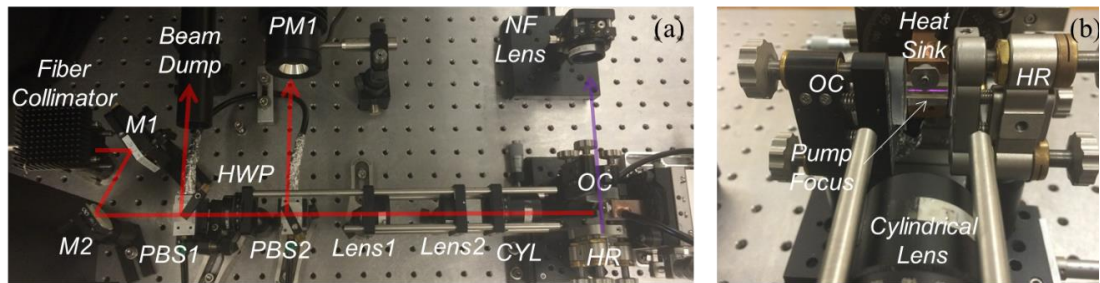


Figure 2-3. Pictures of experiments setup. (a) Overall experiment setups and (b) the zoom in of the IAG chip and the pump footprint.

To remove deposited heat during lasing, the IAG chip is mounted on a custom-made copper cooling block which is actively cooled to 15 degree C. A 100- μ m-thick Indium foil is placed between the chip and the cooling block. The foil provides both soft contact to prevent surface scratch due to the mounting and excellent thermal conductivity

for heat removal. The unabsorbed pump irradiance is reflected back towards the waveguide core due to the foil. Even though the actual reflectivity varies with respect to locations on the foil and the shape of the incident beam, the reflectivity of the foil is determined to be close to 1. Gradually oxidation of the foil is found experimentally since the color the foil becomes white after frequently changing the IAG chips for experiments. Further improvement of the experiment setups are made by fixing the IAG waveguides and Indium foil with a custom made copper sheet. In this way, the IAG waveguide does not have to be removed from the foil when switching the chips. The assembly is then mounted onto the cooling block with thermal paste in between. In this way, the exposure of the air is minimized.

One high reflector and one output coupler are used as the cavity mirrors, which forms the plane-parallel cavity. To successfully get lased, two plane mirrors need to be precisely aligned parallel. A low power red diode laser is used to assist the cavity alignment. The detail procedures for cavity alignment are listed as follow. First of all, the beam height of the laser setups are determined according to the focused pump footprint. Every optics

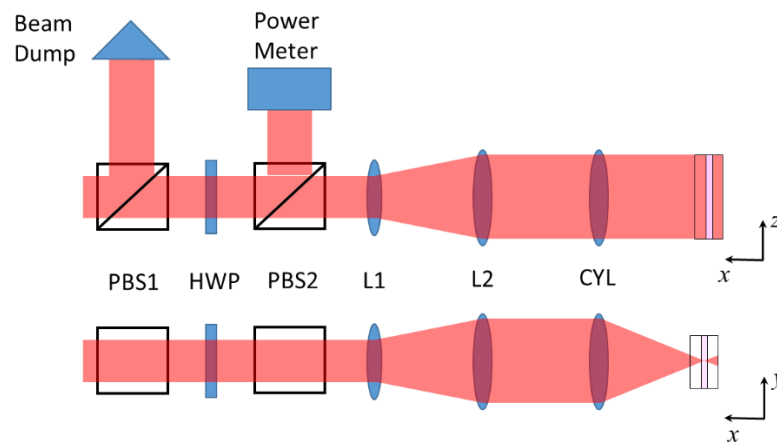


Figure 2-4. Schematic diagram of pump beam delivery path

on the table is set to be at this height. The red alignment laser is then aligned to be parallel to the optical table using two irises and two mirrors. Place an iris near the high reflector which serves as the target pinhole. Secondly, place the IAG waveguide chip and output coupler to their positions shown in Fig. 2-3. Align all the reflections back to the center of the target iris. Finally, place output coupler at the location shown in Fig. 2-3 and align the reflection of it back to the target iris. At this stage, the cavity alignment should be good enough for lasing when moderate pump power is used. Further cavity optimization can be achieved by fine tuning two cavity mirrors in the effort to maximize the output lasing power. It worth noting that as mentioned in optical IAG fiber laser cases [53, 64], the lasing can also be achieved with randomly transverse intensity pattern, or parasite modes. The highest output power at a fixed pump power is achieved by carefully aligning the cavity mirrors for round and symmetric output intensity pattern. The mechanical mount for two cavity mirrors are recommended to be stable kinematic mount with precision screws.

2.4 Characterization

After achieved lasing, the general characterization of the output is discussed in this section. The data discussed in section is based on the results of 220 μm IAG chip. Despite the size difference, the general laser output behavior of two IAG chips are similar. Difference in experiment results between two chips will be mentioned when necessary. In section 2.4.1, the spectral below and above lasing threshold is shown. The transverse and longitudinal mode of IAG planar waveguide laser is discussed in section 2.4.2 and 2.4.3 respectively. In section 2.4.4, the polarization properties represented by the polarization extinction ratio is discussed, followed by the beam quality factors.

2.4.1 Lasing spectrum

The lasing spectral is measured by a fiber coupled grating based spectrometer (Avantes), the resolution of which is 0.1 nm. The measured amplified spontaneous

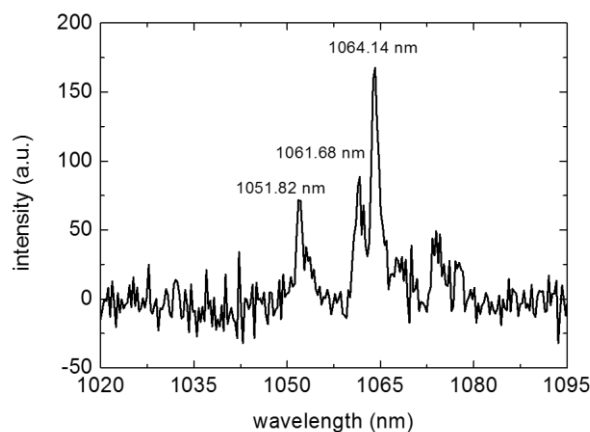


Figure 2-5. Measured amplified spontaneous emission (ASE) spectral with 808.5 nm incident pump. The spectrum shows peaks at 1051.82 nm, 1061.68 nm and 1064.14 nm.

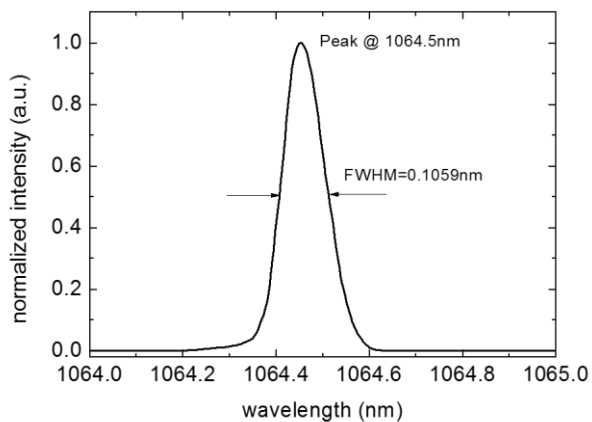


Figure 2-6. Measured lasing spectrum with 0.9 reflectivity output coupler. The FWHM is 0.1059 nm.

emission (ASE) below lasing threshold is shown in Fig. 2-5 while the measured lasing spectral is shown in Fig. 2-6. The ASE spectrum is consistent with the reported data [65].

It is however with the maximal incident pump power, the ASE spectrum for 400 μm chip shows several peaks around 870 nm and 885 nm. These peaks disappear in the output spectrum once lasing is achieved, indicating the possible presence of excited state absorption with substantially high pumping power. The lasing spectrum does not change its shape throughout the span of the available pump for both chips.

2.4.2 Transverse mode

The transverse mode of the laser refers to the electromagnetic field in the plane perpendicular to the propagation axis (z -axis in Fig. 2-1), which can reproduce itself after travelling around trip along bounded direction. The formation of transverse modes are the results of optical cavity and certain intensity patterns are used to quantify the specific order of transverse modes. Since the plane-plane cavity is used, transverse modes inside IAG planar waveguide lasers are effected by the waveguide instead of laser cavity. Therefore, the mode field profiles in the x - y plane are used in this dissertation to represent the corresponding transverse mode of IAG planar waveguide lasers. The rigorous waveguide mode is the solution to the wave equation with rectangular boundary condition. Since the refractive index in IAG waveguide is large enough to preclude itself from the assumption of weakly guiding waveguides, the transverse mode is not degenerated in terms of propagation constant. However, intensity profiles of transverse mode are more relevant in characterizing lasing action considering the gain saturation. The intensity profiles of each transverse mode are also used in this dissertation to describe the transverse mode.

There are two methods used in this dissertation to analyze the transverse mode, namely near-field imaging and far-field imaging. The corresponding measured field profiles are referred as near-field mode and far-field mode respectively. The near-field

mode intensity profiles are measured by imaging the lasing spots of the IAG chip facet onto the beam profiler (WinCamD) as shown in Fig. 2-7. To achieve this, a plano-concave lens whose focal length is 50 mm is placed on a translation stage for focus adjustment.

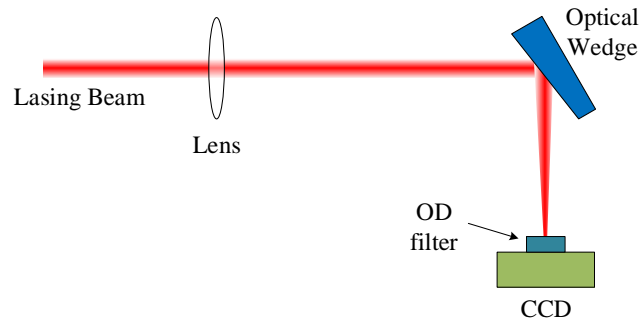


Figure 2-7. Schematic diagram of the near-field imaging. To avoid the damage, an optical wedge is used to pick up a portion of power for imaging.

To avoid saturation at high lasing power, an optical wedge and an absorptive neutral density filter (OD 4.0 in total) are used to sample the lasing beam for imaging. In addition, a long-pass filter (LPF) with 1000 nm cut-off wavelength filters out the unnecessary wavelength. The measured intensity profile for near-field modes are shown in Fig. 2-8.

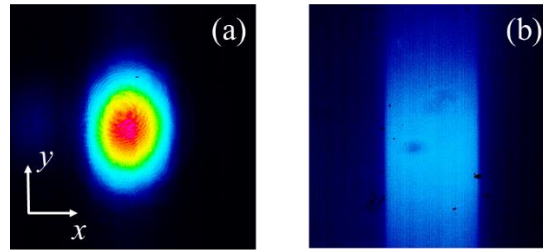


Figure 2-8. Typical measurement results of the near-field modes for (a) above lasing threshold (0.36 W output power) with 0.3 reflectivity output coupler and (b) below lasing threshold. The dark dots scattering around the image corresponds to the dirt or dust on the optical surface.

Below the lasing threshold, typical near-field profile shows two sharp vertical strips corresponding to the material interfaces of waveguide core and cladding. The illuminated core is due to the confined amplified spontaneous emission, or ASE. This feature provides a convenient way to adjust the imaging lens to affirm focusing location. It also helps to calibrate the pixel on the captured near-field intensity profile since the illuminated ASE represents the thickness of the waveguide core. Once focus is set, the setup is ready to take measurements. When measuring the laser operation around maximal pump power, a variable reflectivity neutral density filter ring is used to further attenuate the lasing beam. This helps to maintain long integration time for the beam profiler to capture and display the intensity profile accurately.

Above the lasing threshold, the near-field image shows a symmetric pattern with the peak intensity at its center. In order to get this mode, one has to adjust the cavity mirrors very carefully similar as what was reported in reference [53]. For further analysis, the intensity profiles along two orthogonal lines (along the x -axis and y -axis), the interception

of which is the centroid of the near-field image are extracted out and saved. Examples are plotted in Fig. 2-9.

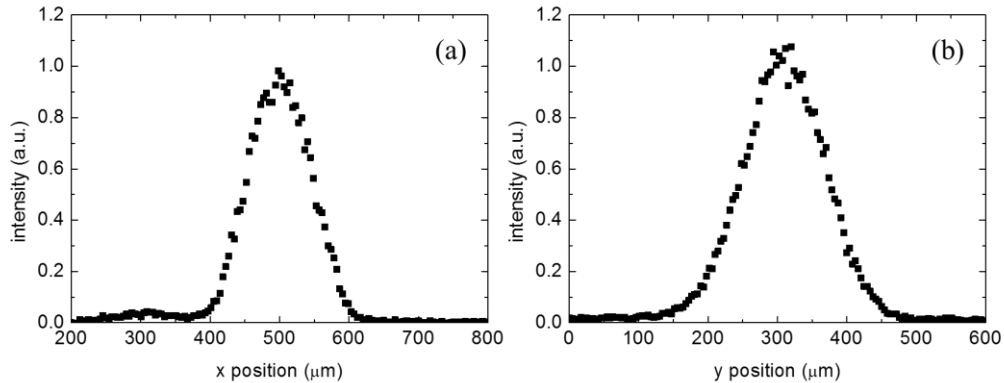


Figure 2-9. Near-field intensity profiles along the (a) x -axis and (b) y -axis.

Extensive analysis are made based on near-field imaging in the following chapters. It is important to note that the near-field mode behaves differently for two IAG chips when pump power is increased. It can be summarized briefly as follows: For 220 μm chip, the intensity profiles along the bounded direction and unbounded direction remain their shapes which are illustrated in Fig. 2-9 (a) and Fig. 2-9 (b) respectively throughout all the pump process as long as the cavity is well aligned. Before the chips were AR coated, higher-order modes along the unbounded direction were observed since there was an obvious dip at the center of the output intensity profile. Following experiments showed this dip disappeared after AR coating was deposited. For 400 μm chip, however, the intensity profile along the bounded direction becomes flat in the center when lasing power was increased. Eventually, a dip appears in the center which is believed due to the presence of first higher-order mode.

Detail discussion on the near-field mode evolution will be detailed in chapter 5 together with mathematical modeling.

Besides the near-field imaging, far-field imaging is also used to observe the transverse mode. Other than near-field imaging, far-field imaging is used to determine the mode structure indirectly. Due to the free-space propagation, the measured intensity profile is the Fourier transform of the near-field lasing mode. Inverse Fourier transform algorithm is needed to retrieve near-field mode profile. This approach is widely used for small core

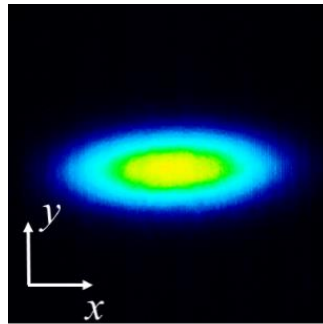


Figure 2-10. Typical far-field mode for 220 μm chip. The measurement is taken with 0.9 reflectivity output coupler while the lasing power is 0.5 W.

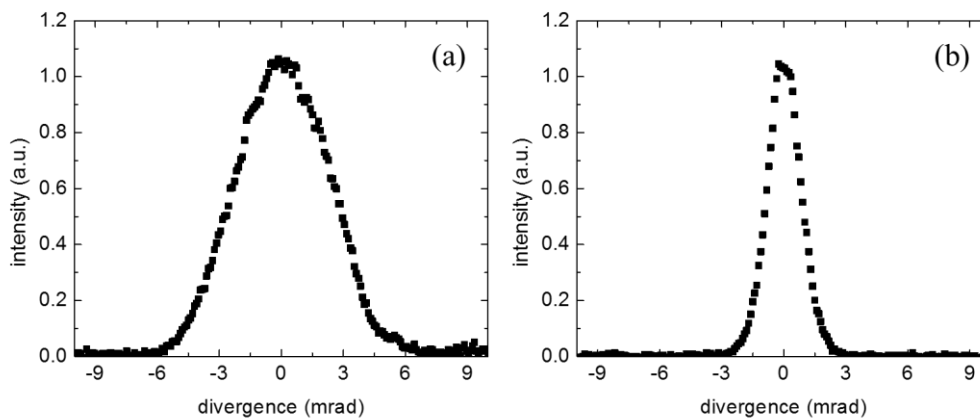


Figure 2-11 Far-field intensity profiles along (a) x -axis and (b) y -axis

waveguides and fibers where large magnification objectives are needed for near-field imaging [66]. Since near-field imaging discussed above provides good imaging of the lasing mode, far-field imaging is treated as the auxiliary method for lasing mode observation in the experiments. The schematic diagram of the far-field imaging is similar as shown in Fig. 2-7 but without the imaging lens. The distance between the chip facet and the beam profiler is fixed to be 200 mm. The typical far-field intensity profile is given in Fig. 2-10 while the intensity profiles along the two orthogonal directions (x -axis and y -axis) are given in Fig. 2-11. Due to the optical confinement along the bounded direction, the far-field intensity profile along the bounded direction, due to the finite aperture imposed by waveguide core, shows large beam divergence when compared with its near-field counterpart. However for the unbounded direction, the lasing beam does not diverge as severe as it does along the bounded direction. It is determined partially due to the unbounded nature such that no hard aperture involved in beam propagation.

2.4.3 Longitudinal mode

The longitudinal mode of a laser resonator is the standing wave pattern along the optical axis, which can resonate inside the laser cavity. The longitudinal modes are characterized by the equally spaced peaks in frequency domain. To resolve them, the grating based spectrometer is not appropriate due to its limited resolution. Interferometry method, namely, scanning Fabry-Perot interferometry (FPI) is used instead. Though several commercial scanning FPIs are available, yet the low resolution around 1 μm region precludes them from being used to correctly interpret the longitudinal modes inside the IAG planar waveguide lasers. A scanning FPI is built to address this issue. The detail description and test results for this scanning FPI can be found in Appendix A. Brief

introduction and the summary is mentioned in this section.

The schematic diagram of the scanning FPI is shown in Fig. 2-12. The cavity is chosen to be confocal (mirror separation equals the radius of curvature of the cavity mirrors) in order to avoid transverse mode excited longitudinal modes [67]. Two identical plano-

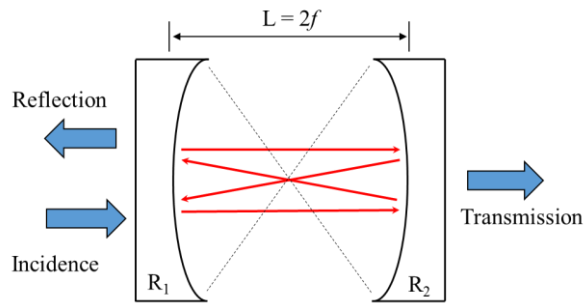


Figure 2-12. Schematic diagram of the home-built scanning FPI.

concave mirrors with high reflectivity ($> 99.8\%$) at $1 \mu\text{m}$ region serve as the cavity mirrors.

Without scanning, the transmittance of the confocal FPI is illustrated in Fig. 2-13. The

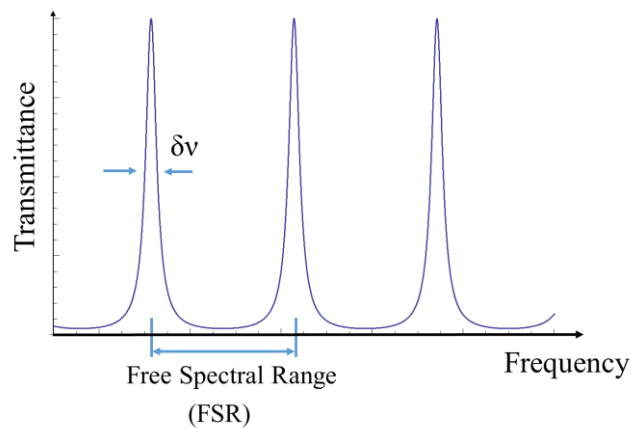


Figure 2-13. Transmittance of the confocal FPI.

period sharp high transmittance spikes are described by two parameters: free spectral range (FSR) and FWHM of single transmittance spike ($\delta\nu$).

For confocal resonator, the FSR is given by $FSR = c / 4L$ where c is the vacuum speed of light and L is the separation between two mirrors (often referred as cavity length).

FSR and $\delta\nu$ are related through finesse (\mathcal{F}) of the FPI through $\delta\nu = FSR / \mathcal{F}$. \mathcal{F} is related

with the reflectivity of the mirrors R through $\mathcal{F} = \pi\sqrt{R} / (1 - R)$ when $R > 0.5$ is met. The

influence of the cavity design parameters (R and L) on the spectral response can be

summarized as follows: FSR is determined by the mirror separation while the \mathcal{F} is

determined by the reflectivity of cavity mirrors. $\delta\nu$ is determined when FSR and \mathcal{F} are set.

By changing d , the transmission peaks of a FPI is tuned across the spectral of interest. The

transmitted intensity corresponds to the convolution between unknown spectral density and

the transmittance curve of the FPI. A transmittance curve, due to high reflectivity of cavity

mirror, can be approximated to be a delta function in spectral domain. The scanning of d

is then treated as sampling through the unknown spectral. The spectral profile of the light

source under test is therefore measured by recording the transmitted intensity correlated

with cavity spacing. If the scanning range is large enough such that two adjacent

transmission peaks of FPI sampled through the same spectral profile, two identical spectral

profiles will be recorded from the detector. The separation between these two identical

profiles is the FSR of the scanning FPI. This provides the self-calibration for the

measurement. The parameters associated with the home-built confocal scanning FPI is

given in table 2-3

The schematic diagram of the longitudinal mode measurement setup based on the home-built scanning FPI is given in Fig. 2-14. Two high reflectors (M1 and M2) are used

Table 2-3. Instrument parameters of the home-built confocal scanning FPI

Parameter	Value
Reflectivity of cavity mirror	> 99.8% @ 1064 nm
Mirror separation	50 mm
FSR	1.5 GHz
Mirror Finesse	784.6
Calculated $\delta\nu$	2 MHz
Measured $\delta\nu$	4 MHz
Scanning Rate	8.69 GHz/V

to direct the output lasing beam towards the FPI. A plane-convex lens (150 mm focal length, L1) is used to condense the diverted beam due to the propagation. A 100 × objective couples the laser beam into the coiled single mode fiber (SMF), the length of which is 10

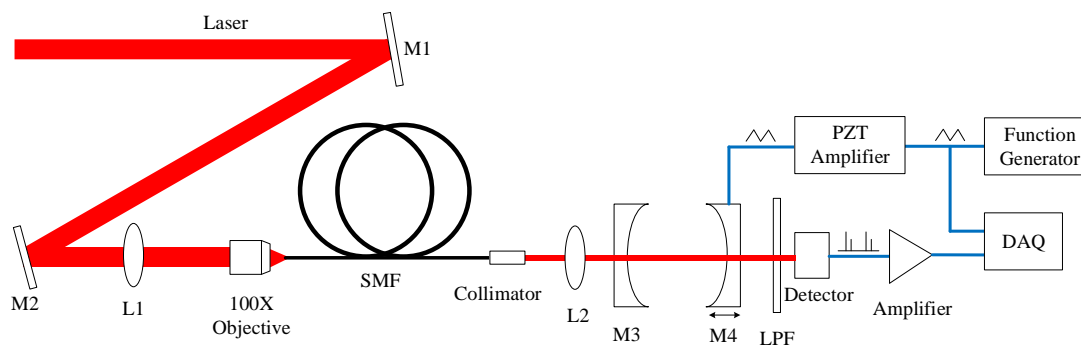


Figure 2-14. Schematic of experiment setup for scanning FPI.

meters. A fiber collimator and another lens (250 mm focal length, L2) are used to couple the light into the scanning FPI.

SMF serves as the spatial filter which helps shaping the laser beam. The shaped beam insures an efficient coupling of lasers output into the FPI. Even though, it is found experimentally that coupling light into the SMF suffers from the low coupling efficiency. Experiment data suggests approximated 20% of lasing power is coupled into the SMF. One of the FPI cavity mirrors is placed on a piezo controlled translation stage while the other mirror is fixed on the same stage. A saw tooth signal generated by function generator is applied to achieve scanning. The scanning rate for the FPI is calibrated to be 8.69 GHz/V using an ultra-narrow linewidth single longitudinal mode diode laser (Thorlabs TLK1060, linewidth 100kHz @ 1064 nm). The transmitted intensity signal from the FPI is measured by a PIN photodiode with a long pass filter (LPF, cut-off wavelength 1 μm). The output of the PIN and the saw tooth voltage are captured with the NI data acquisition card (DAQ).

The longitudinal mode measurement results are shown in Fig. 2-15. The results show clear repetitive structures with the period of 1.5 GHz which corresponds to the FSR of the FPI. Within one FSR, there are 6 major peaks with relatively equal separation. However, the absolute value of the peak intensity is not the same. The measured average FWHM is 8.2 MHz corresponding to 0.03 pm around 1 μm region. The result shows the longitudinal modes from IAG planar waveguide lasers is unstable. This is due to the possibility of spectral overlap since the FSR of the FPI is smaller than that of the IAG laser (estimated to be 4.1 GHz). The measurement results shown in Fig. 2-15 is only 37% of the FSR for the IAG lasers. In addition, the environment of the FPI is not precisely controlled, which adds to the measurement uncertainty. Since there is no apparatus other than the

cavity mirrors inside the IAG laser cavity, it is believed the measured spectral can represent the features of the longitudinal mode structure. Current FPI can be configured such that the

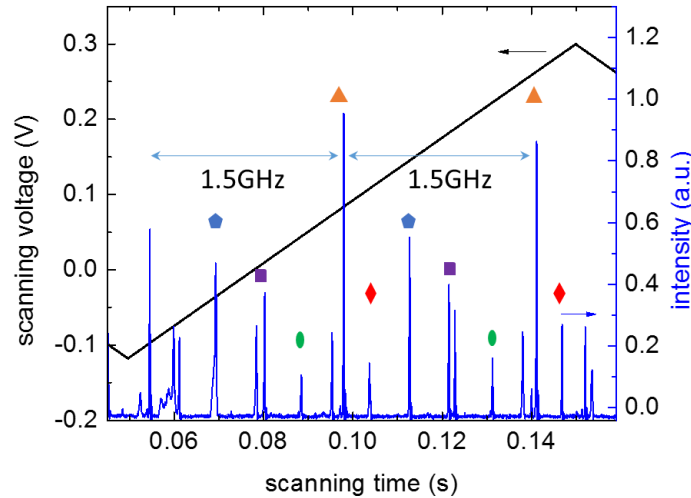


Figure 2-15. Measurement results of the longitudinal mode structure inside the IAG planar waveguide lasers. The result shown here is measured with 220 μm chip, 0.9 reflectivity output coupler and 2.4W lasing power. The horizontal axis represents 0.02309 MHz/ μs . Markers are made with repetitive peaks.

FSR is larger than that of the laser, which enables full range measurement of IAG longitudinal mode range. However the proper curved high reflectors are not immediately available. Besides, it requires extensive additional work to reconfigure current FPI setup while other experiments in the research group needs this setup as well. It is therefore beyond the scope of this dissertation to finish the improved version of the FPI covering 100% of the FSR of IAG planar waveguide lasers. More information about the FPI can be founded in the Appendix.

2.4.4 Polarization

Polarization is another important characterization of a laser. Conventionally, the

output beam from the laser resonator becomes anisotropic due to intracavity polarizing optics or the anisotropic gain media. It is found that the only polarization related mechanism inside the IAG planar waveguide laser is the polarization depended waveguide distributed loss. This anisotropic loss can be explained qualitatively by considering the Fresnel coefficients of the TE and TM polarization. TE polarization refers to the polarization along the x -axis while TM polarization refers to the polarization along the y -axis. The ray inside the IAG waveguide core tends to leak out to the cladding due to the reverse refractive index step. It is equivalent to consider a ray incident on a material interface from the optically rarer media to the optically denser media. The refracted beam represents the leak energy. The Fresnel coefficients are polarization dependent [68]. Consequently, the energy of the refracted ray depends on the polarization as well. For index-guiding waveguide, the total internal reflection eliminates the refracted beam leaving only evanescent field penetrating through the core-cladding interface. In this way, the polarization dependent loss inside index guiding waveguide is much smaller than inside IAG waveguide.

To describe the polarization behavior mathematically, polarization extinction ratio (PER) is used. PER denotes the purity of the output polarization, which is related with the intensity ratio between TE and TM polarization as given in Eq. (2.1).

$$PER = -10 \ln \left(\frac{I_{TE}}{I_{TM}} \right). \quad (2.1)$$

Experimentally, PER is calculated by measuring the intensity of TE and TM polarization respectively. To achieve this, a polarizer is needed. The experiment setup is shown in Fig. 2-16. The Glan-Thompson polarizer is used as PBS due to its large extinction ratio ($10^5:1$). The transmitted light has the same polarization with respect to the crystal axis. The PBS is

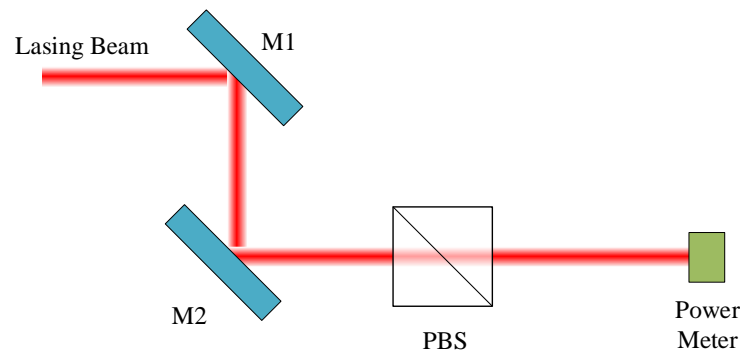


Figure 2-16. Schematic of experiment setup for the PER measurement.

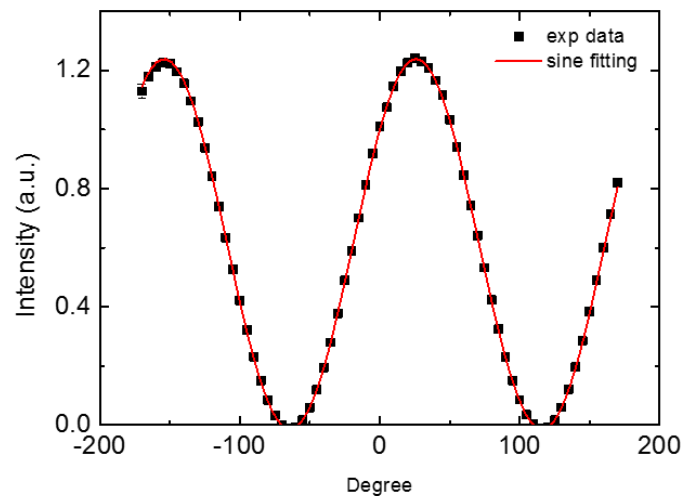


Figure 2-17. The transmitted intensity for a linear polarized laser beam at different rotation angle of PBS. The red line represents the sine fitting. The light source used in the experiment is the reconfigured pump laser in Spectral-Physics Millennia V.

rotated by a computer controlled rotation stage. A photodiode is placed behind the PBS to measure the transmitted intensity. To avoid background light, a long-pass filter (LPF) whose cut-off wavelength is $1\ \mu\text{m}$ is placed before the photodiode. The intensity for TE and TM polarizations is measured alternatively when PBS is rotated in one revolution. For instance, transmitted intensity for a linear polarized laser beam is given in Fig. 2-17.

The peaks in Fig. 2-17 corresponds to the TE polarization while the valleys corresponds to the TM polarization when considering the waveguide geometry. In this case, the PER is measured to be 27 dB suggesting a polarized light. The PER at different lasing power for $220\ \mu\text{m}$ chip is shown in Fig. 2-18. Throughout the experiments, the lasing mode is monitored using near-field imaging. The intensity profiles along the x -axis and y -axis is round and symmetry which suggests fundamental mode operation only. The pump power is set and then the lasing power is measured after 2 minutes which is believed to be the time for thermal equilibration. A virtual instrument interface is used to control the rotation of the PBS while the electric signal from the photodiode is then acquired using a NI DAQ block. The data is firstly fitted with cosine square shape, similar as shown in Fig. 2-17. The peak and valley values are then determined from the fitting and used to calculate the PER according to Eq. (2.1). It is worth noting that there are large deviation for the measurement taken with lasing power over 1 W.

The PER measurement result shows that TE polarization dominates while the purity of the output polarization reduces as the lasing power increases. It is understood since the polarization associated loss coefficients in IAG planar waveguide are calculated to be $8.1247 \times 10^{-4} \text{ cm}^{-1}$ for TE polarization and $9.4688 \times 10^{-4} \text{ cm}^{-1}$ for TM polarization respectively [69]. The increasing pump power facilitates the growth of the intensity of both TE and TM polarization. Due to larger loss coefficient for TM polarization, its intensity is expected to be smaller compared with the TE counterpart at the same incident pump power. However at large pump power, this intensity difference becomes insignificant resulting in the reduced PER. Around the maximal pump power, though, the dominated polarization changes from TE to TM which is reflected by the negative PER shown in Fig. 2-18. This is believed due to the thermal induced birefringence since the residual heat around the

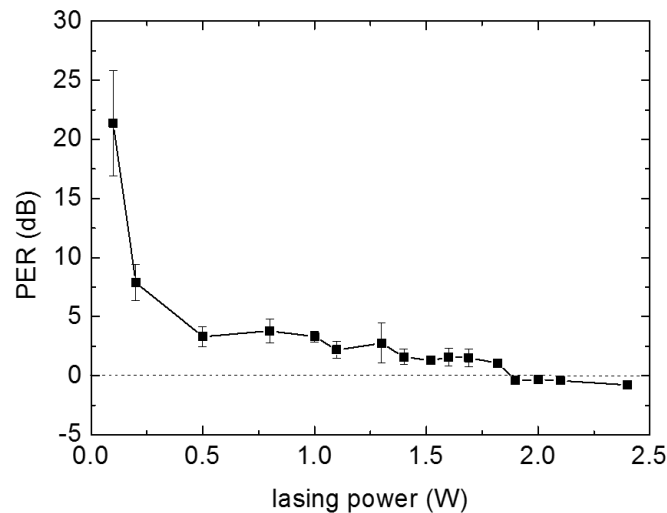


Figure 2-18. PER at different lasing power for 220 μm chip. The dash-line corresponds to the same lasing intensity for TE and TM polarization. The dash line represents PER equals zero, which indicated the same polarization amount.

maximal lasing power is at its maximal. Even a small loss coefficient difference can be magnified by the resonance inside the gain media.

2.4.5 Beam quality factor

The beam quality factor (M^2) is a parameter that widely used to represent the laser beam quality. The definition of M^2 is shown [67]:

$$M^2 = \frac{\pi}{2\lambda} \theta W_0, \quad (2.2)$$

where λ is the wavelength of the lasing signal; W_0 is the minimum beam radius (beam intensity drops to $1/e^2$); θ is the divergent angle for the Gaussian beam. $M^2 = 1$ denotes the diffraction-limited Gaussian beam. Experimentally, the measured M^2 is always larger than 1 since it is extremely difficult to get the perfect diffraction-limited Gaussian beam. M^2 can be calculated by measuring W_0 along the beam propagation direction. In IAG lasing experiment, this is achieved by translating the beam profiler (WinCamD) along a translation rail as shown in Fig. 2-19. Two high reflectors M1 and M2 are used to align the incident laser beam such that the optical axis is parallel with the moving axis of the trail. A lens (50 mm focal length) is used to transform output laser beam for the measurement. The beam profiler takes intensity profile along the transverse plane at a list of longitudinal direction. The profiles are then fitted with Gaussian shape and W_0 are extracted out. The parabolic fitting of W_0 and its location yields θ , with which the M^2 are calculated according to Eq. (2.2).

The typical measurement results are shown in Fig. 2-20 for lasing threshold and maximal output power. The M^2 along both bounded and unbounded direction at different

lasing power is given in Fig. 2-21.

For both bounded and unbounded directions, measured M^2 increase with lasing

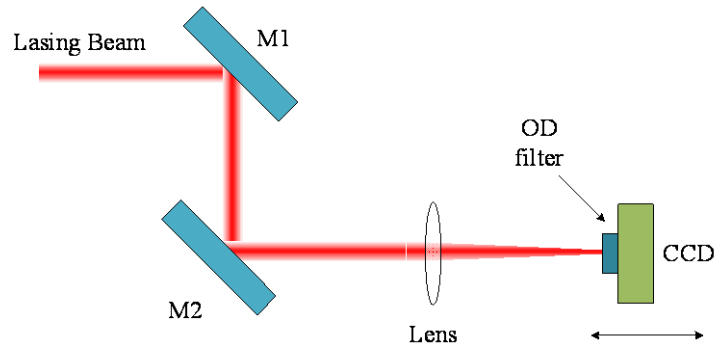


Figure 2-19. Schematic of experiment setup for M^2 measurement. To avoid the damage of the CCD pixel, an OD filter is added in front of the CCD.

power while M^2 result are close to 1 around lasing threshold. Along the bounded direction, M^2 is smaller than 2.5 while it shows a platform shape from 1 W to 2.5 W lasing power. Along the unbounded direction, measured M^2 increases with lasing power and its maximal

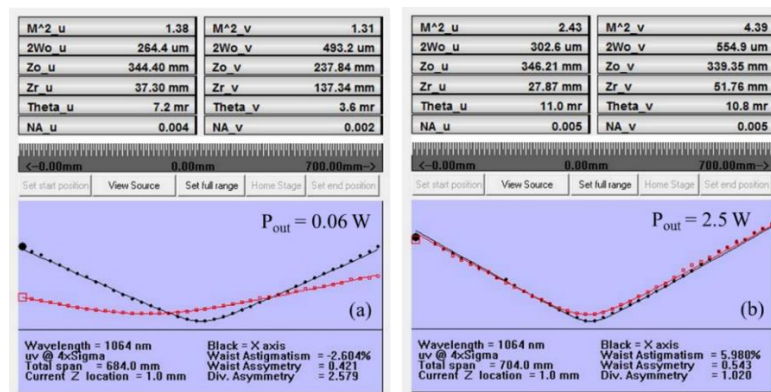


Figure 2-20. M^2 measurement results for (a) 0.06W lasing power and (b) 2.5W lasing power respectively.

value is 4.5. Throughout the measurement, the near-field mode is monitored and it is determined that only fundamental mode presents in the output. It has been reported by other researchers that the field in the cladding greatly affects the M^2 for IAG structure [70, 71]. It is believed due to the same reason that the M^2 along the bounded direction is larger than the results of conventional fundamental Gaussian mode along the bounded direction.

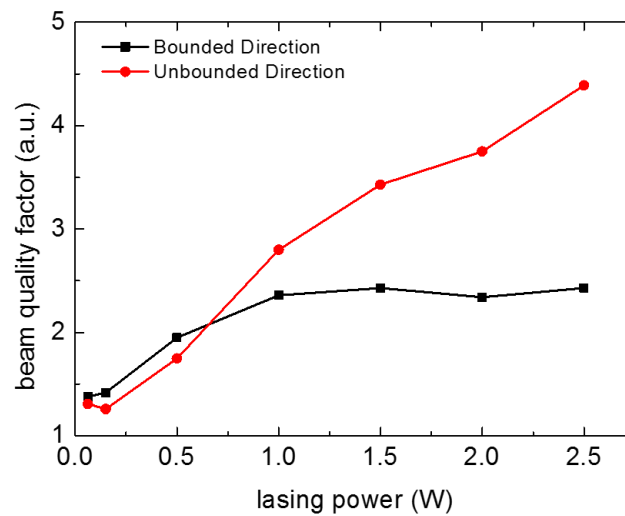


Figure 2-21 M^2 at different lasing power.

In addition, the fundamental mode of the IAG planar waveguide has a cosine shape whose diffraction pattern is different than its Gaussian counterpart. All these facts contribute to the obvious deviation of the M^2 data when the lasing mode is suggested to be fundamental mode by near-field imaging along the bounded direction. Consequently, it is determined in this dissertation that M^2 is not a valid parameter to determine the single mode operation.

2.5 Summary

In summary, the experiment setup and detail lasing output characterization are discussed in this chapter. The same experiment setup is used throughout all the chapters in this dissertation. The possible variation will be the change of IAG chip. The alignment process to achieve lasing, together with is mentioned in detail. Basic laser output such as transverse and longitudinal mode, polarization and beam quality factor are discussed. Based on the data, the 220 μm IAG planar waveguide laser shows great potential for high power, large mode area operation with only fundamental transverse mode operation. Besides, the beam quality factor behaves differently than traditional free-space lasers whose M^2 should be around 1 with fundamental Gaussian mode.

CHAPTER 3 MODE GUIDANCE INSIDE FACE PUMPED INDEX-ANTIGUIDED PLANAR WAVEGUIDE LASER

3.1 Introduction

Optical waveguide is amount the structures that light can be trapped inside. The most commonly found optical waveguide is the optical fiber where optical denser core surrounded by the optical rarer cladding. The total internal reflection provides physical background for trapping light inside the core region. Practically, signal rejuvenation is necessary only when significantly long-distance propagation is required which is often the case for modern telecommunication system.

Besides the total internal refraction, there are other mechanisms that can guide the light. For example, the material interface can be replaced by arrays of air holes while confined propagation modes can be found [72]. The geometrical parameters of the array can be designed to support lossless propagation of a spectral band along the axis of core [73]. This kind of waveguide is referred as photonics crystal waveguide [74]. Another design is to use only one layer of air-holes surrounding the core, which is referred as leaky channel waveguide [75]. The confined propagation of electromagnetic wave is found inside the core. However, due to the finite layers of air holes, energy inside the core tends to leak through the gaps between of the holes to the cladding. Thus, there is a propagation loss which is found to be associated with each order of waveguide mode [22]. In 2003, Siegman proposed a radical design of waveguide which has negative refractive index step and doped core. It has been shown theoretically that lossless propagation mode can be found by

providing proper power gain to overcome the propagation loss [52]. This waveguide structure is hereby referred as gain-guiding, index-antiguided (GG-IAG) waveguide [55]. Experiments based on Nd^{3+} doped phosphate fibers verified Siegmen's theory [53, 64]. Results showed pure fundamental mode operation was achieved with up to 400 μm core diameter GG-IAG fibers while commercial available LMA fiber only has a core diameter of 35 μm . Since propagation of fundamental mode requires optical gain, the doped core has to be pumped for optical amplification. Thus, there is residual heat generated inside the core. In addition, the large core size of GG-IAG fiber makes heat conduction difficult. Researches also show that the output IAG laser suffers from thermal induced distortion even with length shorter than 20 cm [56, 76-78]. GG-IAG fibers have to work in gain switching mode to avoid thermal failure [53, 56, 64]. For IAG planar waveguides, the passive cooling is not sufficient to remove all the residual heat, leading to the obvious shrinkage of the near-field mode [78]. All these facts require analysis of thermal effects inside IAG structure when power scaling is considered. Hence, a model on modal guidance inside planar waveguide lasers with face pumped in developed in this chapter.

Chapter 3 is organized as follows: in section 3.2, the general theory of the index antiguiding is analyzed. In section 3.3, the guiding mechanism, including thermal refractive focusing and quadratic gain focusing, inside the face pumped IAG planar waveguide are discussed theoretically. In section 3.4, the experiment and simulation results are discussed in detail. Final remarks are made in section 3.5.

3.2 Index antiguiding

Typical IAG planar waveguide with step-index profile is illustrated in Fig. 3-1. The refractive index of the waveguide cladding and core are n_1 and $n_1 + \Delta n$ respectively. The

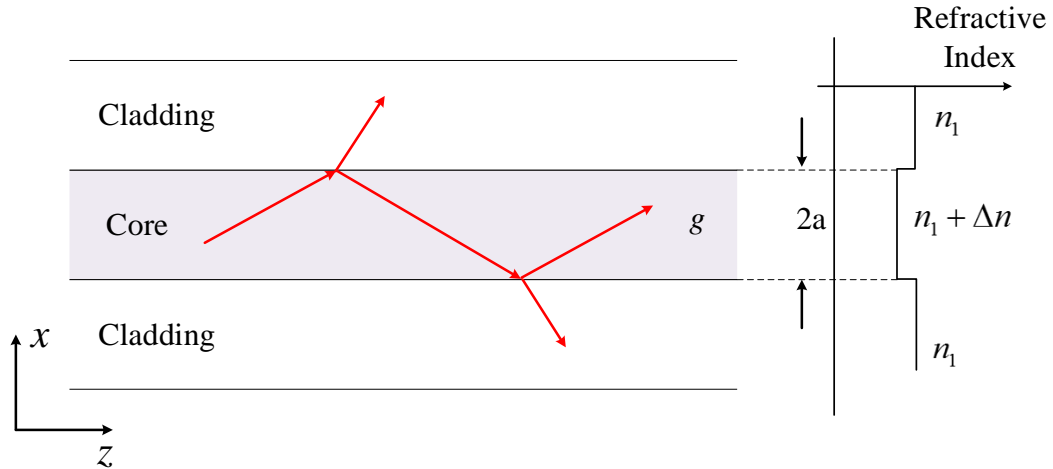


Figure 3-1. Schematic illustration of the waveguide structure of IAG planar waveguide. g is the amplitude gain coefficient in the core region. The core thickness is $2a$. The red line indicates the rays inside the waveguide.

refractive index difference Δn is negative for IAG waveguide. The waveguide core is doped such that it can provide amplitude gain when optically pumped. The waveguide modes propagate along the z -axis while the intensity pattern associated with modal order is observed in x - y plane.

3.2.1 Complex $\tilde{\nu}$ number

A uniform plane wave propagating in IAG waveguide core with the initial amplitude E_0 is expressed as

$$E(x) = E_0 \exp \left[-j \frac{2\pi(n_1 + \Delta n)z}{\lambda} + gz \right]. \quad (3.1)$$

The unique feature of IAG waveguide is represented by the presence of amplitude gain coefficient g inside the exponential argument [52]. For index-guiding step waveguide, the waveguide argument is reflected by the real propagation constant $\beta = 2\pi(n_1 + \Delta n) / \lambda$. The involvement of g transfers the propagation constant from real to complex. The complex

propagation constant $\tilde{\beta}$ is then given by $\tilde{\beta} = 2\pi(n_1 + \Delta\tilde{n})/\lambda$ where complex refractive index step $\Delta\tilde{n}$ is represented by $\Delta\tilde{n} = \Delta n + j(\lambda/2\pi)g$. It is convenient to introduce the dimensionless complex \tilde{v} number the square of which is given by:

$$\tilde{v}^2 = \left(\frac{2\pi a}{\lambda}\right)^2 \left[(n_1 + \Delta\tilde{n})^2 - n_1^2 \right] \approx \left(\frac{2\pi a}{\lambda}\right)^2 2n_1 \left(\Delta n + j\frac{\lambda}{2\pi}g \right) \quad (3.2)$$

The approximation for the second step in Eq. (3.2) is valid when the refractive index difference is relatively small compared with the absolute value of n_1 . More insights can be gained by expressing \tilde{v}^2 in terms of its real and imaginary part as $\tilde{v}^2 = \Delta N + jG$, where

$$\Delta N = \left(\frac{2\pi a}{\lambda}\right)^2 2n_1 \Delta n, \quad (3.3)$$

$$G = \left(\frac{2\pi a}{\lambda}\right)^2 \left(\frac{n_1 \lambda}{2\pi}\right) g. \quad (3.4)$$

As shown in Eq. (3.3) and Eq. (3.4), the refractive index step for IAG waveguide is associated with the real part of \tilde{v}^2 while the amplitude gain coefficient is represented by the imaginary part \tilde{v}^2 . According to the sign of ΔN and G , therefore the sign of Δn and g , the waveguide structure can be divided into 4 categories:

1. Index guiding (IG): $\Delta n > 0$ It is found in conventional optical waveguides for instance step-index optical fiber [66]. The guiding mechanism for this case is total internal reflection.
2. Gain guiding (GG): $g > 0$ It is found in semiconductor waveguide lasers [79] and gas lasers [80]. The optical mode with confined energy inside the core can be found which is supported by the

profile of the optical gain.

3. Index antiguiding (IAG): $\Delta n < 0$
This kind of waveguide is considered to be leaky where the energy in the core region tends to leak to the cladding [52]. It is widely found in semiconductor lasers due to the limited material choices [35].
4. Loss guiding (LG): $g < 0$
It will be shown in the following section that even in this structure, a stable mode or at least mode like solution can be found. In addition, it has been proved that the modes in LG case tend to couple the energy from the lower order modes to higher order modes when perturbation is introduced to the waveguide [67].

It is worth noting that $\tilde{\beta}$ is modal dependent and it is related with complex parameters \tilde{w} and \tilde{u} through:

$$(\tilde{\beta}a)^2 = \left(\frac{2\pi a}{\lambda}\right)^2 (n_1 + \Delta\tilde{n})^2 - \tilde{u}^2 = \left(\frac{2\pi a}{\lambda}\right)^2 (n_1 + \Delta\tilde{n})^2 + \tilde{w}^2 . \quad (3.5)$$

Considering Eq. (3.2), \tilde{u} and \tilde{w} are related with \tilde{v} as

$$\tilde{u}^2 + \tilde{w}^2 = \tilde{v}^2 . \quad (3.6)$$

The dispersion equations for IAG planar waveguide are given based on \tilde{w} and \tilde{u} as

$$\tilde{w} = \tilde{u} \tan \tilde{u} \quad \text{for symmetric modes (odd modes)} , \quad (3.7)$$

$$\tilde{w} = -\frac{\tilde{u}}{\tan \tilde{u}} \quad \text{for antisymmetric modes (even modes)} . \quad (3.8)$$

Eq. (3.1) to Eq. (3.8) forms the mathematical base describing modes inside IAG planar

waveguides. Similar parameters in conventional step index waveguide are used [81]. Due to g and negative Δn , the conventional parameters associated with optical waveguide is transferred from real to complex. Solutions to the dispersion equations yield the mode shape for desired modal order in IAG planar waveguide.

3.2.2 Fundamental mode

To gain insights on modal shape of IAG planar waveguide, the fundamental mode is analyzed in this section. The electric field along the transverse direction (x -axis) for fundamental mode inside the IAG waveguide is given by:

$$E(x) = \begin{cases} \cos\left(\frac{\tilde{u}}{a}x\right) & |x| \leq a \\ \cos(\tilde{u}) \exp\left[-\frac{\tilde{w}}{a}(|x|-a)\right] & |x| \geq a \end{cases} \quad (3.9)$$

To be confined, the mode has to carry finite energy and can be normalized inside the cladding. This requires the real part of \tilde{w} be a positive number. Thus, the possible solutions of \tilde{w} locate in the first and fourth quadrant of complex \tilde{w} plane as shown in Fig. 3-2. Each point in Fig. 3-2 represents one possible solution of \tilde{w} . The line by the black scatters forms the line of pure GG (in first quadrant) and pure LG (in fourth quadrant), Δn of which are zero. According to Eq. (3.5), $\tilde{\beta}$ is approximated as

$$\tilde{\beta} \approx kn_1 + \frac{\tilde{w}^2}{2kn_1a^2} = kn_1 + \left(\frac{1}{2kn_1a^2}\right)(w_r^2 - w_i^2 + 2jw_rw_i), \quad (3.10)$$

where $k = 2\pi / \lambda$ and $\tilde{w} = w_r + jw_i$. The GG (LG) occurs when the imaginary part of Eq. (3.10) is positive (negative), which locates in first quadrant (fourth quadrant). The real part of Eq. (3.10) is zero for pure GG or LG, namely $w_r^2 - w_i^2 = -2k^2n_1^2a^2$. As w_r and w_i increase, this condition is approximated to be $w_r^2 - w_i^2 \approx 0$, which yields the 45 degree

black scatter lines at the top-right or bottom right corners. The region where $\text{Re}[\tilde{\beta}]$ is positive locates under below the black line in the first quadrant and above the black line in the fourth quadrant. This region represents the IG while the region formed by vertical axis and the black dots represents the IAG region.

The allowed region where $w_r > 0$ is transformed into complex \tilde{u} plane as plotted in Fig. 3-3. The allowed \tilde{u} locates between two blue thick lines. The two black thinner

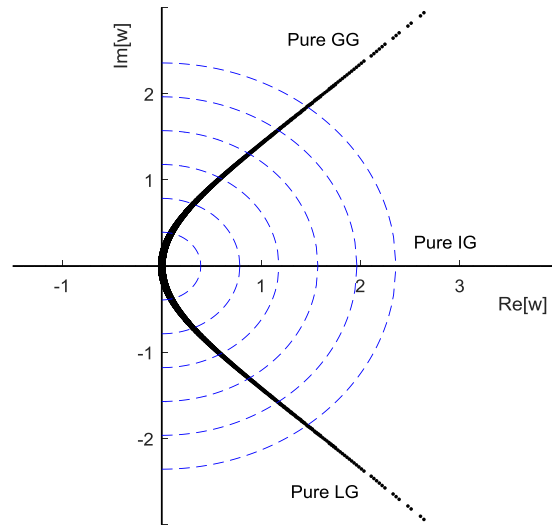


Figure 3-2. Values for possible \tilde{w} parameters for lowest order mode. The line formed by the black scatter dots represents the pure GG (in first quadrant) and pure loss guiding (in fourth quadrant). The pure IG occurs with the points along the horizontal axis. The blue dash line corresponds to the $|\tilde{w}| = n\pi/8$, where n is integer ranging from 1 to 6.

lines represent the pure GG and pure LG as marked. The thinnest lines from the left to the right correspond to the same condition as denoted by the dash lines in Fig. 3-2. To be specific, the allowed real part of complex \tilde{u} parameter u_r at a given ΔN is plotted in Fig.

3-4. The horizontal axis denotes ΔN while the vertical axis denotes $2u_r / \pi$. It is worth noting that as $|\Delta N|$ decreases, the allowed u_r occurs only in a narrow band in the vicinity

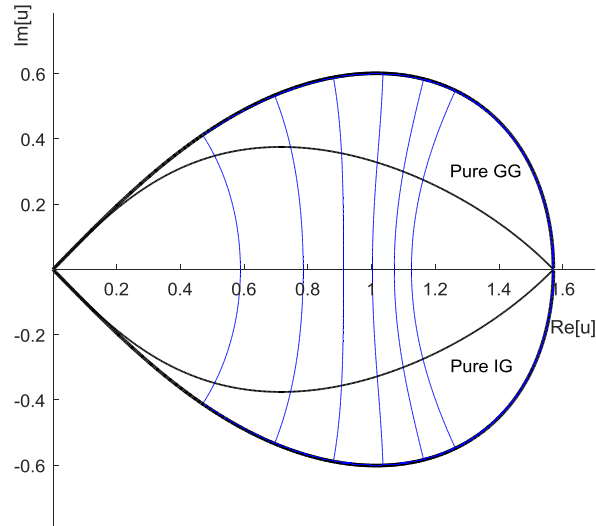


Figure 3-3. The allowed value of \tilde{u} . The outer blue thick lines represents the boundaries of the possible \tilde{u} . The upper thinner line in the first quadrant represents the pure GG in Fig. 3-2. The lower thinner line in fourth quadrant represents the pure LG in Fig. 3-2. The blue line from the left to right represents the $|\tilde{w}| = n\pi/8$, where n is integer ranging from 1 to 6.

of $\pi/2$, the width of which reduces. Meanwhile, the allowed u_r locates in the vicinity of zero as shown in Fig 3-3. Thus, the mode field in Eq. (3.9) can be approximated to zero at the material interface when $|\Delta N|$ is sufficient large. This is referred as zero-field approximation, or ZFA. Though the analysis above is based on the fundamental mode, it can be extended to higher order modes where \tilde{u} approaches to $m\pi/2$ where m is the modal order. The ZFA implies that as the absolute refractive index difference $|\Delta n|$, therefore $|\Delta N|$ increases, either towards positive direction (index guiding, $\Delta N > 0$) or

towards negative direction (index antiguiding, $\Delta N < 0$), the absolute mode field value at the core-cladding interface will decrease. This nature helps to approximate the mode field inside the IAG waveguide core to a simple analytical form, which is crucial for power simulation of a given IAG structure.

3.2.3 High-order modes

So far the analysis is focused on the fundamental mode. When considering higher order modes, it is convenient to plot the possible solutions of each modes in the complex \tilde{v}^2 plane as shown in Fig. 3-5. In this plane, each point represents a specific waveguide design characterized by G and ΔN . The lines labeled with modal order m corresponds to the boundaries of all the possible solutions for the each order mode. The region formed by the dark blue curves including the negative direction of horizontal axis is the region that no propagation mode can be found. The waveguide designs that only support the lowest

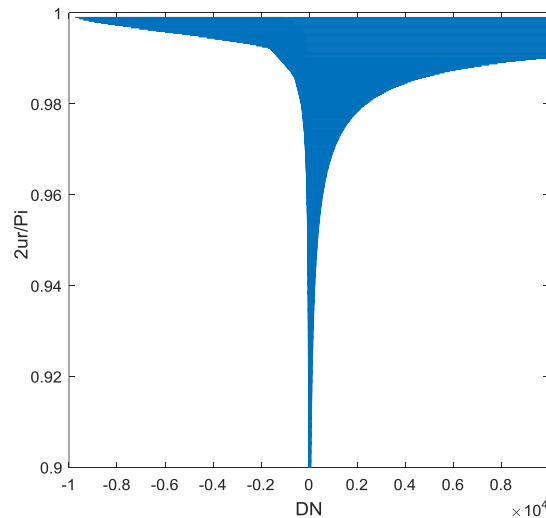


Figure 3-4. The allowed u_r of a given ΔN for the lowest order mode. The blue region denotes the possible region of u_r . The horizontal axis denotes ΔN while the vertical axis denotes the ratio between $2u_r / \pi$.

order mode locates in the ribbon region formed by $m = 1$ and $m = 2$ curves. The waveguide designs that can support both the lowest order mode and first higher order mode locate in the ribbon-shape region formed by the curves labeled $m = 2$ and $m = 3$. Same scenarios apply to the other curves though not given in Fig. 3-5.

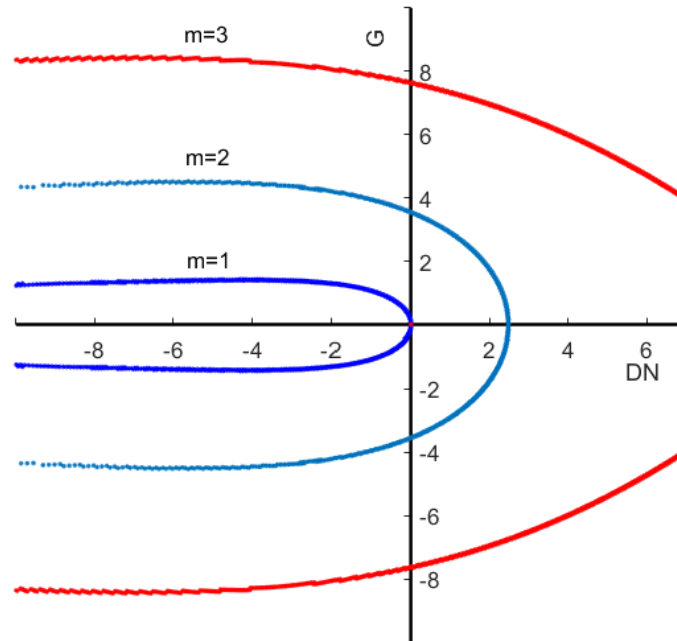


Figure 3-5. Complex $\tilde{\nu}^2$ plane and the boundaries of the modal order. The horizontal axis corresponding to ΔN (DN in the plot) while the vertical axis corresponding to G .

Special interests are devoted to the case of IG and GG due to their physical significance. The points located along the positive direction of horizontal axis correspond to the pure IG waveguides, for instance, conventional step index planar waveguide. $\tilde{\nu}$ reduces to the conventional normalized frequency ν . It is well known that such waveguide, the cut-off ν for first higher order mode is around 1.5. And there is no cut-off ν for the lowest mode. This is reflected by the line between the origin and the intersection of $m = 2$

curve with horizontal axis in Fig. 3-5.

The waveguide configuration with pure GG locates along the positive vertical axis. It is known that GG can support at least one mode [82]. This is reflected by the line between the origin and the intersection of $m = 2$ curve with vertical axis. For IAG waveguides ($\Delta N < 0$ and $G > 0$), there does not exist propagation mode in the region which is surrounded by $m = 1$ curve and includes origin. Appropriate gain is needed to facilitate mode propagation even for the lowest order. The minimum gain required for propagation is treated as modal propagation loss in the following chapters. This loss is the unique feature of the IAG waveguide. As shown by Yeh [69], the modal intensity loss coefficient for s -th order TE and TM modes in one dimensional (1-D) leaky planar waveguide are mathematically expressed as

$$\alpha_s^{TE} = \frac{s^2 \lambda^2}{2a^3 \sqrt{(n_1 + \Delta n)^2 - n_1^2}}, \quad (3.11)$$

$$\alpha_s^{TM} = \frac{s^2 \lambda^2 (n_1 + \Delta n)^2}{2a^3 \sqrt{(n_1 + \Delta n)^2 - n_1^2}}. \quad (3.12)$$

The loss inside IAG waveguide is unique and controversial for several reasons: On one hand, the energy efficiency of IAG waveguide is effected by α_s . Efforts should be devoted to reduce this loss by either changing the waveguide dimension or increasing the refractive index difference. For example, increasing the waveguide thickness will sufficiently reduce α_s . In this way, large-mode-area (LMA) IAG waveguides can be made with reduced propagation loss waveguide design. Proper gain helps to selectively support the lossless propagation of the lowest order mode while higher-order modes are below propagation threshold. Eventually, a LMA waveguide with fundamental mode operation is

achieved with IAG structure. However, the suitable waveguide is difficult to manufacture. For example, materials with proper refractive index difference may have large lattice constant difference. Consequently, it is difficult to perfectly join the core and cladding, adding additional waveguide loss.

On the other hand, it is beneficial for higher-order modes to propagate in IAG waveguide when α_s is small. Usually, a large loss contrast between two adjacent transverse modes are essential for modal discrimination [36]. In IAG planar waveguide, adjacent TE mode loss coefficient ratio $\alpha_2^{TE} / \alpha_1^{TE} = 4$. The reduction of α_1^{TE} is effectively reducing α_2^{TE} risking to allow higher-order modes propagating lossless. In IAG laser device in particular, it will be shown in the following chapters that the gain saturation and the coupling loss due to the gap between IAG crystal and cavity mirrors help the mode discrimination process.

3.3 Hyper guiding inside index-antiguidded planar waveguides

Hyper guiding waveguide refers to the waveguide in which the guiding mechanism are different along two orthogonal direction, namely the bounded and unbounded directions [37]. For IAG planar waveguide in particular, the mode is affected by index antiguiding along the bounded direction while the mode along the unbounded direction is controlled by the pump profile. As discussed at the beginning of this chapter, the thermal refractive focusing effect along both directions need to be considered. In this section, the effect of gain profile and thermal profile on the fundamental mode of 220 μm IAG planar waveguide laser will be discussed.

3.3.1 Gain profile

To provide optical gain, the doped waveguide core need to be optically excited. As

mentioned in chapter 2, the pump light is focused to a line for face-pumping. Since the absorption length for Nd:YAG is much longer than the core thickness, the focused pump radiance along the bounded direction is assumed to be uniform. Meanwhile, the pump profile along the unbounded direction is measured to be quadratic shape with peak at its center (discussed in chapter 4). Normalized pump density $\rho(x, y, z)$ is used in this chapter, which is related with absorbed pump power P_{ab} as:

$$\iiint_V \rho(x, y, z) dx dy dz = P_{ab} \quad (3.13)$$

As far as the transverse plane is considered, the pump density along the z -axis is assumed to be uniform. $\rho(x, y, z)$ is expressed explicitly:

$$\rho(x, y, z) = \rho(y) = \rho_0 \left(1 - \frac{y^2}{r_p^2} \right), \quad (3.14)$$

where r_p is the radius of the pump profile at which the intensity drops to zero; ρ_0 is peak density which is calculated to be

$$\rho_0 = \frac{3P_{ab}}{2(l_z \cdot 2r_p \cdot 2a)}, \quad (3.15)$$

where l_z is the length of the pump profile along the z -axis, which is the length of the chip; The product $(l_z \cdot 2r_p \cdot 2a)$ represents the gain volume V . The absorbed pump energy excites the dopant ions from its ground level to laser upper level. It is worth noting that there may be other energy level involved in this process. However, the detail lasing transition of Nd:YAG at 1.06 μm is well documented and it is not the interest of this dissertation to explain it in detail. References such as [67] and [65] provide necessary explanation if additional information is needed. The optical amplification is achieved when the condition

of population inversion is met. The intensity small signal gain coefficient g_0 is expressed as [65]:

$$g_0 = \sigma_{21} N_0 W_p \tau_f, \quad (3.16)$$

where σ_{21} is the emission cross section (cm^2) of laser upper and lower level; N_0 is population of the ground level; W_p is the pump rate and τ_f is the fluorescence life time.

The product $W_p N_0$ denotes the number of atoms that transferred from the ground level to laser upper level due to the pump energy. It is this portion of atoms that contributes to the population inversion, therefore the gain of the laser inside the cavity. $W_p N_0$ can be expressed in terms of absorbed pump power P_{ab} :

$$W_p n_0 = \eta_Q \eta_S \eta_B \frac{P_{ab}}{h\nu_L V}, \quad (3.17)$$

where η_Q is the quantum efficiency, which is assumed to be 0.95; η_S is Stokes factor which represents the energy fraction of the lasing photon over pump photon. The rest energy of the pump photon is presented as heat and dissipates through the cladding of the waveguide to heat sink. Since Nd:YAG core is pumped with 808 nm diode laser, $\eta_S = 0.76$; η_B is the mode overlap factor, which express how well the overlap between lasing mode and pump region which is estimated to be 0.24. Substitute Eq. (3.17) into Eq. (3.16) and g_0 is expressed as:

$$g_0 = \eta_Q \eta_S \eta_B \frac{\sigma_{21} \tau_f}{h\nu_L} \frac{P_{ab}}{V}, \quad (3.18)$$

The expression $\sigma_{21} \tau_f / h\nu_L$ is the parameter that only concerns about the laser material and energy level parameters. For a four-level system, it can be expressed in terms

of saturation intensity:

$$I_s = \frac{h\nu_L}{\sigma_{12}\tau_f} . \quad (3.19)$$

It helps further simplify the small-signal gain expression:

$$g_0 = \eta_Q \eta_S \eta_B \frac{P_{ab}}{I_s V} . \quad (3.20)$$

To involve the pump density, one can replace P_{ab}/V with $\rho(x, y, z)$. The small-signal gain is then expressed as

$$g_0(x, y, z) = \frac{\eta_Q \eta_S \eta_B \rho_0}{I_s} \left(1 - \frac{y^2}{r_p^2} \right) \quad (3.21)$$

It is shown in Eq. (3.21) that the gain along the unbounded direction shares the same quadratic shape as the incident pump.

3.3.2 Thermal profile

The heat generation inside the CW solid-state lasers is inevitable for the following reasons: Firstly, there are energy difference between pump and lasing photon. Even if the quantum efficiency is 1 indicating that 1 pump photon generates 1 lasing photon, this energy deviation between pump and lasing photon leads to the quantum defect heating. This sets the power efficiency limit to the Stokes factor in typical 4 level system. Secondly, the quantum efficiency for a real laser is usually smaller than one without multi-phonon transition process, for instance cross relaxation where one pump photon can induce more than one lasing photon. The energy of the non-radiation transition from the lasing upper level to the lasing lower level often takes form of heat. Thirdly, the unabsorbed pump radiation interacts with the defects inside gain media, the interaction of which often results in the heat generation.

The presence of heat inside the pumped gain media introduces thermal stress and thermal optical distortion [65]. Thermal stress sets the physical damage limit for a particular gain medium due to surface stress. Failure can be found when the thermal stress is larger than the surface stress limit for a single crystal. It is worth noting that in a bonded structure, such as the IAG planar waveguide, mechanical stress may lead to the failure of the bonding. Besides thermal stress, optical distortion is another thermal-optical effect inside CW operation solid-state lasers. There are two major optical distortions, namely thermal lensing and thermal induced stress birefringence. Thermal lensing is due to the thermal induced refractive index variation which distorts the wavefront. Assume plane wave propagating in such media. The wavefront picks up different optical path length at its center than its edge. In this way, the media behaves similar as a refractive focusing or defocusing lens. Besides, the material response to thermal induced mechanical stress may introduce optical birefringence. For IAG planar waveguide in particular, stationary heat transfer analysis based on finite elements analysis is used to calculate the temperature distribution inside the IAG waveguide chip.

The parameters used in the model are listed in table 3-1. The quantum defect heating due to pumping process is assumed to be the only heat source inside the waveguide core. Thus, the heat density share the same profile as pump density given by Eq. (3.21). It is estimated that 20% of the incident pump power is absorbed while 30% of the absorbed pump power is dissipated in terms of heat. To include all other possible non-radiation transition or absorption, the number 30% is larger than the theoretical calculation value which is 24%.

Table 3-1. Parameters used in heat transfer simulation

Parameter	Value
Nd:YAG Thermal Conductivity	14 W m ⁻¹ K ⁻¹
Nd:YAG Density	4550 kg m ⁻³
Nd:YAG Heat Capacity	590 J kg ⁻¹ K ⁻¹
TGG Thermal Conductivity	4.7 W m ⁻¹ K ⁻¹
TGG Density	7130 kg m ⁻³
TGG Heat Capacity	393 J kg ⁻¹ K ⁻¹
Cooling Temperature	15 degree C
Background Temperature	20 degree C

To illustrate the extreme circumstance, the instrument-limited maximal incident power is applied. The temperature profile with 25 W incident pump power is calculated as shown in Fig. 3-6. The two vertical lines in Fig. 3-6 represent the core-cladding boundaries. The heat sink locates at the left side, the temperature of which is actively controlled to 15 degree C. Other surfaces are subjected to convective boundaries with a constant ambient temperature which is 20 degree C. The calculated highest temperature is 18.3 degree C which locates at the center of the heating zone.

Due to the unsymmetrical thermal diffusion, the temperature profile is distorted towards the side where the heat sink locates. To illustrate it, the temperature profiles along the bounded and unbounded directions are extracted and plotted respectively in Fig. 3-7.

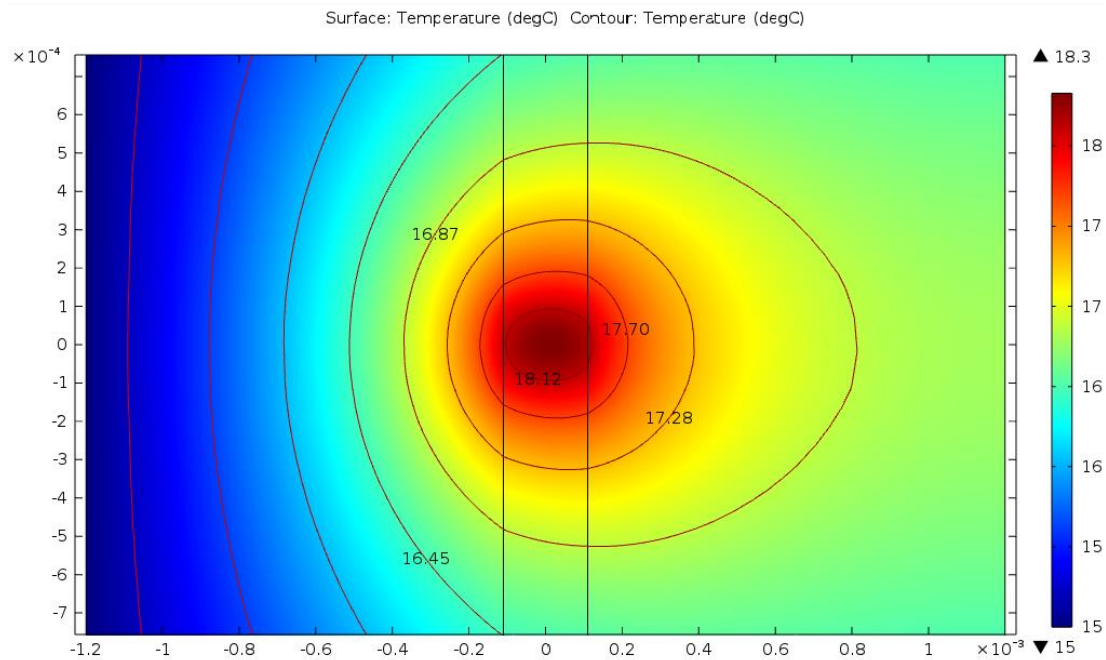


Figure 3-6. Temperature distribution in transverse plane.

Along the bounded direction, the peak of the temperature locates slightly towards the uncooled side leaving the two cladding area with different temperature. The temperature at the core-cladding boundaries has a maximal difference of 3.3 degree C. Due to the face pumping, it is extremely difficult to achieve actively temperature control on both side of the waveguide chip. However, the profile shows good fitting with parabolic shape inside the waveguide core region. For unbounded direction, the temperature distribution is symmetry partially due to the parabolic pump density and shows good agreement with

parabolic fitting while large deviation happens around the edge of pump density.

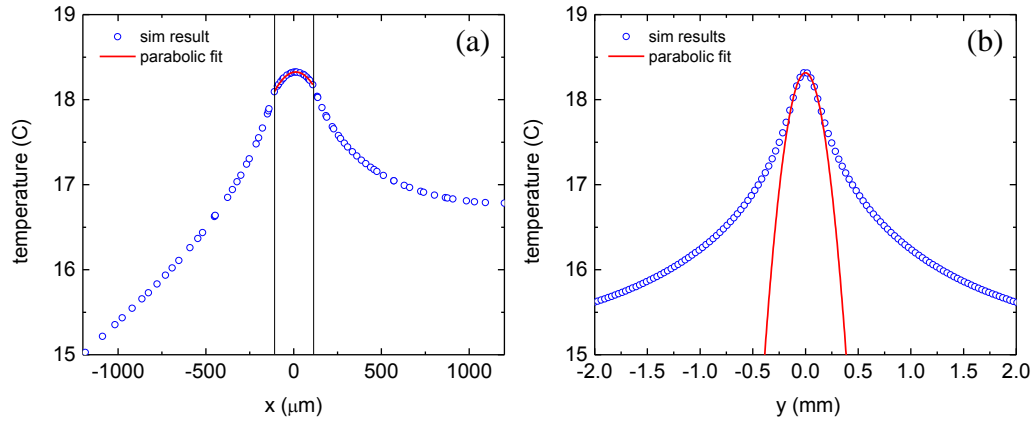


Figure 3-7. Temperature profiles along (a) the bounded and (b) the unbounded directions. The red line in each figure represents the parabolic fitting.

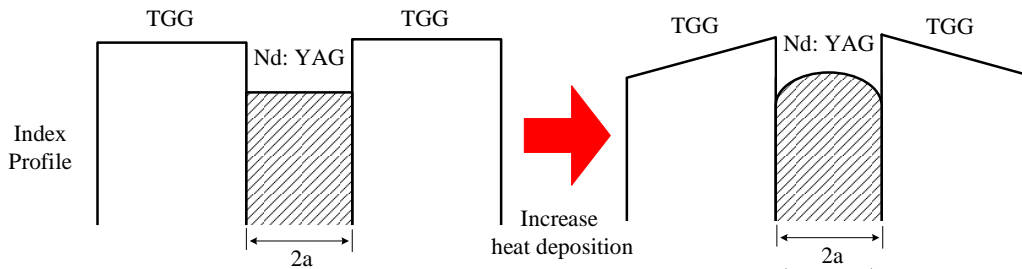


Figure 3-8. Index profile of IAG planar waveguide including thermal induced refractive index variation.

The temperature profiles prove that face-pumped IAG planar waveguide has a much smaller temperature deviation from its peak to the heat sink compared with reported end-pumped IAG fiber [57]. The low peak temperature makes CW operation possible with face pumping. However, even as small as it is, the thermal gradient inside the waveguide core introduces refractive index variation. To simplify the modeling process, the heat diffusion

is assumed only either along x -axis or along y -axis. Heat cross-diffusion is negligible. The change of refractive index inside the IAG planar waveguide is illustrated in Fig. 3-8.

The refractive index inside the core region is expressed as [18]:

$$n(x, y) = n_0 + \frac{(2a)^2 \rho(y) f}{8\kappa} \frac{dn}{dT} \left(1 - \frac{4x^2}{t^2} \right), \quad (3.22)$$

where dn/dT is the refractive index change due to temperature variation; κ is thermal conductivity; f is the thermal load, typically 0.34-0.4 for lasing Nd:YAG at 1.06 μm [83].

The product $2a \cdot \rho(y) \cdot f$ is the amount of absorbed pump energy that transferred into heat.

Substitute Eq. (3.14) into Eq. (3.22) and expand the result in terms of the order of x and y , one can get:

$$n(x, y) = n_0 + \frac{(2a)^2 f}{8\kappa} \frac{dn}{dT} \rho_0 \left(1 - \frac{4x^2}{t^2} - \frac{y^2}{r_p^2} + \frac{4x^2 y^2}{t^2 r_p^2} \right). \quad (3.23)$$

Eq. (3.23) indicates that the pump profile imposes a quadratic variation on the refractive index in given x - y plane through thermal refractive focusing ($dn/dT > 0$ for Nd:YAG). This is verified by the temperature profile given in Fig. 3-7. However, the quadratic index profile is valid around the center of the heating zone. Deviation of the temperature, therefore the induced refractive index, from the quadratic shape is found around the edge of the heating zone. Due to ZFA, the lasing mode is mainly confined inside the core region which renders the temperature around the heating boundaries insignificant in term of affecting the lasing mode.

3.3.3 Lens-like media

To analyze the mode inside the IAG waveguide core, scalar Helmholtz equation are used. Assume $E(x, y, z)$ represents transverse Cartesian component of the laser electric

field inside the waveguide core. The Helmholtz equation is expressed as

$$\nabla^2 E(x, y, z) + \tilde{k}^2 \cdot E^2(x, y, z) = 0. \quad (3.24)$$

To represent the quadratic gain and refractive index profile in the transverse plane, the profile of complex wavenumber \tilde{k} is approximated to be quadratic described as:

$$\tilde{k}(x, y) = k_0 - \frac{\delta k}{2}, \quad (3.25)$$

where $\delta k = k_{2x}x^2 + k_{2y}y^2$. The wavenumbers k_n ($n=0, 2x, 2y$) used in this section are expressed as $k_n = \beta_n + j\alpha_n$ where β_n and α_n are the corresponding real and imaginary part respectively. β represents the propagation characteristics of the mode field, which is closely related with the refractive index profile. Meanwhile, α represents the amplitude gain of the mode field. For k_0 in particular, the real part is given by $\beta_0 = 2\pi(n_1 + \Delta n) / \lambda$ while α_0 is negligible. Since δk is small compared with k_0 , it is reasonable to drop $(\delta k)^2$ term when taking the square of Eq. (3.25):

$$\tilde{k}^2(x, y) = k_0(k_0 - k_{2x}x^2 - k_{2y}y^2). \quad (3.26)$$

The quadratic complex wavenumber indicates that the phase for a uniform wavefront propagating inside the IAG waveguide core depends on the transverse location. This phenomenon shares the same principle of conventional optical lens. Thus, the media is referred as lens-like media. To analyze the contribution of thermal refractive focusing and gain profile on the lasing mode, real and imaginary part of $\tilde{k}(x, y)$ are separated. The real part of $\tilde{k}(x, y)$ is related with refractive index $n(x, y)$ and vacuum wavelength λ through:

$$\text{Re}[\tilde{k}(x, y)] = \frac{2\pi}{\lambda} n(x, y). \quad (3.27)$$

As discussed in section 3.3.1, the thermal refractive focusing is the mechanism by which the refractive index profile is affected. The real parts of k_{2x} and k_{2y} are then determined by substituting Eq. (3.23) into Eq. (3.27) and requiring the coefficients in front of each order of x and y terms be equal:

$$\text{Re}[k_{2y}] = \beta_{2y} = \frac{2\pi f}{\lambda} \frac{dn}{\kappa dT} \rho_0 \left(\frac{2a}{r_p} \right)^2, \quad (3.28)$$

$$\text{Re}[k_{2x}] = \beta_{2x} = \frac{2\pi f}{\lambda} \frac{dn}{\kappa dT} \rho_0. \quad (3.29)$$

Since β_{2x} and β_{2y} are related with the quadratic thermal profile along x and y axis respectively, they are referred as thermal refractive focusing parameters.

The imaginary part of k_{2y} is related with the gain profile given by Eq. (3.21). To emphasize the shape and its impact on lasing field, the electric-field gain parameter α_0 and quadratic gain focusing parameter α_{2y} , which is related with pump density through:

$$\frac{\eta_Q \eta_S \eta_B}{I_s} \rho(y) = 2\alpha(y) = 2\alpha_0 - 2\alpha_{2y} \cdot y^2. \quad (3.30)$$

By comparing the coefficients in front of the spatial coordinate in Eq. (3.30), α_{2y} is then extracted out as:

$$\alpha_{2y} = \frac{\eta_B \eta_Q \eta_S}{2I_s} \frac{\rho_0}{r_p^2}. \quad (3.31)$$

Since α_{2y} is related with the quadratic gain profile, it is therefore referred as quadratic gain focusing parameter.

As shown from the mathematical derivation above, especially the results represented by Eq. (3.28), Eq. (3.29) and (3.31), the pump profile influences the mode field

in both bounded and unbounded directions. Along the bounded direction, the mode field is affected by the index antiguiding and thermal refractive focusing. Meanwhile, along the unbounded direction, the mode is affected by the gain profile and thermal refractive focusing. Due to the difference in terms of the guidance mechanism in these two orthogonal directions, the face-pumped IAG planar waveguide is a hybrid guided waveguide. The implication of the hybrid guiding on the lasing mode is explained in the next section.

3.4 Fundamental mode inside hyper guided IAG planar waveguide laser

As discussed in section 3.3.3, the electric field propagation inside the IAG planar waveguide core is governed by Helmholtz equation as given by Eq. (3.24). Analytical solution to it can be obtained by using the separable of variables method. Assume $E(x, y, z)$ is expressed as:

$$E(x, y, z) = X(x)Y(y, z). \quad (3.32)$$

Substitute Eq. (3.32) into Eq. (3.24), one can two individual equations describing the mode field along x and y axis:

$$\frac{1}{X(x)} \frac{\partial^2 X(x)}{\partial x^2} + (a_x - k_0 k_{2x} x^2) = 0, \quad (3.33)$$

$$\frac{1}{Y(x)} \frac{\partial^2 Y}{\partial y^2} + \frac{1}{Y(x)} \frac{\partial^2 Y}{\partial z^2} + k_0 (k_0 - k_{2y} y^2) - a_x = 0, \quad (3.34)$$

where a_x is a constant and independent with either x or y . By solving individual equations, the mode profiles can be found. The pursuit for analytical solution is limited to the fundamental mode for the practical interest. Higher order mode solutions are discussed in reference [76].

3.4.1 Bounded direction

Since the gain per wavelength is relatively small ($\beta_0 \gg \alpha_0$), it is reasonable to replace $k_0 k_{2x}$ with $\beta_0 \beta_{2x}$. The $k_0 k_{2x} x^2$ term indicates the field can be treated as being transmitted through a truncated lens-like media as in reference [82]. The fundamental solution to Eq. (3.33) is given by [78, 84]

$$X(x) = \exp\left(-\frac{x^2}{w_x}\right) \cdot {}_1F_1\left(\frac{t}{2} + \frac{1}{4}; \frac{1}{2}; \frac{2x^2}{w_x^2}\right), \quad -a \leq x \leq a \quad (3.35)$$

where ${}_1F_1$ function is Kummer confluent hypergeometric function with parameters $t/2 + 1/4$, 0.5 and $2x^2/w_x^2$; w_x is referred as the Gaussian spot size (field amplitude dropped to 1/e) of the mode in the corresponding unbounded quadratic media, and is expressed analytically as

$$w_x = \sqrt{2} (\beta_0 \beta_{2x})^{-0.25}. \quad (3.36)$$

Meanwhile, t is correlated with a_x , β_0 and β_{2x} as:

$$t = -a_x (4\beta_0 \beta_{2x})^{-0.5} \quad (3.37)$$

The expression given by Eq. (3.35). To illustrate the impact of thermal refractive focusing

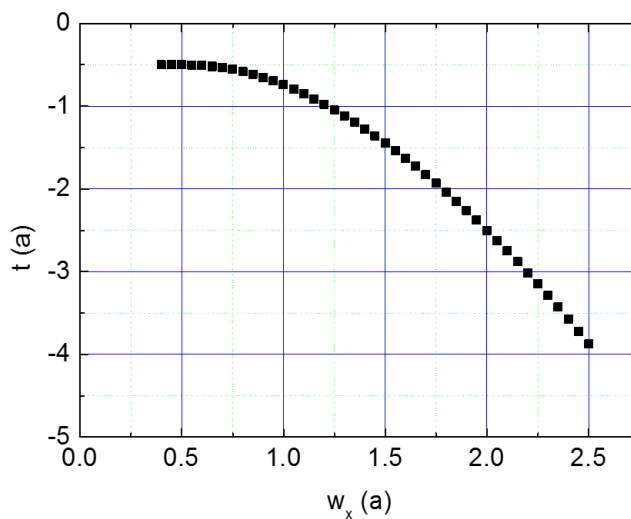


Figure 3-9. The typical values of t at given w_x in the unit of a .

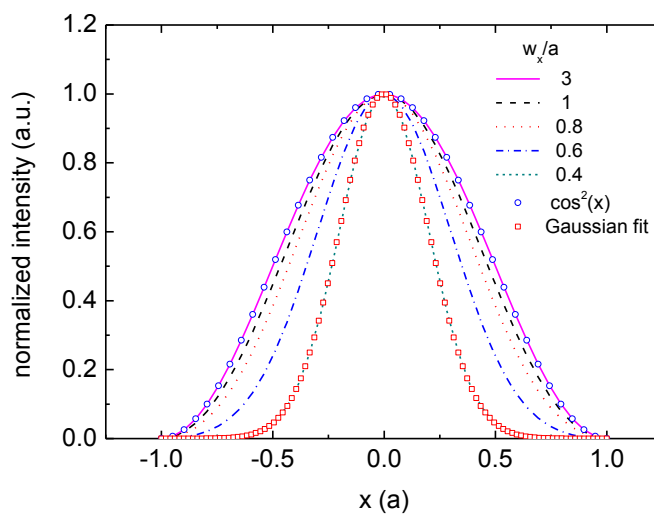


Figure 3-10. Intensity profile of fundamental mode along the bounded direction with different w_x . The blue dots is the cosine square shape while the red square is the Gaussian fit. w_x are taken to be 3, 1, 0.8, 0.6, 0.4 respectively [78].

on the mode profile, Eq. (3.35) is solved as follows. Due to ZFA, the field amplitude at the core-cladding interface is required to be zero, namely $X(a) = 0$. This condition is used to get parameter t at given w_x which is expressed in term a . The typical values of t are given in Fig. 3-9. The analytical expression for the mode field can then be calculated by substituting t and w_x into Eq. (3.35). The typical normalized mode intensity profiles at given w_x is calculated and shown in Fig. 3-10.

The intensity profiles in Fig. 3-10 indicate that the mode field changes its shape from cosine square shape to Gaussian shape when thermal refractive focusing becomes severe. This trends can be clearly pictured in Fig. 3-11, where the fundamental mode intensity FWHM is plotted. The horizontal axis represents the non-truncated intensity Gaussian width if there are no material boundaries. It is closely correlated with thermal refractive focusing as shown in Eq. (3.36). The FWHM approaches to a when w_x is sufficient large, which corresponds to the negligible thermal refractive focusing effect. The mode field shows the same width as cosine shape. It indicates that dominate guiding mechanism along the bounded direction remains to be index antiguiding. However, FWHM begins to shrink when w_x is reduced, which corresponds to the increasing thermal refractive focusing effects. The FWHM increase linearly with w_x when smaller than 0.75. This indicates that the mode profile changes from cosine shape to Gaussian shape with sufficiently large thermal refractive focusing effect. It is therefore determined that the dominated guiding mechanism switches from index antiguiding to thermal refractive focusing. The curved region in Fig. 3-11 indicates the transition of the guiding mechanism.

Previous theoretical analysis is applied to the 220 μm -thick core IAG planar waveguide laser. The detail laser configuration and experiment setups are explained in chapter 2. The near-field modes (illustrated in Fig. 3-12) are analyzed at both lasing

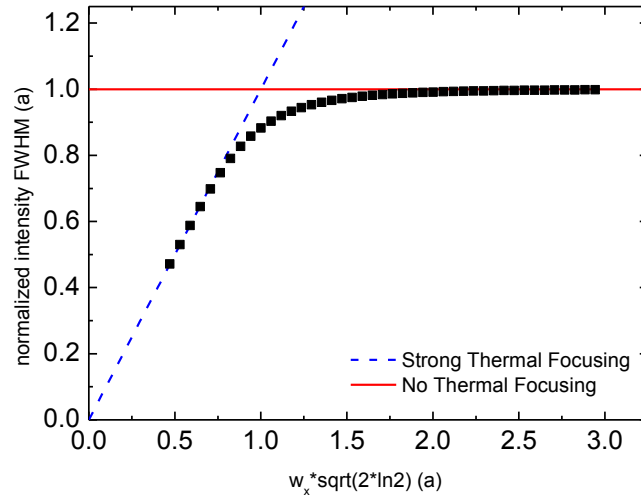


Figure 3-11. The intensity FWHM of fundamental mode at given $\sqrt{2 \ln 2} \cdot w_x$ (in the unit of a). The red line indicates the intensity width in absence of thermal effect while the blue dot line represents the line fitting

threshold ($P_{ab} = 0.8 \text{ W}$) and maximal lasing power ($P_{ab} = 5.75 \text{ W}$). It is worth mentioning that the data shown here was taken with the chip that the antireflection coating was not available. The coating increases power efficiency and stabilized the output lasing mode. Parameters used in the simulation is determined individually and given in table 3-2 [65]. The calculated $\beta_{2,x}$ are 507.5 cm^{-3} and 3648.0 cm^{-3} for $P_{ab} = 0.8 \text{ W}$ and $P_{ab} = 5.75 \text{ W}$ respectively. The intensity profiles along the bounded direction $|X(x)|^2$ are calculated accordingly and plotted in Fig. 3-13 [20], together with near-field mode and cosine square fitting.

Around the lasing threshold, the experiment results shows excellent agreement with

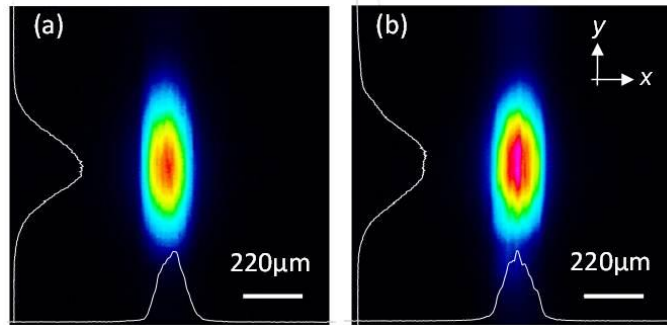


Figure 3-12. Near-field mode intensity profiles at (a) lasing threshold with $P_{ab} = 0.8\text{W}$ and (b) maximum lasing power with $P_{ab} = 5.75\text{W}$. The reflectivity of the output coupler used is 95%. The magnification factor is 3.5. The bounded direction is along the x -axis while the unbounded direction is along the y -axis.

Table 3-2. Parameters and corresponding value used for simulation

Parameters	Value	Parameters	Values
l_z	19.8 cm	f	0.3
r_p	250 μm	κ	$0.14 \text{ W cm}^{-1} \text{ K}^{-1}$
I_s	$2.9 \times 10^3 \text{ W cm}^{-2}$	dn/dT	$7.3 \times 10^{-6} \text{ K}^{-1}$
η_Q	0.95	λ	1.064 μm
η_B	0.278	η_s	0.76

both calculated $|X(x)|^2$ and cosine square fitting. This suggests the thermal refractive focusing is negligible while the mode field is guided by index antiguiding. At the maximum lasing power, however, the experiment results and fittings suggest the mode structure is still dominated by the index antiguiding. Though the calculated $|X(x)|^2$ is slightly

narrower than experiment results, it shows reasonable agreement with experiment data. The discrepancy is likely due to the heat cross-diffusion which is not considered during the modeling process. The weak heat diffusion along the y -axis reduces the temperature gradient along the x -axis. The limited spatial resolution of the near-field imaging system is believed to be cause of the broadening of experiment data around the core-cladding interface.

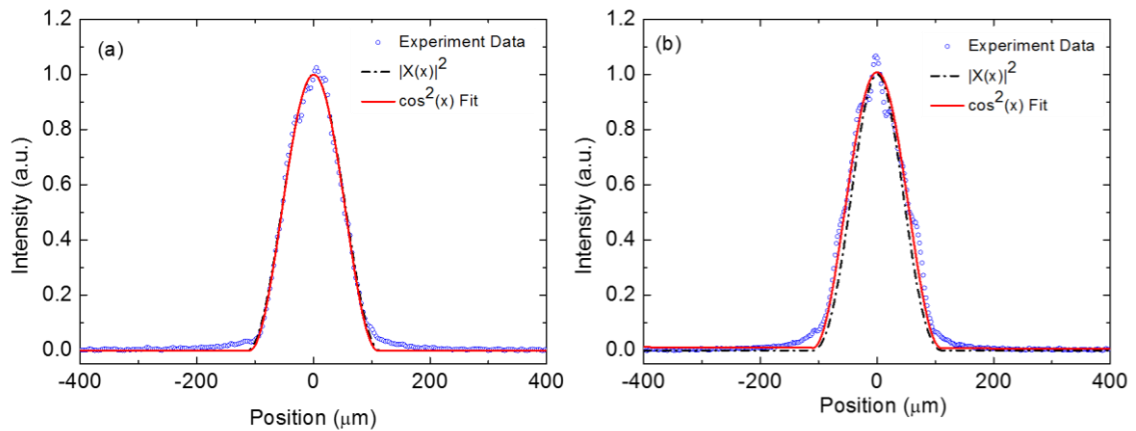


Figure 3-13. The intensity profiles cross-section (blue circles) along the x -axis at (a) $P_{ab} = 0.5W$ and (b) $P_{ab} = 5.75W$. Together with calculated $|X(x)|^2$ (black dash-dots) and cosine square fitting (red solid).

In conclusion, the fundamental mode field profile is calculated in presence of various thermal refractive focusing. The results show the transition of the mode field profile from cosine shape to Gaussian shape as thermal refractive focusing effect becomes dominate. This suggests the guiding mechanism transits from index antiguiding to thermal refractive focusing along the bounded direction of IAG planar waveguide. However, the experiment data suggests the mode is guided by index antiguiding with negligible thermal refractive focusing.

3.4.2 Unbounded direction

Along the unbounded direction, the mode field is affected by the thermal refractive focusing and quadratic gain focusing. For a weak thermal guiding which satisfies $a_x \ll k_0^2$ (as indicated by Fig. 3-9), Eq. (3.34) reduces to:

$$\frac{1}{Y(x)} \frac{\partial^2 Y}{\partial y^2} + \frac{1}{Y(x)} \frac{\partial^2 Y}{\partial z^2} + k_0 (k_0 - k_{2y} y^2) = 0 . \quad (3.38)$$

Eq. (3.38) describes a Gaussian beam propagating through a complex lens-like media [82, 85]. In order to get an analytical solution, it is assumed $Y(y, z)$ can be separated into $A(y)$ and $Z(z)$ as:

$$Y(y, z) = A(y)Z(z) = C_0 \exp\left(-i \frac{Q_y y^2}{2}\right) \cdot \exp(-iP_z - ik_0 z) , \quad (3.39)$$

where Q_y is steady-state complex beam parameter [86], which is linked with both Gaussian beam spot size along the y-axis w_y and the phase front curvature R_y as shown:

$$Q_y = \frac{\beta_0}{R_y} - i \frac{2}{w_y^2} . \quad (3.40)$$

P_z is a function with respect to z coordinate and C_0 is a constant. Therefore, the modal field along the propagation direction and along the y-axis are separated. By substituting Eq. (3.40) into Eq. (3.39) and requiring the coefficients of each order of derivatives be equal, one arrives at two important relationships as noted by:

$$Q_y = \left[-\beta_0 (\beta_{2y} + i\alpha_{2y}) \right]^{\frac{1}{2}} , \quad (3.41)$$

$$\frac{dP_z}{dz} = -i \frac{Q_y}{2\beta_0} . \quad (3.42)$$

The field amplitude along the y-axis is denoted by $|A(y)|$ and is related with β_{2y} , α_{2y} as:

$$|A(y)| = \exp\left(-\sqrt{\frac{\beta_0\beta_{2y} + \beta_0\sqrt{\beta_{2y}^2 + \alpha_{2y}^2}}{8}} \cdot y^2\right). \quad (3.43)$$

It is shown in Eq. (3.43) that the mode field along the unbounded direction is affected by both thermal refractive focusing and gain refractive focusing. Unlike along bounded direction, the mode field along unbounded direction is fixed to be Gaussian shape, the width of which is expressed as:

$$w_y = \left(\frac{-8\beta_{2y} + 8\sqrt{\beta_{2y}^2 + \alpha_{2y}^2}}{\beta_0\alpha_{2y}^2}\right)^{\frac{1}{4}}. \quad (3.44)$$

To illustrate impact of thermal refractive focusing and gain focusing on the mode field, the normalized width $w_y \cdot (\beta_0)^{0.25}$ is calculated with given β_{2y} and α_{2y} in Fig. 3-14. As shown in Fig. 3-14, the influence of the thermal refractive focusing on the width is stronger than the quadratic gain focusing. It is noted that the quadratic gain focusing or thermal refractive focusing alone can guide the mode with the Gaussian shape mode profile. This is reflected with the data points along the horizontal or vertical axis. In absence of quadratic gain focusing, the thermal refraction focusing transforms the step index waveguide to a quadratic refraction index waveguide. It is known that the width of the guided fundamental mode in such waveguide tends to shrink as the quadratic curvature increases [42].

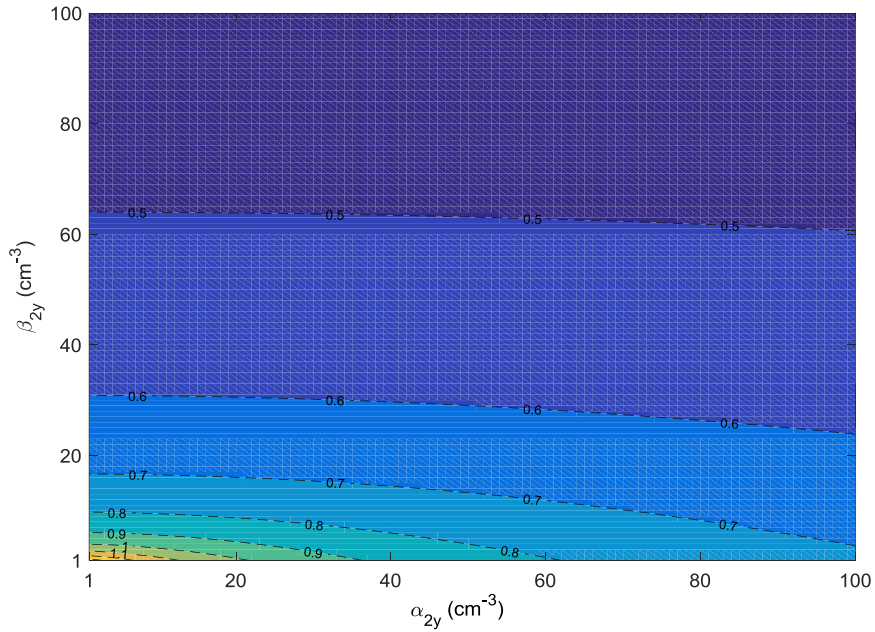


Figure 3-14. The contour plot of $w_y \cdot (\beta_0)^{0.25}$. Each point in contour plot represents a particular combination of gain and thermal refractive focusing.

Besides the shape of the mode field, the wavefront curvature is also of interest. The analytical expression of R_y is given by:

$$R_y = \left(\frac{2\beta_0\beta_{2y} + 2\beta_0\sqrt{\beta_{2y}^2 + \alpha_{2y}^2}}{\alpha_{2y}^2} \right)^{\frac{1}{2}}. \quad (3.45)$$

The normalized wavefront curvature $R_y / (\beta_0)^{0.5}$ is calculated with different β_{2y} and α_{2y} shown in Fig. 3-15. As shown, the influence of gain refractive focusing on R_y is larger than the thermal refractive focusing. This suggests, as appose to w_y , the wavefront curvature of the guide mode is mainly effected by the gain curvature.

The theoretical analysis is also applied to experiment but only around lasing threshold. This is because the higher order modes along the unbounded direction quickly

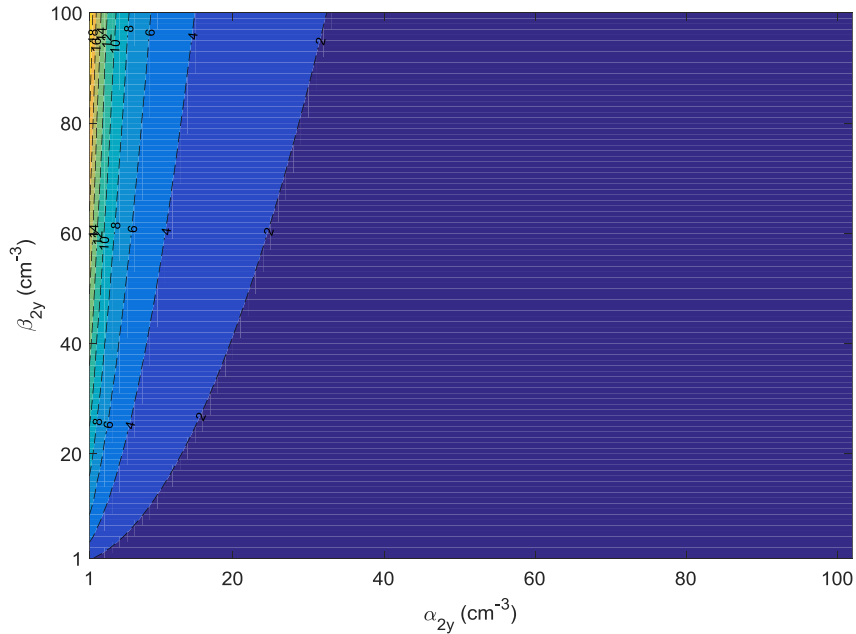


Figure 3-15. The contour plot of $R_y / (\beta_0)^{0.5}$. Each point in this plane represents a particular gain and thermal refraction focusing configuration.

reaches its lasing threshold. With the same parameter value in table 3-2, α_{2y} is calculated to be 22.7 cm^{-3} and β_{2y} is calculated to be 73.3 cm^{-3} with 0.8 W absorbed pump power.

The intensity profile along the y -axis with $P_{ab} = 0.8 \text{ W}$ is plotted in Fig. 3-16 together with the calculated normalized intensity profiles [20]. In order to compare the guiding mechanism, $|A(y)|^2$ with only α_{2y} and only β_{2y} are also plotted as reference.

Experiment results show the intensity shape along the y -axis is Gaussian shape, which agrees with the theoretical predication given by Eq. (3.43). The calculated $|A(y)|^2$ with only α_{2y} shows large deviation from the experiment while calculation results with β_{2y} alone shows reasonable agreement with the experiment results. This suggests that the mode is guided by thermal refractive focusing while the quadratic gain focusing has

negligible effects on it.

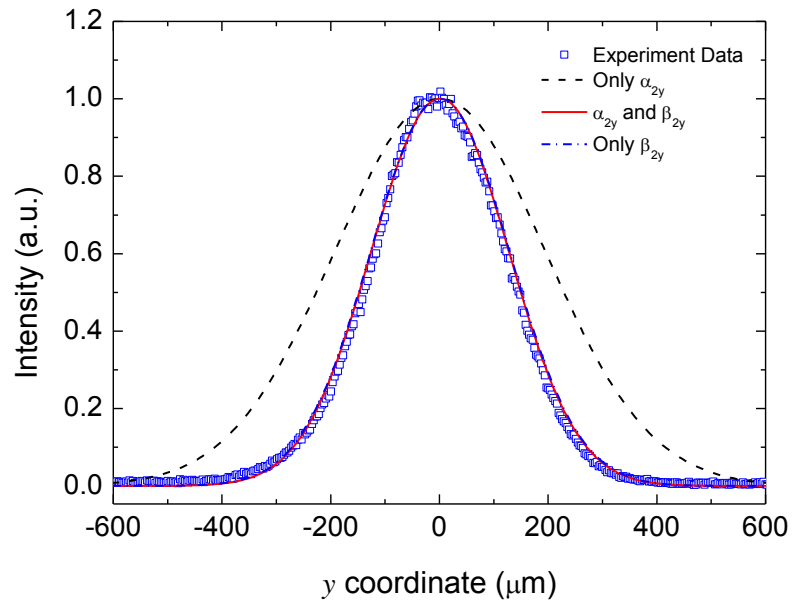


Figure 3-16 Experiment result of intensity profile along the y -axis together with calculation results with only α_{2y} , only β_{2y} and both α_{2y} and β_{2y} .

To conclude briefly, the analytical solution of fundamental mode field along the unbounded direction is derived. The width of the mode field profile is closely related with thermal refractive focusing and quadratic gain focusing. However, the formal factor shows greater influence on the mode profile which is verified by the experiment around the lasing threshold. It is concluded that along the unbounded direction, the mode profile is guided by the thermal refractive focusing with negligible quadratic gain guiding.

3.4.3 Quadratic modal loss

The propagation characteristics of the mode along the z -axis is dictated by P_z . A real P_z indicates the lossless propagation of the guided mode. However, due to the

quadratic gain focusing and thermal refractive focusing, a mixture of β_{2y} and α_{2y} appears in both real and imaginary parts of the complex P_z . The imaginary of P_z represents the attenuation of the mode intensity during propagation since $\alpha_{2y} > 0$. In order to express this attenuation, the modal loss coefficient along the y-axis α_m which is the imaginary part of P_z is calculated to be:

$$\alpha_m = - \left(\frac{-\beta_{2y} + \sqrt{\beta_{2y}^2 + \alpha_{2y}^2}}{8\beta_0} \right)^{\frac{1}{2}}. \quad (3.46)$$

α_m is the modal loss of the fundamental Gaussian mode along the y-axis when compared with uniform pumped case where $r_p \rightarrow \infty$ and $\alpha_{2y} \rightarrow 0$. The origin of this loss is quadratic distributed gain. Therefore in the following chapter, α_m is not treated as distributed loss coefficient when lasing power calculation is performed if the spatial distributed gain has been taken into consideration.

3.5 Summary

To sum up, the mode guiding theory inside the index-antiguinding planar waveguide laser is discussed in detail. The general index antiguinding theory is introduced using complex \tilde{v} number. Different region in the complex \tilde{v}^2 plane is explained in detail. From the practical stand point, other effects such as thermal refractive focusing and quadratic gain focusing are considered when the IAG planar waveguide is faced pumped. The simulation shows that the fundamental mode profile along the bounded direction transits from cosine shape to Gaussian shape when thermal refractive focusing begins to dominate. It is noted that the theory developed in this section can also be applied to any large-core waveguide lasers where ZFA applies. The experiment data based on 220 μm IAG chip

indicates the mode is guided by the index antiguiding with negligible thermal refractive focusing, which agrees with the simulation. Along the unbounded direction, however, the mode field is effected by both quadratic gain focusing and thermal refractive focusing. Experiment data around lasing threshold confirmed that the mode is guided by the thermal refractive focusing with negligible quadratic gain focusing.

CHAPTER 4 POWER CALCULATION BASED ON SPATIAL RATE EQUATIONS

4.1 Introduction

The power and efficiency of a laser are among the most important parameters. Optimization of such parameters sets the application range of a certain type of laser. Therefore, theoretical modelling on power and efficiency is of great importance, especially for novel laser media or structures. Due to the complexity of such modeling, seldom does an analytical model fit all the cases. Even though the proper model had been developed[1], analytical solutions from it is difficult to find. Numerical calculation requires approximation to make it practical, which may deviate the calculation results from the experiments observation [87].

Modeling of laser output and efficiency have been reported by many researchers [1, 87-92]. The major approaches can be grouped in to two categories [89]. One group of authors [87, 88, 90] incorporates the transverse profile of pump and lasing intensity in the intracavity intensity propagation equation. The output power is calculated by requiring the round-trip gain equals the round-trip loss. When the pump and lasing transition is relatively simple, the optical gain is easy to model, enabling simple calculation following this approach. It is even possible to get analytical solutions [87]. The other group of authors[1, 91] starts with rate equation which describes the interplay between population inversion density and cavity photon density. The profile information is taken into consideration by the modification of the densities in rate equations. For the gain media with complex lasing

transitions, such as Tm^{3+} [93] and alkali vapor [94], this approach provides reliable simulation results with numerical calculation. However, it is difficult to get analytical solutions. In addition, the numerical calculation usually requires advanced calculation capability to reduce the calculation time. It has been proved by Risk that these two approaches are equivalent [89].

The modeling for IAG lasers power performance are crucial for understanding the reported low power efficiency results. Many researchers reported the simulation results of IAG fiber lasers in end-pumping [62], uniform side-pumping [63] and multipoint distributed side pumping [95] configurations. The models in all these papers are based on the second approach and the temperature distribution inside the fiber was discussed as well. However, there is no experiment data for direct support for their models. The only experiment data of side-pumping shows large deviation from theoretical calculation [56, 57], weakening credibility of the model used.

The model discussed in this chapter follows the process in reference [89] with emphasis on face-pumped IAG planar waveguide lasers. It starts with the introduction of the spatial rate equations in section 4.2. Since pump and lasing transition of Nd^{3+} is well known, the focus of the model is on the evolution of intracavity intensity. The experiment data with 220 μm -thick-core IAG chip is discussed in section 4.3. Final remarks will be made in section 4.4.

4.2 Theory

The spatially dependent rate equation (SRE) is introduced in this section considering the profile of the pump irradiance and lasing output. The coordinate system used in this chapter is illustrated in Fig. 4-1, together with the pump and lasing geometry.

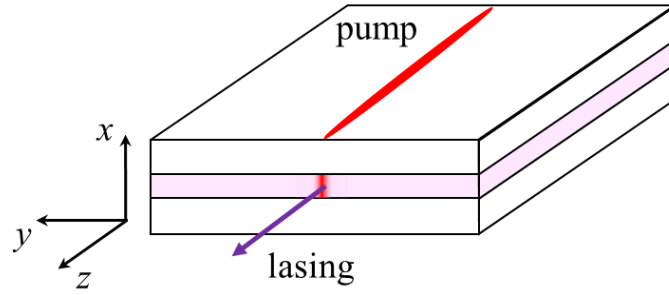


Figure 4-1. Face-pumped planar waveguide chip used in the modeling. The lasing takes place along the z -axis.

Before proceeding to detail mathematics, one important assumption is made here: the intensity profiles of the face-pumping footprint and the lasing in a given transverse plane do not change with incident pump power, lasing power, nor with given cavity mirrors. This is valid for only fundamental mode lasing along both x -axis and y -axis.

4.2.1 Spatial rate equation

Rate equation describes dynamic of the population inversion density and photon density inside a laser resonator. For continuous-wave lasers, steady-state solution is used to simulate the output power at given pump power. Due to the four-level system nature of Nd:YAG crystal, only laser upper and lower energy levels are considered in the following modeling. The population inversion density $\Delta N(x, y, z)$ inside the pumped waveguide core region and total number of cavity photon inside waveguide core Φ are expressed as [91]

$$\frac{d\Delta N(x, y, z)}{dt} = R \cdot r_p(x, y, z) - \frac{\Delta N(x, y, z)}{\tau_f} - \frac{c\sigma\Delta N(x, y, z)}{n} \Phi \cdot \phi_0(x, y, z), \quad (4.1)$$

$$\frac{d\Phi}{dt} = \frac{c\sigma}{n} \iiint \Delta N(x, y, z) \Phi \phi_0(x, y, z) dV - \frac{\Phi}{\tau_q}. \quad (4.2)$$

The normalized pump profile $r_p(x, y, z)$ and normalized lasing photon profile $\phi_0(x, y, z)$

satisfy:

$$\iiint r_p(x, y, z) dV = 1, \quad (4.3)$$

$$\iiint \phi_0(x, y, z) dV = 1. \quad (4.4)$$

To simplify the model, it is assumed that only FM presents in the output within the region of interests. The parameters in Eq. (4.1) and Eq. (4.2) are explained in table 4-1.

Table 4-1. Physical parameters used in rate equation

Parameter	Physical Meaning [unit]	Parameter	Physical Meaning [unit]
$Rr_p(x,y,z)$	Pump rate per unit volume	$\Delta N(x,y,z)$	Population inversion density [cm ⁻³]
τ_f	Lasing upper level fluorescence life time [s]	n	Refractive index of material
η_a	Pump power absorption coefficient	P_p	Incident pump power [W]
ν_L	Lasing frequency [Hz]	c	Speed of light in vacuum [m/s]
σ	Lasing cross section [cm ²]	Φ	Total number of lasing photon
$\phi_0(x,y,z)$	Lasing photon distribution function [cm ⁻³]	ν_p	Pump frequency [Hz]
τ_q	Cold cavity photon life time [s]	L	Cavity length [cm]

The pump rate R is related with η_a , P_p and ν_p through

$$R = \frac{\eta_a P_p}{h \nu_p}. \quad (4.5)$$

At steady state where $dN(x, y, z) / dt = 0$ and $d\Phi(x, y, z) / dt = 0$, $\Delta N(x, y, z)$ is

simplified to be:

$$\Delta N(x, y, z) = \frac{\tau_f R \cdot r_p(x, y, z)}{1 + \frac{\tau_f c \sigma}{n} \Phi \cdot \phi_0(x, y, z)} . \quad (4.6)$$

It is worth noting that the population inversion is reduced when total number of photon increases, which is often referred as gain saturation [65]. The intensity gain coefficient g (cm^{-1}) is related with σ and $\Delta N(x, y, z)$ through [67]

$$g(x, y, z) = \sigma \cdot \Delta N(x, y, z) . \quad (4.7)$$

Substitute Eq. (4.6) in to Eq. (4.7), the gain coefficient at spatial point (x, y, z) is given by:

$$g(x, y, z) = \frac{\sigma \tau_f R \cdot r_p(x, y, z)}{1 + \frac{\tau_f c \sigma}{n} \Phi \cdot \phi_0(x, y, z)} . \quad (4.8)$$

The small signal gain coefficient g_0 representing the maximal gain coefficient is derived from Eq. (4.8) by setting $\Phi = 0$:

$$g_0(x, y, z) = \sigma \tau_f R \cdot r_p(x, y, z) . \quad (4.9)$$

Eq. (4.9) represents the influence of incident pump and its profile on the spatial gain. The 1.064 μm transition of the Nd:YAG crystal is a well-known 4 level system. Therefore, the spectroscopic parameters are treated as constant, which helps simplify the model. It is, however, feasible to incorporate processes such as cross-relaxation or reabsorption of laser lower level if necessary by adding dependent parameters with σ and τ_f .

4.2.2 Intracavity intensity

To involve the intracavity intensity, consider a laser amplifier with $g(x, y, z)$ given in Eq. (4.8). The lasing intensity at each spatial point (x, y, z) within the amplifying media is given by [65]

$$\frac{dI(x, y, z)}{dz} = g(x, y, z)I(x, y, z) - \alpha_D I(x, y, z), \quad (4.10)$$

where α_D is the distributed intensity loss coefficient (cm^{-1}). Note that $I(x, y, z)$ and $\phi_0(x, y, z)$ are related through [91]

$$I(x, y, z) = \frac{ch\nu_L}{n} \Phi \phi_0(x, y, z). \quad (4.11)$$

Substitute Eq. (4.8) into Eq. (4.10) and the intensity propagation equation is transferred into:

$$\frac{dI(x, y, z)}{dz} = \frac{R_0 r_p(x, y, z) I(x, y, z)}{1 + sI(x, y, z)} - \alpha_D I(x, y, z), \quad (4.12)$$

where saturation intensity I_S and saturation factor s is linked by $I_S = h\nu_L / \tau_f \sigma = s^{-1}$; R_0 denotes how much pump power is transferred into lasing photon, and is expressed as $R_0 = \eta_a \eta_s P_p / I_S$. η_s is Stokes factor which denotes energy difference between pump and lasing photon. It is calculated through: $\eta_s = \nu_L / \nu_p$.

Eq. (4.12) describes the intracavity intensity propagation inside the gain media of a laser amplifier, the solution to which provides the insights of the power performance. The influence of the incident pump power on lasing intensity is represented by the produce of R_0 and $r_p(x, y, z)$. This product is the small-signal gain at a spatial point. It is shown that both the magnitude and profile of incident pump has the potential to effect the lasing intensity. Meanwhile, the overlap between lasing profile and pump profile is represented by the product of $I(x, y, z)$ and $r_p(x, y, z)$. This produce determines the saturation level at which the energy is extracted out from the population inversion to lasing photons. It has been shown theoretically that this profile overlap (often referred as mode overlap), if

ignored, leads to dramatic deviation of the slope efficiency simulation [87].

Besides the gain and profile overlap, distributed loss in Eq. (4.12) is another interesting topic. The term “distributed loss” used in this chapter refers to the loss mechanism which causes the intracavity intensity drops exponentially. The major distributed loss inside the IAG chip is the leaky loss due to IAG structure, which can be calculated based on the waveguide design parameters as discussed in chapter 3. The scattering loss due to the impurity inside the waveguide core can be treated as distributed loss as long as the scattering process happened randomly. Another major loss mechanism in IAG planar waveguide lasers (PWL) is the coupling loss due to the gap between waveguide facets and cavity mirrors. Unlike the distributed loss, it effects the circulating intensity only at discretized locations along the z -axis. Calculation of the coupling loss in a waveguide and its influence on laser output power were reported by many researchers [38, 39, 96, 97]. The focus of these researches were made on metal waveguide CO₂ lasers and with curved mirrors. It is appropriate to apply the theory to IAG PWL as long as ZFA holds. The detail discussion of the coupling loss will be presented in chapter 5 with planar waveguide and fiber geometry. The coupling loss in this chapter is treated as the effectively reduction of mirror reflectivity following the ref [18, 98].

4.2.3 Output power calculation

To involve the lasing intensity profiles, consider the normalized transverse lasing intensity profile $f(x, y)$ which does not change longitudinally. The lasing power at given longitudinal position $P(z)$ inside the gain media is then expressed as [99]

$$P(z)f(x, y) = I(x, y, z), \quad (4.13)$$

where

$$\iint f(x, y) dx dy = 1. \quad (4.14)$$

Note that $f(x, y)$ is the intensity profile inside the waveguide core for IAG PWL. The propagation equation of $P(z)$ is found by integrating Eq. (4.12) in $x - y$ plane:

$$\frac{dP(z)}{dz} = \frac{\eta_a \eta_s P_p}{I_s} \iint \frac{r_p(x, y, z) f(x, y)}{1 + sP(z) f(x, y)} dx dy P(z) - \alpha_D P(z). \quad (4.15)$$

The power gain coefficient $G(z)$ can therefore be extracted from Eq. (4.15):

$$G(z) = \frac{dP(z)}{P(z) dz} = \frac{\eta_a \eta_s P_p}{I_s} \iint \frac{r_p(x, y, z) f(x, y)}{1 + sP(z) f(x, y)} dx dy. \quad (4.16)$$

In a laser resonator, both forward propagation (towards the output coupler) intracavity power $P^+(z)$ and backward propagation (towards the high reflector) intracavity power $P^-(z)$ are involved in the gain saturation process [100]. When the intracavity lasing power is large enough, $P^+(z)$ and $P^-(z)$ can be approximated to be the same constant P_0 . Above lasing threshold, the round trip power gain should be enough to overcome the power loss and mirror loss. To express this mathematically, integrate Eq. (4.16) from 0 to cavity length L two times:

$$2 \int G(z) dz = -\ln R_1 R_2 + 2\alpha_D L, \quad (4.17)$$

where R_1 and R_2 are the reflectivity of left (high reflector) and right (output coupler) cavity mirror respectively. Given Eq. (4.16), Eq. (4.17) is expressed as

$$\frac{\eta_a \eta_s P_p}{I_s} \iiint \frac{r_p(x, y, z) f(x, y)}{1 + 2sP_0 f(x, y)} dx dy dz = -\frac{1}{2} \ln R_1 R_2 + \alpha_D L. \quad (4.18)$$

Eq. (4.18) shows the relationship between P_0 and P_p when pump and lasing photon

profiles are considered to be spatially distributed. The following observations are made:

1. The intracavity lasing power will be affected by the spatial distribution of incident pump power. This is reflected by the spatial integral in Eq. (4.18).
2. $f(x, y)$ is assumed to be invariant longitudinally. This is true when only fundamental mode presents in the output. However to involve the transverse mode competition (discussed in the chapter 5), more rigorous model, for instance Rigrod analysis, has to be used in laser power calculation. In addition, the intensity in the waveguide cladding is ignored. It is believed the lasing signal inside the cladding has fewer change to couple back into the core for amplification. Therefore, it can not resonate.
3. The longitudinal spatial hole-burning due to the interference between forward and backward propagation of the laser field is not being considered in previous modeling process.

The output power $P_{out} = P_0(1 - R_2)$ at given pump power can be solved numerically if $r_p(x, y, z)$ and $f(x, y)$ are known. Other important efficiency parameters such as slope efficiency or optical efficiency can be determined by scanning P_p within in the region of interest. The threshold pump power P_p^{th} can also be determined by assuming P_0 to be zero:

$$\frac{\eta_a \eta_s P_p^{th}}{I_s} \iiint r_p(x, y, z) f(x, y) dx dy dz = -\frac{1}{2} \ln R_1 R_2 + \alpha_p L. \quad (4.19)$$

The integral inside Eq. (4.19) represents the overlap between pump and lasing profiles. Its impact on the lasing threshold is obvious. However for waveguide lasers where $f(x, y)$ is fixed by the waveguide structure, the optimization of this integral relays on shaping $r_p(x, y, z)$. It is equivalent for choosing the proper pumping scheme. As discussed

previously, the reflectivity of the cavity mirrors are reduced to $R_1\Gamma_1$ and $R_2\Gamma_2$ respectively considering the coupling loss.

4.3 Experiment results and discussion

The theory discussed in previous sections has been applied to the lasing experiment with only 220 μm -thick-core IAG PWL. The experiment setups are discussed in chapter 2, along with the pump and lasing profile.

4.3.1 Pump absorption

Though narrow, the pump laser has certain spectral profile as shown in Fig. 4-2. So does the absorption of pump radiance given by Fig. 4-3. Considering the gain media has a wavelength dependent absorption coefficients (cm^{-1}) expressed as $\alpha_p(\lambda)$. The pump power is expressed as $P_p(\lambda)$. Since the pump area has been fixed, $P_p(\lambda) \propto I_p(\lambda)$ where $I_p(\lambda)$ is the spectral profile of the pump radiance. The transmitted pump intensity after passing through the gain media with a length of L at wavelength λ_0 is expressed as $I_p(\lambda_0)\exp[\alpha_p(\lambda_0)L]$. After integration over the spectral range of the pump laser, the power transmission (in term of percentage) is given by

$$T = \frac{\int I_p(\lambda)\exp[\alpha_p(\lambda)L]d\lambda}{\int I_p(\lambda)d\lambda} . \quad (4.20)$$

The length of the gain media along the pumping direction is short (220 μm) compared with absorption length (10 cm at its peak shown in Fig. 4-3). It is reasonable to assume that $L = 220 \mu\text{m}$. The scattering loss is assumed to be zero. The calculated absorption (in terms of percentage of incident pump power) is expressed as

$$A = 1 - \frac{\int I_p(\lambda) \exp[\alpha_p(\lambda) 2a] d\lambda}{\int I_p(\lambda) d\lambda} . \quad (4.21)$$

According to Eq. (4.21), the calculated single-pass transmission for the pump is 0.9068.

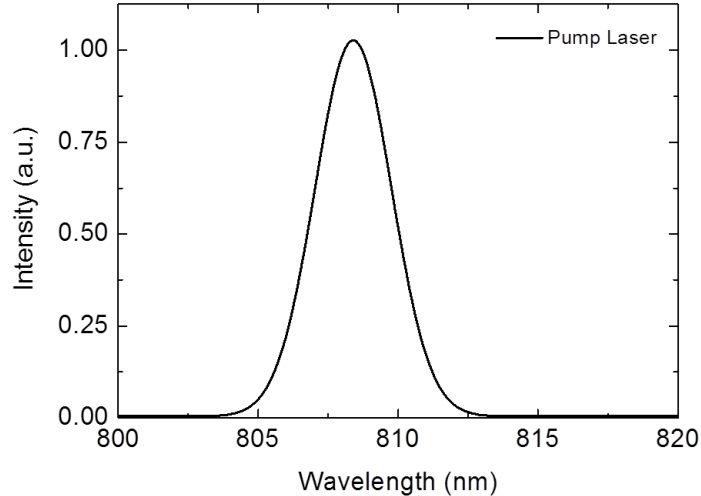


Figure 4-2. Lasing spectral of pump diode at 44.0A inject current and 24.0 C. The output lasing has a wavelength centered at 808.5 nm with a Gaussian shape with 3.8 nm FWHM. The pump spectral is measured by a grating-CCD based spectrometer (Avantes).

Experiment has been done to measure the single pass pump power absorption. The output of the pump diode laser is collimated and incidents on the IAG planar waveguide whose core is 220- μm -thick. The transmitted power is collected by a power meter (Melctron LM30). The single-pass transmission is determined to be 0.8946, which shows good agreement with theoretical calculation. As discussed in chapter 2, the Indium foil between the chip and the heat sink is treated as a mirror for the pump light. The reflected pump radiance is absorbed by the gain medium as well. Given this, the double pass pump power absorption is assumed to be 0.2. It is worth noting that the influence of the overlap

between pump spectral profile and gain media absorption spectral profile on the absorption of pump power is significant. Efforts of precisely controlling the pump spectral should be taken into consideration when optimizing the absorption of the pump power. This is especially critical when diode laser serves as the pump source.

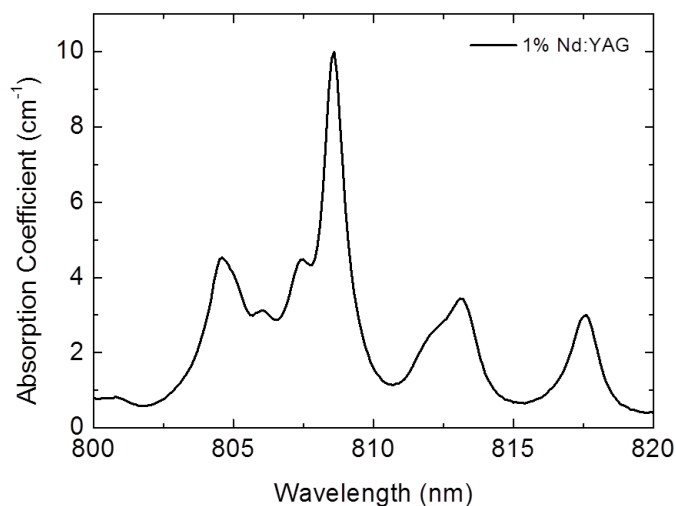


Figure 4-3. Absorption coefficient (cm⁻¹) of 1% Nd:YAG crystal. The graph shows the maximal absorption coefficient locates at 808.5 nm with multiple peaks. (Countersy of SYNOPTICS)

4.3.2 Pump spatial profile

The pump spatial profile, or pump footprint, is measured by placing the beam profiler at the focal plane of the cylindrical lens and translating the profiler along the z -axis. The pump profile along the y -axis is read out directly from the profiler while multiple profiles are stitched to form the profile along the z -axis. Due to the short length along the x -axis, the pump is assumed to be uniform. The measured results are shown in Fig. 4-4.

The fittings in Fig. 4-4 indicate the pump profiles are parabola shape along the y -

axis and z -axis. Therefore, $r_p(x, y, z)$ is expressed as

$$r_p(x, y, z) = \frac{9}{32(l_z \cdot r_y \cdot a)} \left(1 - \frac{4z^2}{l_z^2} \right) \left(1 - \frac{y^2}{r_y^2} \right), \quad (4.22)$$

where r_y and l_z are the half-width at null intensity (HWNL) along the y -axis and z -axis

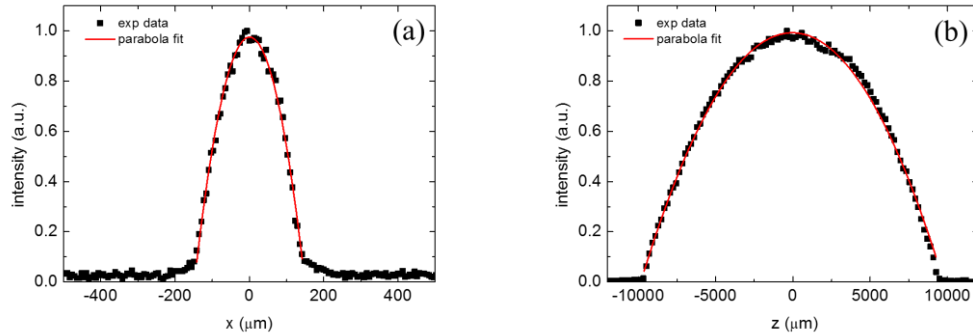


Figure 4-4. Pump spatial profiles along (a) y -axis and (b) z -axis. The experiment data are fitted with parabola shape.

respectively, which are determined to be $145 \mu\text{m}$ and 9.9 mm experimentally. It is worth noting that the pump expression can be modified for end-pumping by considering the intensity attenuation along the z -axis as in reference [101]. It is also noted that the model mentioned above can be tailored to fit in the end pumping case with minor revision.

4.3.3 Lasing profile

The lasing mode is measured by near-field (NF) imaging as discussed in chapter 2. A plano-convex lens (singlet) with 100 mm focal length is used to image the lasing facet onto the beam profiler. The variable attenuator is added before the profiler to avoid saturation. The magnification factor is 6.2 . The lasing mode intensity profile along the x -axis is verified to be cosine square shape while along the y -axis, it is Gaussian shape as

discussed in chapter 2.

The lasing modes are then taken at a variety of incident pump power with 5 different output couplers, the reflectivity (R_{oc}) of which are 0.95, 0.9, 0.7, 0.5 and 0.3. The typical near-field mode profile is given in Fig. 4-5. The intensity profile along the x -axis shows good fitting with cosine square shape during the experiment with all the output couplers at all the pump levels. This indicates, as discussed in chapter 3, that robust single mode operation is achieved along the bounded direction. The intensity profile along the y -axis shows a Gaussian shape, which is consistent with discussion in chapter 2. $f(x, y)$ is therefore expressed as:

$$f(x, y) = F(x)G(y) = \frac{1}{aw\sqrt{\pi/2}} \cos^2\left(\frac{\pi x}{2a}\right) \exp\left(-\frac{2y^2}{w^2}\right). \quad (4.23)$$

It is worth noting that the Gaussian width w (half width at field drops to 1/e of its maximum) changes with the pump power and with the output couplers. This is believed to be the

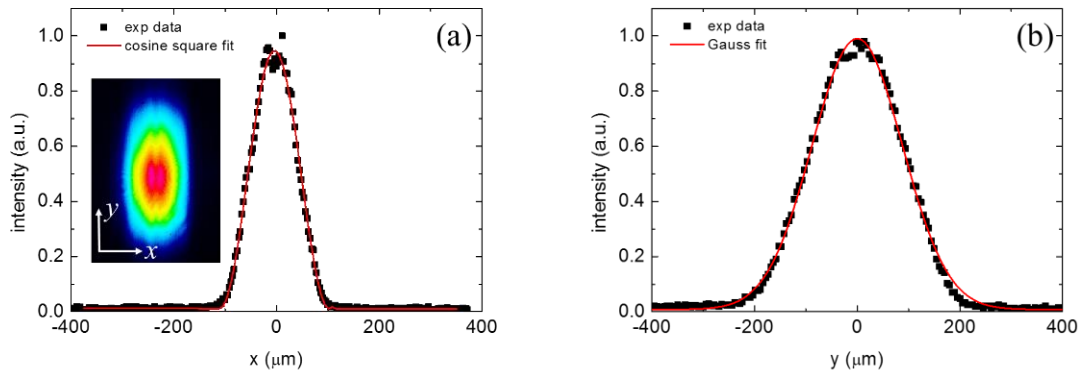


Figure 4-5. Intensity profile at 2.0W lasing power with $R_{oc} = 0.95$ output coupler along (a) x -axis and (b) y -axis. The profile along the x -axis is fitted with cosine square (red line) while the profile along the y -axis is fitted with Gaussian shape (red line). The inset in (a) is the typical near-field mode throughout the experiment.

consequence of thermal refractive focusing. For the power calculation purpose, however, the intensity profile along the y -axis is fitted with Gaussian shape and the averaged fitted w for each output couplers are used in Eq. (4.23).

4.3.4 Output power and efficiency

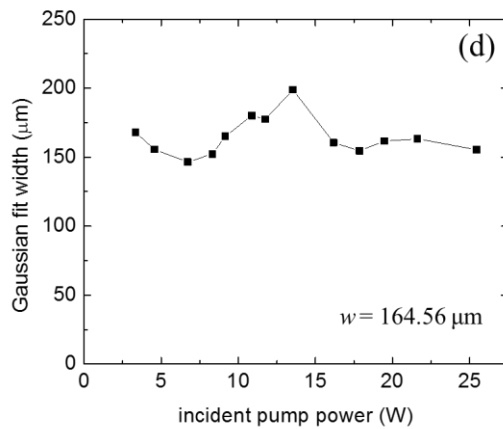
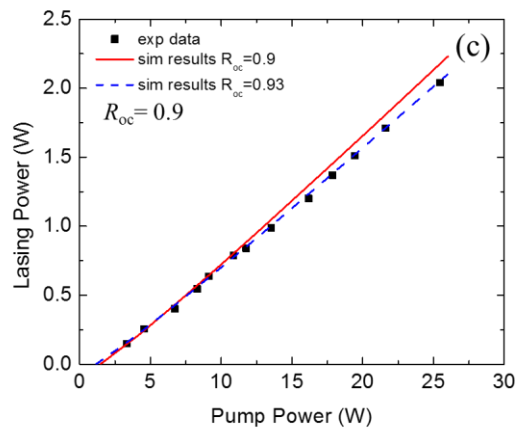
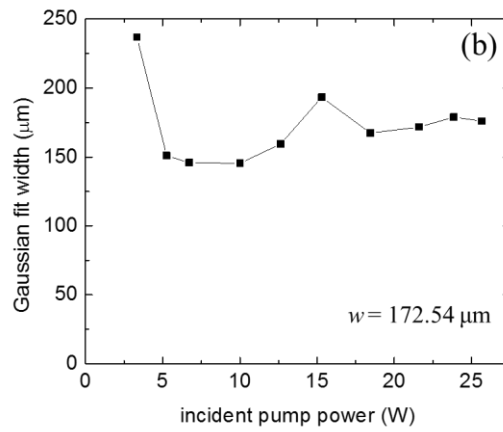
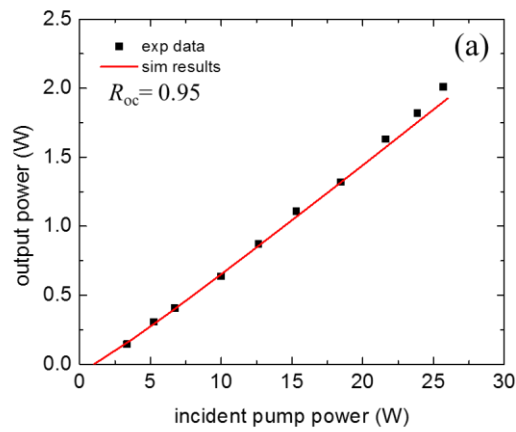
Prior to the calculation of lasing power, the loss inside the cavity needs to be specified and calculated. As discussed before, two major optical loss mechanism are being considered: the distributed loss and the coupling loss. The distributed loss is associated with waveguide design parameters and it scales as the square of the modal order [69]. As far as fundamental mode is concerned, the intensity loss coefficient is calculated to be $8.2147 \times 10^{-4} \text{ cm}^{-1}$. The coupling loss, on the other hand, is evaluated numerically based on free space diffraction and modal overlap integral [38, 98]. The gaps between crystal facet and cavity mirror is 2.7 mm on the high reflector side and the same on the output coupler side. The coupling loss due to this gap is treated as the reduction of reflectivity of cavity mirrors. The coupling efficiency is calculated to be 0.99. Detail explanation of the coupling loss can be found in chapter 5. The output power is defined as

$$P_{out} = (1 - R_2)P_0 . \quad (4.24)$$

To calculate P_{out} at given P_p , Eq. (4.18) is solved numerically by self-consistently searching for P_0 when other parameters are known. This is realized in MATLAB. Other parameters used in the calculation are listed in table 4-2. The experiment data and simulation results with different output couplers are given in Fig. 4-6.

Table 4-2. Parameters used to solve Eq. (4.18)

Parameter	Value	Parameter	Value
α_D	$8.2147 \times 10^{-4} \text{ cm}^{-1}$	I_s	$2.9 \times 10^3 \text{ W/cm}^2$
η_s	0.759	η_a	0.20
L	19.8 cm	a	110 μm
r_p	$145 \times 10^{-4} \text{ cm}$	R_1	0.99



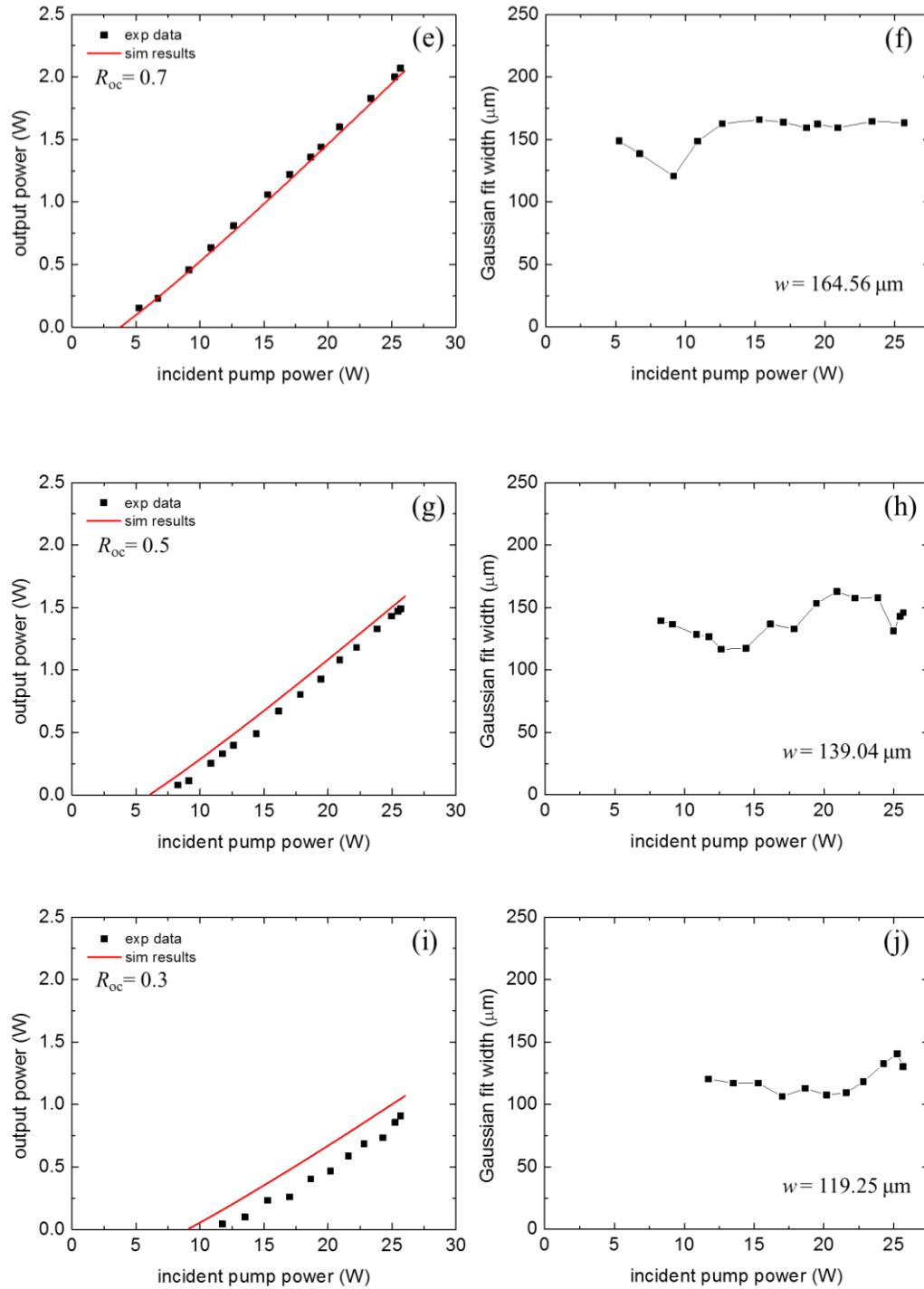


Figure 4-6. Experiment data and simulation results for lasing power at different incident pump power with (a) $R_{oc} = 0.95$, (c) $R_{oc} = 0.9$, (e) $R_{oc} = 0.7$ (g) $R_{oc} = 0.5$ and (i) $R_{oc} = 0.3$. The fitted w at different incident pump power are given with (b) $R_{oc} = 0.95$, (d) $R_{oc} = 0.9$, (f) $R_{oc} = 0.7$ (h) $R_{oc} = 0.5$ and (j) $R_{oc} = 0.3$. The number marked at the lower bottom

is the number used in the corresponding simulation. The blue dash line in (c) represents the simulation results with $R_{oc} = 0.93$.

The simulation results show good agreement with experiment data for $R_{oc} = 0.95$ and $R_{oc} = 0.7$ cases. However, for $R_{oc} = 0.9$ case, the simulation results with increased reflectivity of the output coupler shows good agreement with experiment data. It is believed that this is due to the degradation of the dielectric coating of the very output coupler used in the experiment. The dielectric coating on the primary surface of this output coupler has the discernable color variation. The microscope image reinforced this observation with additional black dots randomly scattering across the field of view. The size of the black dot is estimated to be $1 \mu\text{m}$ in diameter. Based on these facts, the attempt to using other reflectivity in the simulation is justified. The actual influence of this coating degradation on the reflectivity of the output coupler is difficult to analyze since it requires detail receipt of the coating. For practical consideration, the reflectivity is changed around the nominal value in the effort for the best simulation results. As shown in Fig 6. (c), the reflectivity is chosen to be 0.93 (blue dash curve). The simulation results for $R_{oc} = 0.5$ and $R_{oc} = 0.3$ cases show increasing deviation from the experiment data. This deviation is believed to be the results of the assumptions made previously that the forward and backward intracavity intensity is the same inside the waveguide core. This approximation is valid for large R_{oc} . However, the difference between forward and backward intracavity intensity becomes large for small R_{oc} .

Experimentally, the maximal slope efficiency is 10.3% (51.5%) with respect to incident (absorbed) pump power when the output coupler with 70% reflectivity is used. It

is the highest slope efficiency with only FM operation for IAG lasers to our knowledge. In addition, this is the highest slope efficiency for CW operation of IAG lasers as well. The simulated input-output curves show slightly deviation from a perfect straight line, especially around lasing threshold. This can be understood from Eq. (4.18) qualitatively. As P_p increases, P_0 gradually prevails the denominator. For the limiting case where $sP_0f(x, y) \gg 1$, the slope efficiency reduces to the well-known form:

$$\frac{P_o(1-R_{oc})}{P_p} = \frac{\eta_a\eta_s(1-R_{oc})}{-\ln R_{oc} + 2\alpha_D L}. \quad (4.25)$$

According to Eq. (4.25), the slope efficiency is proportional to η_a . The current face-pumping setup allows the pump beam effectively passing through the gain media twice. η_a can definitely be increased by letting the pump beam pass through the gain medium multiple times. This technique has been applied to the disk laser for long time, where the single-pass absorption of the pump can be even smaller than the face-pumped IAG PW lasers discussed above [4, 102]. The remaining challenges are the effective pump beam shaping and the effective heat removal. Eq. (4.25) also suggests a smaller $\alpha_D L$ favors higher slope efficiency. However, this is with the risk of introducing the adjacent higher order transverse mode. Besides this concern, the optimization of the slope efficiency in this case has no difference than a standard laser, which has already been discussed in standard laser textbooks such as references [65, 67]: there will be an optimal reflectivity for the output coupler when $\alpha_D L$ is fixed. This can be carried out by taking the derivatives of the R_{oc} on the right-hand side of Eq. (4.25).

4.4 Summary

In summary, a theoretical model on calculating the laser output power is introduced

and then applied to the face-pumped IAG PW lasers in this chapter. The model is based on spatial rate equation, where pump and lasing intensity profiles are taken into consideration. The simulated results and experiment data are shown in good agreements. The maximal slope efficiency is 10.3% (with respect to the incident pump power) observed with 70% reflectivity output coupler. This is, as far as we know, the highest slope efficiency with IAG structure in CW operation for IAG lasers. Throughout the experiment, the lasing profiles along the x -axis shows good fitting with cosine square shape, indicating robust single mode operation in 220 μm IAG chip. Based on all these facts, the IAG lasers shows the potential to achieve high power CW operation with large-mode-area and only fundamental mode.

CHAPTER 5 TRANSVERSE MODE COMPETITION INSIDE INDEX-ANTIGUIDED WAVEGUIDE LASER

5.1 Introduction

In step-index optical waveguides, the material interface imposes boundary conditions on the propagation modes. This leads to a set of well-defined transverse electromagnetic wave pattern [103]. For instance, the modal amplitude profiles inside the core of a 1-D waveguide structure are cosine or sine shape with specified modal order [104, 105]. Without perturbation and certain phase relationship, the intensity cross-talk between two adjacent propagation modes is zero due to orthogonality [106]. When optical gain is added in the core, the amplitude of individual transverse mode is amplified according to its intensity profile. This amplification process is, however, subject to the gain saturation due to the finite population inversion. In small signal limit where gain saturation is negligible, the amplification of each transverse mode can still be treated individually and the intensity cross-talk can be ignored. However, the gain saturation becomes noticeable as the amplitude of each transverse mode increases since the locally available gain is depleted by the sum of all transverse modes. The amplification of the modes begins to effect each other through competing the available gain. In presence of the modal discrimination factors, for example modal loss, the amplitude of each transverse mode, consequently the output power, becomes correlated. This phenomenon is referred as transverse mode competition (TMC) in the sense that transverse modes compete for the gain media to oscillate.

The depleted gain reflects the footprint of lasing modes in a transverse plane (plane perpendicular to the optical axis), which is often referred as transverse hole-burning effect [87]. Besides in laser amplifiers, TMC is also found in laser resonators where the gain media is saturated by both forward and backward propagation intracavity signals. The lasing threshold of the higher order modes (HOM) can then be treated as the consequence of TMC in lasers, which affects both power efficiency and output beam quality.

In free-space lasers, TMC led by gain saturation becomes less noticeable because the pump profile can be tailored to efficiently excite fundamental transverse mode (FM) by increasing the overlap efficiency [65]. For example in diode end-pump solid-state lasers, the pump spatial profile is designed such that it has the maximal overlap with the fundamental transverse lasing mode [91]. This strategy is proved to be effective in maintaining high power efficiency and suppressing HOMs for excellent output beam quality [89, 90]. However, in waveguide lasers, the pump geometry and lasing profiles are fixed by the waveguide geometry. Hence, TMC due to gain saturation has the potential to prevail other effects in determining the threshold of 1st HOM, which eventually determines the output power and beam quality [107, 108].

For IAG planar waveguide lasers in particular, the large refractive index difference and large core thickness lead to a small propagation loss. This favors the lossless propagation of HOMs in general. However, lossless propagation does not guarantee the resonance of HOMs due to TMC. Researchers have reported the behavior of TMC in fiber geometry where only qualitatively analysis was presented [109]. However, few reports about TMC in planar waveguides which is the motivation for this chapter to develop a model describing TMC inside IAG lasers considering practical parameters such as modal

loss, reflectivity of cavity mirrors, etc. And it is also important that this model can be extended to other laser geometries with proper modification. In addition, effects of design parameters on the overall performance of a particular IAG lasers can be extracted by numerically exploring different design combinations based on the model. In this way, valuable design suggestions can be made.

In this chapter, the coupling loss in waveguide lasers is firstly explained in both planar waveguide and cylindrical fiber geometry in section 5.2. In section 5.3, the transverse mode competition theory is developed and is applied to the planar waveguide. Due to the limitation of experiment samples, only planar waveguide case is explored experimentally. In chapter 5.4, performance matrix is proposed and optimization of the laser output is performed in both planar waveguide and optical fiber. Summary is made in section 5.5.

5.2 Coupling loss in waveguide laser

The confined propagating modes tend to diffract when exiting the waveguide. When mirrors instead of waveguide facets are used as cavity mirrors, the diffracted field has to couple back into the waveguide in order to resonate. The energy loss in this process is referred as coupling loss, which is well-known to be modal dependent and has been demonstrated to be useful for modal discrimination [18]. There are many researchers who reported the coupling loss in rectangular metal waveguides [38, 97, 110, 111]. In this section, theoretical calculation of the coupling loss is demonstrated.

5.2.1 General theory

There are two major approaches to calculate the coupling loss, one is to decompose the waveguide modes into free-space Gaussian modes and calculate the coupling loss for

each Gaussian modes [38]; the other one is to evaluate the diffraction integral directly [112].

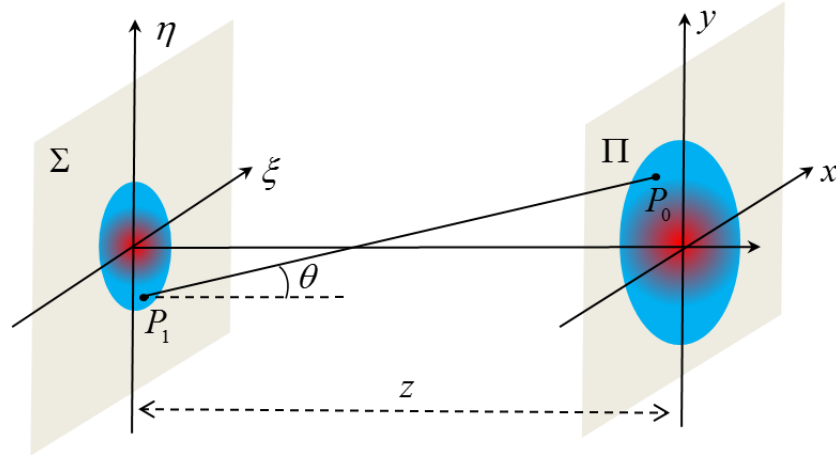


Figure 5-1. Schematic drawing of the free space diffraction.

In this section, the coupling loss calculation follows the second approach. The principle for calculation is illustrated in Fig. 5-1. Assume the mode field at the waveguide facet surface Σ is $U(\xi, \eta)$ while the diffracted field at the detector plane Π is $U'(x, y)$. The distance between plane Σ and Π is z , which is much larger than the wavelength.

$U'(x, y)$ is related with $U(\xi, \eta)$ through Fresnel integral [113]:

$$U'(x, y) = \frac{z}{j\lambda} \iint_{\Sigma} U(\xi, \eta) \frac{\exp(jkr_{01})}{r_{01}^2} d\xi d\eta, \quad (5.1)$$

where k is the wavenumber, λ is the vacuum wavelength and r_{01} is the distance between point P_1 on the source plane and P_0 on the detector plane: $r_{01} = \sqrt{z^2 + (x - \xi)^2 + (y - \eta)^2}$.

Detail explanation can be found in reference [114]. The reflected field is then coupled into the original field. The intensity modal coupling efficiency Γ is given by [96]:

$$\Gamma = \left| \frac{\left(\iint U^{r*}(x, y)U(x, y)dxdy \right)^2}{\left(\iint U^*(x, y)U(x, y)dxdy \right) \left(\iint U^{r*}(x, y)U'(x, y)dxdy \right)} \right|. \quad (5.2)$$

$(1 - \Gamma)$ is the loss factor that denotes how much energy is lost during a single coupling process. It is worth noting that Eq. (5.2) reflects the coupling happened within the same modal order. In reality, mode cross coupling is possible. For practical interest, however, only fundamental mode and first higher order mode are considered in this chapter and the mode cross-coupling is ignored.

5.2.2 Coupling loss in planar waveguide lasers

As shown in chapter 3, the fundamental mode profile along the x -axis is cosine shape while the mode profile remains Gaussian shape along the y -axis. The Rayleigh range is larger than the gap distance, leading to the assumption that the mode profile along y -axis is constant after bouncing back from the cavity mirror. The coupling loss only is evaluated along the x -axis for the planar waveguide. In IAG planar waveguide laser, according to ZFA (discussed in chapter 3), the normalized field profile along the x -axis for the FM ($U_{FM}(x)$) and 1st HOM ($U_{HOM}(x)$) are given respectively by

$$U_{FM}(x) = \frac{1}{\sqrt{a}} \cos\left(\frac{\pi x}{2a}\right), \quad -a \leq x \leq a, \quad (5.3)$$

$$U_{HOM}(x) = \frac{1}{\sqrt{a}} \sin\left(\frac{\pi x}{a}\right), \quad -a \leq x \leq a, \quad (5.4)$$

where a is the half thickness of the waveguide core. The intensity profile of FM and 1st HOM are then expressed as

$$f_1(x) = \frac{1}{a} \cos^2\left(\frac{\pi x}{2a}\right), \quad -a \leq x \leq a, \quad (5.5)$$

$$f_2(x) = \frac{1}{a} \sin^2\left(\frac{\pi x}{a}\right), \quad -a \leq x \leq a . \quad (5.6)$$

After leaving the waveguide facet, the mode field diffracts as illustrated in Fig. 5-2. When coupled back into the waveguide core after diffracts twice the distance of the gap, part of the energy is coupled into the cladding. The intensity modal coupling efficiency reduces to 1-D integral:

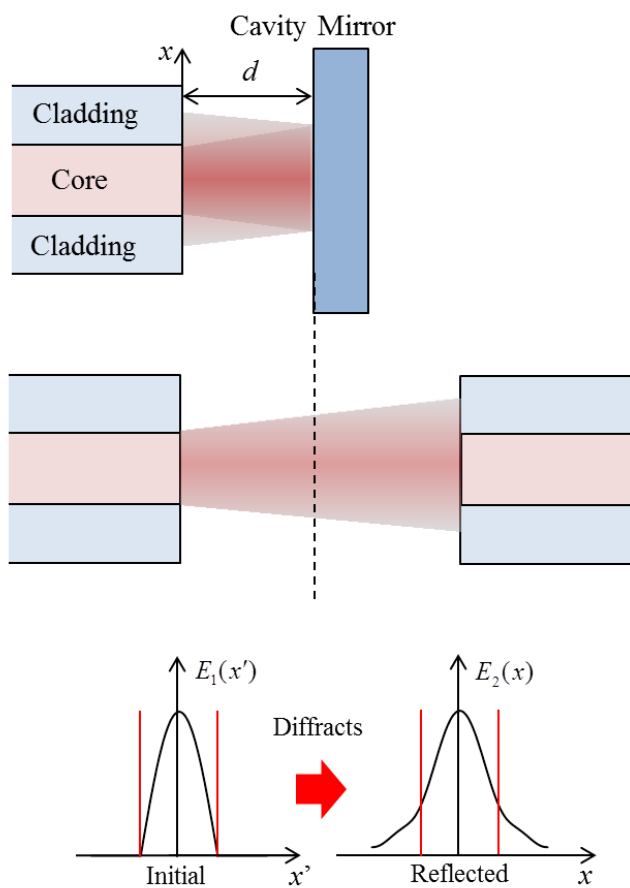


Figure 5-2. Schematic drawing of mode diffraction after leaving the waveguide facets.

$$\Gamma = \left| \frac{\left(\int_{\Sigma} U_1^*(x) U_0(x) dx \right)^2}{\left(\int_{\Sigma} U_1^*(x) U_1(x) dx \right) \left(\int_{\Sigma} U_0^*(x) U_0(x) dx \right)} \right|, \quad (5.7)$$

where $U_1(x)$ and $U_0(x)$ denote the diffracted mode profile after propagating $2d$ and original mode profile respectively. In practice, $(1-\Gamma)$ is plotted at different gap distance d in Fig. 5-3 for 220 μm and 400 μm IAG planar waveguide chip.

The general trend is that the coupling loss factor increases for both FM and 1st HOM as the gap distance increases while HOM suffers higher loss per bounce compared with

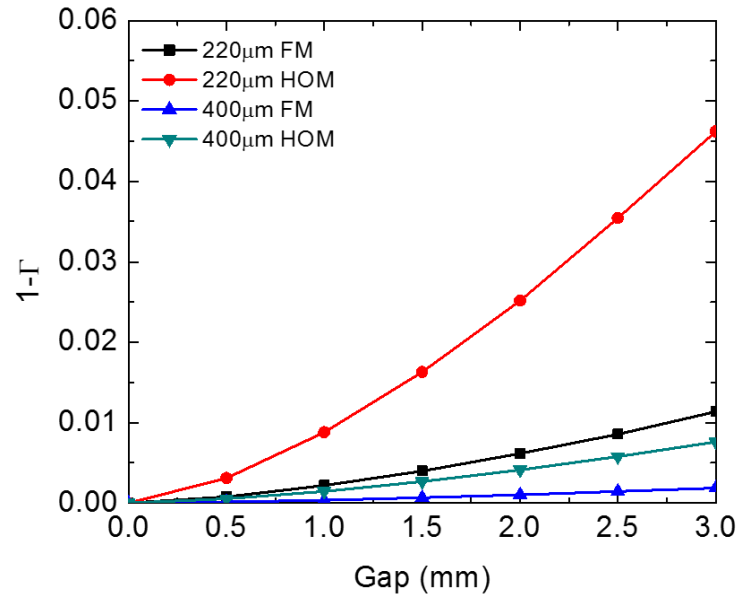


Figure 5-3. Calculated $(1-\Gamma)$ at different gap distance for IAG planar waveguide chips with core thickness of 220 μm and 400 μm .

FM. This modal associated loss, proved in latter chapters, can be used to facilitate modal discrimination.

5.2.3 Coupling loss in cylindrical IAG fiber lasers

The coupling loss exists in the IAG fiber lasers if the cavity is not formed by the

fiber ends and can be determined following the analysis above. The mode profile for FM and 1st HOM in IAG fiber with core radius a are given by [52]

$$U_{FM}(r) = \begin{cases} J_0(\tilde{u}r/a) & r \leq a \\ J_0(\tilde{u}) \frac{K_0(\tilde{w}r/a)}{K_0(\tilde{w})} & r \geq a \end{cases}, \quad (5.8)$$

$$U_{HOM}(r) = \begin{cases} J_1(\tilde{u}r/a) & r \leq a \\ J_1(\tilde{u}) \frac{K_1(\tilde{w}r/a)}{K_1(\tilde{w})} & r \geq a \end{cases}, \quad (5.9)$$

where J_n is Bessel function of the first kind and K_n is the modified Bessel function of the second kind; n denotes the order of the function; complex parameters \tilde{u} and \tilde{w} are closed related with the IAG fiber design pump power level [52]. According to ZFA, at large Δn , $\tilde{u}_{FM} \rightarrow j_{01} = 2.4048$ and $\tilde{u}_{HOM} \rightarrow j_{11} = 3.8317$. An important feature for modes in fibers

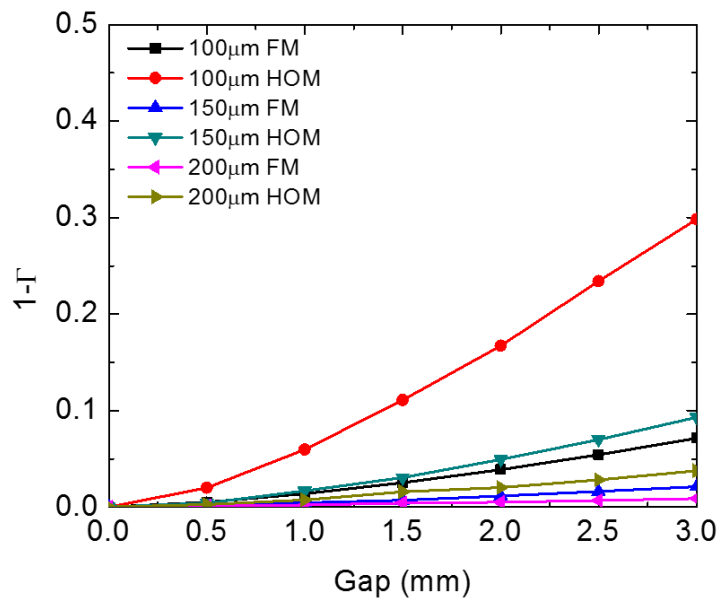


Figure 5-4. Calculated $(1 - \Gamma)$ at different gap distance for IAG fibers with 200 μm , 300 μm and 400 μm core diameter.

is that FM and 1st HOM are radially symmetric. Simulation is carried out in the same fashion as mentioned before. $(1 - \Gamma)$ is plotted at different gap distance d in Fig. 5-4 for IAG fibers with core diameter of 200 μm , 300 μm and 400 μm respectively.

5.3 Transverse mode competition

In this section, a general TMC model is firstly developed considering the transverse mode profiles. Then simulation and experiment results are shown based on IAG planar waveguide lasers while pure simulation results are shown based on IAG fiber lasers. Finally design and optimization insights are provided.

5.3.1 Theory

5.3.1.1 Rigrod analysis

The theoretical model dealing with intracavity intensity evolution inside is firstly proposed by Rigrod [115], which is the basis of the model developed in this section. To explain it, consider a plane-parallel laser resonator with a high reflector (HR) and an output coupler (OC) as illustrated in Fig. 5-5. The length of the gain media is L . The gap distance d between mirrors and crystal facets on both sides of the resonator are assumed to be the same. The forward propagation (from HR to OC) and the backward propagation (from OC to HR) intracavity lasing intensity at a given longitudinal position z are expressed as

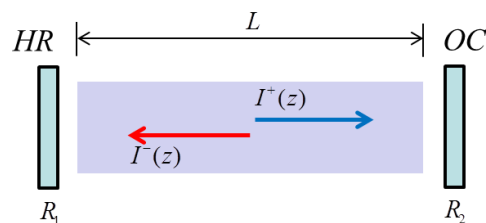


Figure 5-5. Schematic of the plane-parallel laser resonator.

$I^+(x, y, z)$ and $I^-(x, y, z)$ respectively.

In absence of interference between forward and backward lasing signal, the propagation equations for $I^+(x, y, z)$ and $I^-(x, y, z)$ inside the laser resonators with distributed loss coefficient α , saturation factor s and small signal gain g_0 are given as [100] :

$$\frac{dI^+(x, y, z)}{dz} = \frac{g_0 I^+(x, y, z)}{1 + s[I^+(x, y, z) + I^-(x, y, z)]} - \alpha I^+(x, y, z), \quad (5.10)$$

$$\frac{dI^-(x, y, z)}{dz} = -\frac{g_0 I^-(x, y, z)}{1 + s[I^+(x, y, z) + I^-(x, y, z)]} + \alpha I^-(x, y, z). \quad (5.11)$$

The normalized transverse intensity profile $f(x, y)$ is related with the intracavity power $P(z)$ through $P(z)f(x, y) = I(x, y, z)$ [87], where $\iint f(x, y) dx dy = 1$. To simplify, $f(x, y)$ is assumed to be constant along the z -axis. Integrate Eq. (5.10) and (5.11) over the transverse plane yields the intracavity power propagation equations:

$$\frac{dP^+(z)}{dz} = g_0 P^+(z) \iint \frac{f(x, y) dx dy}{1 + sf(x, y)[P^+(z) + P^-(z)]} - \alpha P^+(z), \quad (5.12)$$

$$\frac{dP^-(z)}{dz} = -g_0 P^-(z) \iint \frac{f(x, y) dx dy}{1 + sf(x, y)[P^+(z) + P^-(z)]} + \alpha P^-(z). \quad (5.13)$$

Eq. (5.12) and (5.13) form a coupled differential equation system (CDEs), the boundary conditions of which are listed as

$$P^+(0) = \Gamma R_1 P^-(0) = \tilde{R}_1 P^-(0), \quad (5.14)$$

$$P^-(L) = \Gamma R_2 P^+(L) = \tilde{R}_2 P^+(L), \quad (5.15)$$

where \tilde{R}_1 and \tilde{R}_2 are the effective reflectivity for HR and OC considering the coupling loss. The solution to the CDEs are known as first integral [87]:

$$P^+(z)P^-(z) = C, \quad (5.16)$$

where C is a spatially invariant constant. The output power is expressed as $P^+(L)(1 - \Gamma\tilde{R}_2)$. Eq. (5.12) to (5.16) define a boundary condition problem which describes the power evolution inside a given laser resonator, which is illustrated in Fig. 5-6.

Round-trip circulation starts from HR. $P^+(z)$ is amplified by the gain media while propagating forward. When bouncing back from the OC side, part of the energy is lost in term of the output while the rest coupled back into the cavity. Due to mode coupling, there is additional energy loss for intracavity intensity when coupling back into the waveguide core. The lasing signal is amplified by the gain media again while propagating backward.

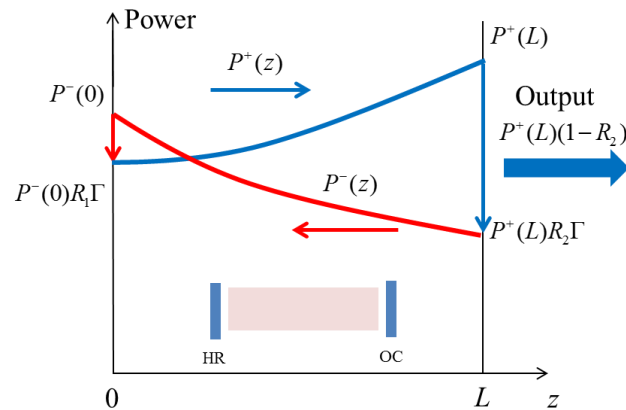


Figure 5-6. Schematic for power evolution inside a laser resonator.

At HR side, the other boundary condition has to be fulfilled. At steady state, the lasing signal needs to repeat itself after travelling one round-trip. This provides a way to solve the CDEs numerically, namely through searching for self-consistent solutions.

One of important application of this model is to calculate modal output lasing power at given pump power. Compared with the spatial rate equation discussed in chapter 4, a

major advantage of this model is that the intracavity lasing power is calculated at each longitudinal location, which provides more information about intracavity power evolution. In addition, it is valid for resonator configuration with low reflectivity OC since the gain saturation is considered at given longitudinal position. However, this is at the cost of increasing the complexity of calculation.

5.3.1.2 Gain saturation by dual transverse modes

To illustrate TMC, the gain is assumed to be uniform in given transverse plane (x - y plane). For practical interest, only FM and 1st HOM are considered. Each mode satisfies the CDEs and the boundary conditions discussed before individually. However, the gain media is shared with all propagating lasing signals. Therefore the sum of all the forward and backward intensities are used as the saturation terms. To show this mathematically, Eq. (5.10) and (5.11) transfers into:

$$\frac{dI_1^+(\bar{r})}{dz} = \frac{g_0 I_1^+(\bar{r})}{1 + s[I_1^+(\bar{r}) + I_1^-(\bar{r}) + I_2^+(\bar{r}) + I_2^-(\bar{r})]} - \alpha_1 I_1^+(\bar{r}), \quad (5.17)$$

$$\frac{dI_1^-(\bar{r})}{dz} = \frac{g_0 I_1^-(\bar{r})}{1 + s[I_1^+(\bar{r}) + I_1^-(\bar{r}) + I_2^+(\bar{r}) + I_2^-(\bar{r})]} + \alpha_1 I_1^-(\bar{r}), \quad (5.18)$$

$$\frac{dI_2^+(\bar{r})}{dz} = \frac{g_0 I_2^+(\bar{r})}{1 + s[I_1^+(\bar{r}) + I_1^-(\bar{r}) + I_2^+(\bar{r}) + I_2^-(\bar{r})]} - \alpha_2 I_2^+(\bar{r}), \quad (5.19)$$

$$\frac{dI_2^-(\bar{r})}{dz} = \frac{g_0 I_2^-(\bar{r})}{1 + s[I_1^+(\bar{r}) + I_1^-(\bar{r}) + I_2^+(\bar{r}) + I_2^-(\bar{r})]} + \alpha_2 I_2^-(\bar{r}), \quad (5.20)$$

where the subscript 1 and 2 correspond to the FM and 1st HOM respectively; \bar{r} denotes the spatial coordinate. The optical power inside waveguide core relates with the spatial invariant mode intensity profiles as $P_n(z)f_n(x, y) = I_n(\bar{r})$, $n = 1, 2$. Integrate Eq. (5.17) to Eq. (5.20) over the transverse plane yields:

$$\frac{dP_1^+}{dz} = g_0 P_1^+ \iint \frac{f_1(x, y) dx dy}{1 + sf_1(x, y)[P_1^+ + P_1^-] + sf_2(x, y)[P_2^+ + P_2^-]} - \alpha_1 P_1^+, \quad (5.21)$$

$$\frac{dP_1^+}{dz} = -g_0 P_1^+ \iint \frac{f_1(x, y) dx dy}{1 + sf_1(x, y)[P_1^+ + P_1^-] + sf_2(x, y)[P_2^+ + P_2^-]} + \alpha_1 P_1^+, \quad (5.22)$$

$$\frac{dP_2^+}{dz} = g_0 P_2^+ \iint \frac{f_2(x, y) dx dy}{1 + sf_1(x, y)[P_1^+ + P_1^-] + sf_2(x, y)[P_2^+ + P_2^-]} - \alpha_2 P_2^+, \quad (5.23)$$

$$\frac{dP_2^-}{dz} = -g_0 P_2^- \iint \frac{f_2(x, y) dx dy}{1 + sf_1(x, y)[P_1^+ + P_1^-] + sf_2(x, y)[P_2^+ + P_2^-]} + \alpha_2 P_2^-, \quad (5.24)$$

where P^- and P^+ are short for $P^-(z)$ and $P^+(z)$ respectively. Eq. (5.21) to (5.24) form the CDEs describing the power evolution for each mode inside the laser resonator. The denominators containing intracavity optical power for each mode indicate that the gain is saturated by both modes in two propagation directions. It has been shown in section 5.2.2 that Γ is modal dependent. Therefore, the boundary condition for each modes are given respectively as:

$$P_1^+(0) = \Gamma_1 R_1 P_1^-(0), \quad P_1^-(L) = \Gamma_1 R_2 P_1^+(L), \quad (5.25)$$

$$P_2^+(0) = \Gamma_2 R_1 P_2^-(0), \quad P_2^-(L) = \Gamma_2 R_2 P_2^+(L). \quad (5.26)$$

The solution for each mode is first integral which related with two individual constants:

$$P_1^-(z)P_1^+(z) = C_1, \quad (5.27)$$

$$P_2^-(z)P_2^+(z) = C_2. \quad (5.28)$$

For given g_0 , when steady state is reached, the intracavity power will reproduce itself after one round trip for both FM and 1st HOM simultaneously. This condition, in principle, can be used to numerical solve CDEs. However, dual mode case requires significant calculation power combined with increased code instability. This topic will be detailed in the following

sections.

The solution to the CDEs yields the modal output power for each mode. Besides, the normalized output intensity along the x -axis can be extracted as well by considering the power fraction of the total power as the weight. This provides a feasible approach to verify the model experimentally which will be discussed in detail in the following section.

5.3.1.3 Planar waveguide

Previously developed model is applied to IAG planar waveguide lasers. Instead of modal intracavity power, the power in the core per unit length P_c along the x -axis is considered. As shown in reference [116], $I(x, z) = P_c(z) f_c(x)$ where $f_c(x)$ is the normalized intensity profile along x -axis. In IAG planar waveguide lasers, $f_c(x)$ for FM and 1st HOM are given by Eq. (5.5) and (5.6) respectively.

The formulism can be further simplified by using averaged core intensity along the x -axis $I'(z)$ which is defined as $I'(z) = sP_c(z)/2a$. Eq. (5.21) to Eq. (5.24) are transformed into:

$$\frac{dI_1^+(z)}{dz} = g_0 \cdot S_1 \cdot I_1^+(z) - \alpha_1 \cdot I_1^+(z), \quad (5.29)$$

$$\frac{dI_1^-(z)}{dz} = -g_0 \cdot S_1 \cdot I_1^-(z) + \alpha_1 \cdot I_1^-(z), \quad (5.30)$$

$$\frac{dI_2^+(z)}{dz} = g_0 \cdot S_2 \cdot I_2^+(z) - \alpha_2 \cdot I_2^+(z), \quad (5.31)$$

$$\frac{dI_2^-(z)}{dz} = -g_0 \cdot S_2 \cdot I_2^-(z) + \alpha_2 \cdot I_2^-(z), \quad (5.32)$$

where S_n is the saturation factor for n -th mode, which are expressed as:

$$S_1 = \int_{-a}^a \frac{f_1(x)}{1 + 2a[I_1^{'+}(z) + I_1^{-}(z)]f_1(x) + 2a[I_2^{'+}(z) + I_2^{-}(z)]f_2(x)} dx, \quad (5.33)$$

$$S_2 = \int_{-a}^a \frac{f_2(x)}{1 + 2a[I_1^{'+}(z) + I_1^{-}(z)]f_1(x) + 2a[I_2^{'+}(z) + I_2^{-}(z)]f_2(x)} dx. \quad (5.34)$$

The first integrals for dual modes are converted into

$$I_1^{+}(z)I_1^{-}(z) = c_1, \quad (5.35)$$

$$I_2^{+}(z)I_2^{-}(z) = c_2. \quad (5.36)$$

Where c_1 and c_2 are individual constants. Further simplification can be done by eliminating the backward propagation terms in Eq. (5.33) and (5.34) using Eq. (5.35) and (5.36):

$$S_1 = \int_{-a}^a \frac{f_1(x)}{1 + 2a\left[I_1^{'+}(z) + \frac{c_1}{I_1^{'+}(z)}\right]f_1(x) + 2a\left[I_2^{'+}(z) + \frac{c_2}{I_2^{'+}(z)}\right]f_2(x)} dx, \quad (5.37)$$

$$S_2 = \int_{-a}^a \frac{f_2(x)}{1 + 2a\left[I_1^{'+}(z) + \frac{c_1}{I_1^{'+}(z)}\right]f_1(x) + 2a\left[I_2^{'+}(z) + \frac{c_2}{I_2^{'+}(z)}\right]f_2(x)} dx. \quad (5.38)$$

The boundary conditions for both modes are related with c_1 and c_2 through:

$$c_1 = \frac{1}{\Gamma_1 R_1} [I_1^{+}(0)]^2 = \Gamma_1 R_2 [I_1^{+}(L)]^2, \quad (5.39)$$

$$c_2 = \frac{1}{\Gamma_2 R_1} [I_2^{+}(0)]^2 = \Gamma_2 R_2 [I_2^{+}(L)]^2. \quad (5.40)$$

The output power intensity is given as $I_n^o = I_n^{'+}(L)(1 - R_2)$, $n = 1, 2$. Eq. (5.29) to (5.40) form specifically the CDEs for IAG planar waveguide lasers with a well-defined boundary

conditions.

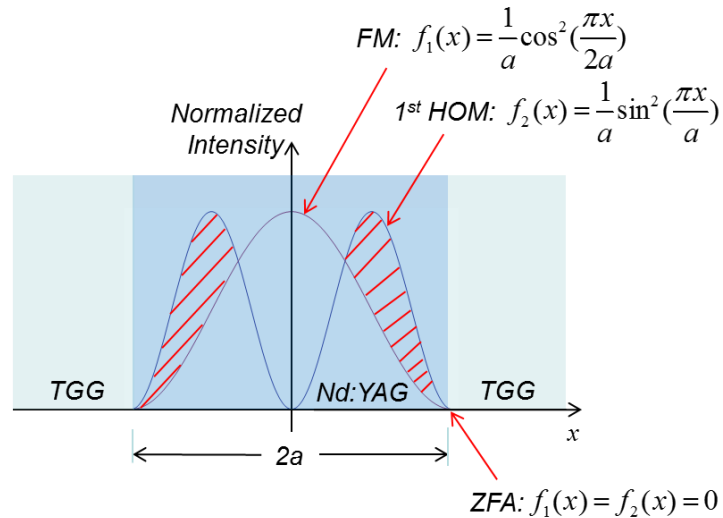


Figure 5-7. Transverse mode overlap with gain media for FM and 1st HOM.

The physical interpretation of S_1 and S_2 are illustrated in Fig. 5-7. The integrals in Eq. (5.37) and (5.38) represent the modal gain of FM and 1st HOM respectively. Assume only FM reaches lasing threshold. In presence of the lasing power of FM, S_1 and S_2 are reduced simultaneously. This makes 1st HOM even more difficult to reach its own lasing threshold. In this way, 1st HOM is suppressed. However, due to the intensity shape of 1st HOM, it can access to the peripheral gain region near the material interface, which is represented by the numerator in S_2 . This geometrical advantage favors 1st HOM. The actual threshold of 1st HOM is consequence of the balance between these two processes, which are closely related with waveguide design and resonator configuration.

5.3.1.4 Solve the CDEs

The CDEs described in section 5.3.1.4 is solved numerically by searching for c_1

and c_2 simultaneously. An algorithm based on the combination of 4th order Runge–Kutta method (ordinary differential equation solver) and Newton-Raphson method (roots searching) is developed. The schematic diagram is shown in Fig. 5-8.

Before solving the CDEs, parameters based on the IAG planar waveguide laser design need to be collected. These parameters are divided into 2 categories: resonator configuration and waveguide design, which are given in table 5-1.

Table 5-1. Parameters used before solving the CDEs.

Resonator Configuration	Waveguide Design
Reflectivities R_1 , R_2	Core thickness $2a$
Cavity length L	Core refractive index n_1
Mirror-Crystal gap d	Refractive index step Δn
Small signal gain g_0	Lasing wavelength λ

A set of initial guess value of c_1 and c_2 is proposed. Both initial values $I_1^+(0)$, $I_2^+(0)$ and boundary values $I_1^+(L)$, $I_2^+(L)$ are then calculated according to Eq. (5.39) and (5.40). $I_1^+(0)$, $I_2^+(0)$ are passed to the 4th order Runge-Kutta solver, together with other waveguide laser parameters to generate the new boundary values $I_1^+(L)$, $I_2^+(L)$. Another pair of c_1 and c_2 based on newly generated $I_1^+(L)$, $I_2^+(L)$ are then calculated. The absolute difference of $I_1^+(L)$, $I_2^+(L)$ between two iterations are calculated and compared with the preset tolerance. $I_1^+(L)$, $I_2^+(L)$ are accepted as the solutions to the

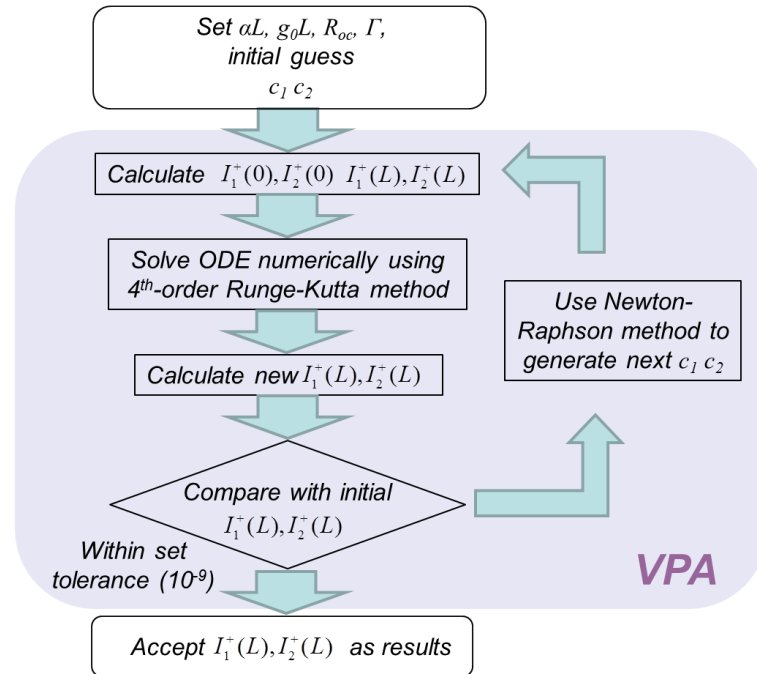


Figure 5-8. Schematic diagram of strategy for solving coupled ODEs. In order to increase the accuracy, variable precision algorithm (VPA) is used.

CDEs if the absolute difference is smaller than the tolerance. Otherwise, the newly generated set of c_1 and c_2 are used to predict the next possible set of c_1 and c_2 using Newton-Raphson method. By setting the prediction as the initial guess, a loop is formed in order to find the self-consistent solution of c_1 and c_2 . The variable precision algorithm, or VPA, is used in the numerical calculation in order to increase accuracy. The algorithm is implemented using MATLAB. Original MATLAB code are attainable by contacting the author.

It is worth noting that though Newton-Raphson method leads to a convergent solution most of the time, for some particular combination of parameters convergent solution is not available. This is often the case when $I_2^+(L)$ approaches to zero. According to Eq. (5.37) and (5.38), the denominators approaches to infinity and the root searching is

around the boundary of convergent region. Small perturbation around this region results in divergence. A practical solution to this is to search the root manually around the region of interest. A graphic user interface (GUI) in MATLAB is used to facilitate root searching for certain parameter combination.

5.3.2 TMC simulation and experiment results

Experiment efforts have been spent on exploring TMC inside IAG planar waveguide lasers. Due to the limited chip designs, two IAG chips are used experimentally, the core size of which are 220 μm and 400 μm respectively. The experiment setups and mode analysis methods have been detailed in chapter 2 in detail.

5.3.2.1 220 μm chip

The laser cavity configuration as well as chip design parameters are given in table 5-2 for 220 μm chip. Due to the spacing issue, the gaps on both sides are 2.7 mm. According to chapter 3, the α_1 is calculated to be $8.215 \times 10^{-4} \text{ cm}^{-1}$ while α_2 is calculated to be $3.286 \times 10^{-3} \text{ cm}^{-1}$. The near-field mode profile at lasing threshold and maximal output power are shown in Fig. 5-9. The fitting indicates that along the x -axis the lasing remains pure

Table 5-2. Parameters used in the 220 μm chip experiment.

Parameter	Value	Parameter	Value
n_1	1.82	L	1.98 cm
Δn	0.134	d_1	2.7 mm
λ	1.06 μm	d_2	2.7 mm
R_1	1	R_2	0.9

FM operation as discussed in chapter 3. The measured output power at given pump power

and the simulation results with different single pass gain are given in Fig. 5-10.

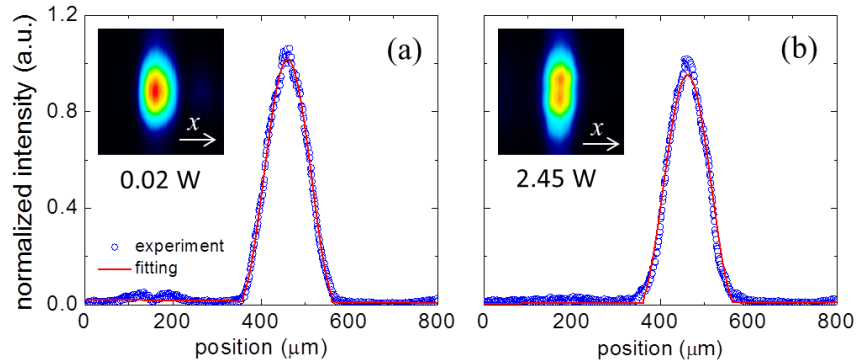


Figure 5-9. The near-field mode pictures and intensity profiles along the x -axis at the mode centroid for (a) 0.02W lasing power and (b) 2.45W lasing power [98]. Horizontal arrow in the inset indicates the bounded direction. The red lines represent the cosine square fitting [98].

As the increase of g_0L , the simulation result shows the IAG planar waveguide lasers can be operated in 3 regions. Region I is between zero the threshold of FM. In this

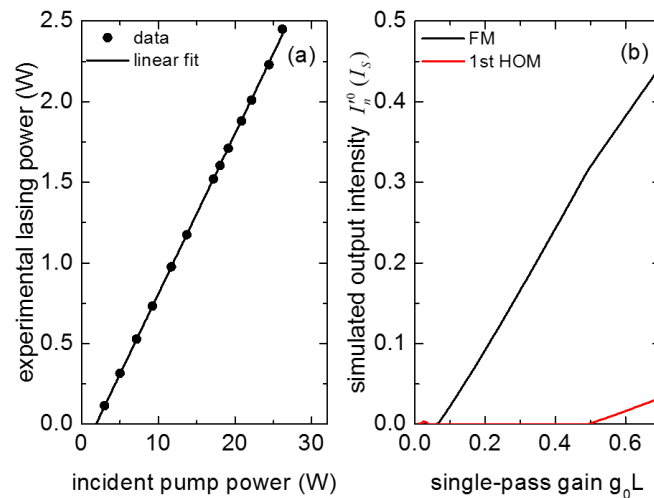


Figure 5-10. Measured and simulated output for 220 μm chip with $R_{oc} = 0.9$: (a) the measured output lasing power at given pump power and (b) simulated output intensity for FM and 1st HOM at given single-pass gain g_0L [98].

region no lasing signal since g_0L is smaller than the threshold of FM. Region II is between the lasing threshold of FM and 1st HOM. In this region, only FM oscillates and the output intensity increases linearly with g_0L while the FM remains below lasing threshold. It is worth noting that it is possible that the gain is larger than the propagation threshold of 1st HOM. However, the quench of 1st HOM oscillation is due to the gain saturation process. The third region is after the threshold of 1st HOM. FM and 1st HOM appear in the cavity and output.

The important parameters extracted from the simulation is the pump threshold of FM $(g_0L)_{FM}$ and 1st HOM $(g_0L)_{HOM}$. This is extracted from the simulation results by fitting output of FM in region II and calculating the intersection. According to figure 8(b), $(g_0L)_{FM}$ is calculated to be 0.05989 and $(g_0L)_{HOM}$ is calculated to be 0.50485. The simulated threshold contract defined as $\xi_{theo} = (g_0L)_{HOM} / (g_0L)_{FM}$ is determined to be 8.4 ± 0.7 . The plus and minus sign arises from the fitting uncertainty. In experiment, since 1st HOM did not appear in the near-field mode. The experiment results yield the threshold contract ξ_{exp} to be larger than 14 ± 2 . The obvious deviation suggests that the mode discrimination is larger in experiment than in simulation. This is reasonable since only mode profile along the x -axis is considered in this model. As shown in chapter 3, the mode along the y -axis is guided by thermal refractive focusing and gain guiding, which has modal associated loss. This loss also contributes to the overall lasing performance further delaying the onsite of the 1st HOM.

To conclude the 220 μm case, the theoretical calculation agrees with the experiment observation. Since HOM has not been observed, robust fundamental mode operation with up to pump power limited 14 times higher than lasing threshold is achieved.

5.3.2.2 400 μm chip

The parameters used in 400 μm chip experiments are listed in table 5-3. For 400 μm chip, α_1 is calculated to be $2.14 \times 10^{-4} \text{ cm}^{-1}$ while α_2 is calculated to be $8.57 \times 10^{-4} \text{ cm}^{-1}$.

Table 5-3. Parameters used in the 400 μm chip experiment.

Parameter	Value	Parameter	Value
n_1	1.82	L	1.54 cm
Δn	0.134	d_1	1.75 mm
λ	1.06 μm	d_2	1.75 mm
R_1	1	R_2	0.9, 0.7

Based on the parameters in table 5-3, the simulated output intensity of FM and 1st HOM

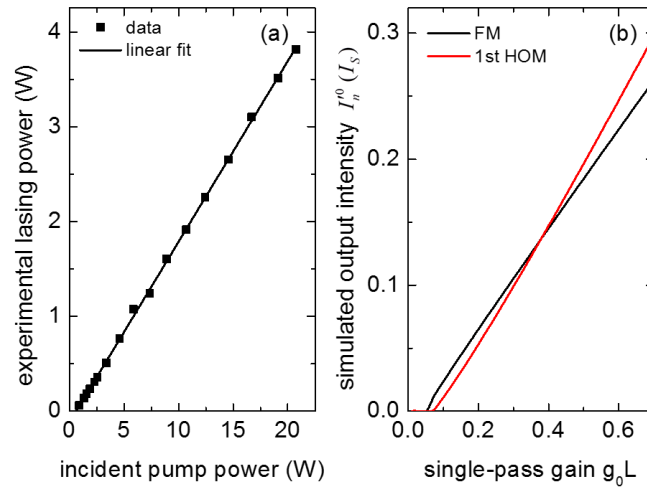


Figure 5-11. Measured and simulated output for 400 μm chip with $R_{oc} = 0.9$: (a) the measured output lasing power at given pump power and (b) simulated output intensity for FM and 1st HOM at given single-pass gain g_0L [98].

are plotted with g_0L as well as measured output power at different incident pump power in Fig. 5-11. The simulated results [98], shown in Fig. 5-11 (b), are different for 220 μm case since the span of region II is much smaller. $(g_0L)_{FM}$ is calculated to be 0.05499 and $(g_0L)_{HOM}$ is calculated to be 0.07026. ξ_{thero} is 1.3 ± 0.1 . The calculation suggests that 1st HOM oscillates quickly after FM reaches the lasing threshold. This is verified by the near-field mode profiles in Fig. 5-12.

Unlike the 220 μm case, the near-field mode quickly deviates from the FM shape along the x -axis with a noticeable intensity dip in the center region when pump power is increased. Pure FM is only observed around lasing threshold, which agrees with the trend predicted by the model. The intensity does not drop to zero at the centroid suggesting the output mode is the combination of FM and 1st HOM. To quantify it, the intensity profile along the x -axis across the geometric centroid is extracted out from the near-field images which is then fitted with:

$$I(x) = A \cos^2[\pi(x - x_c) / 2a] + B \sin^2[\pi(x - x_c) / a], \quad (5.41)$$

where x_c , A and B are the fitting parameters. A and B represent the relative weight of FM and 1st HOM in the output respectively. The modal ratio defined as A/B is then extracted at given total lasing power. According to the model, A and B are proportional to $I_1'^o$ and $I_2'^o$ respectively. Therefore, the modal ratio can also be written as $I_1'^o / I_2'^o$, representing the degree of modal mixing. It can be determined experimentally based on A and B as mentioned before whereas it can also be determined through simulation using $I_1'^o / I_2'^o$.

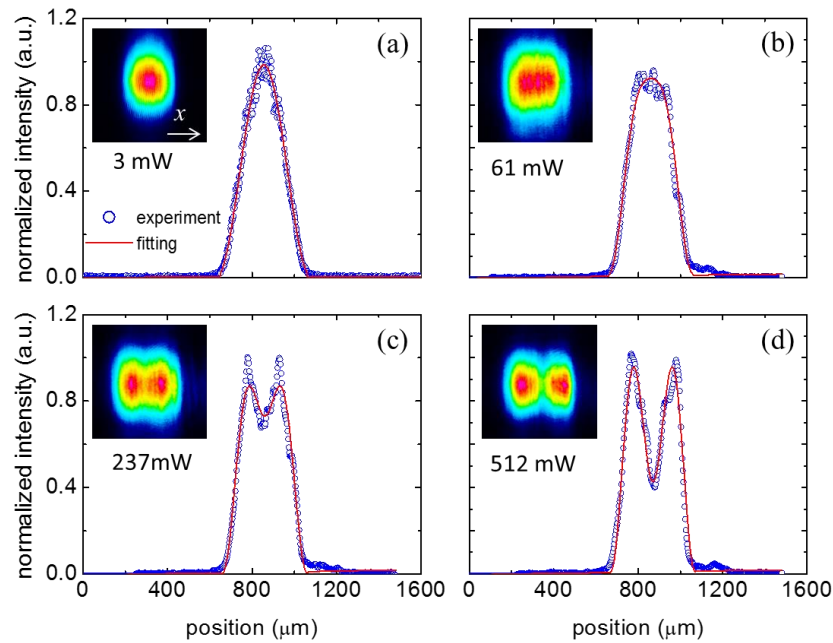


Figure 5-12. The near-field mode pictures and intensity profiles along the x -axis at the mode centroid for lasing power at (a) 0.002W, (b) 0.064W, (c) 0.237W and (d) 0.512W. Horizontal arrow in the insets indicates the bounded direction. The red lines represent the cosine square fitting [98].

To further exam the model, modal ratio is calculated based on experiment results as well as simulation at given output power as shown in Fig. 5-13. As shown, the experiment results follow the simulated trends. Pure FM yields the infinity modal ratio happened only around the lasing threshold. 1st HOM begins to gain its presence in the lasing resonator reflected by the decrease of the modal ratio. The ratio is expected to approach zero at the large enough lasing power since HOMs are expected to dominate the output.

However, it is possible to suppress HOMs by increasing the modal discrimination loss. An easy approach is to increase the mirror gap introducing coupling loss. This

approach is proved to be effective maintaining FM operation in index guiding planar waveguide lasers [18]. Experimentally, the near-field mode profile for an extreme case with maximal incident pump is shown in Fig. 5-14. In this case, the OC side gap is 16 mm while the HR side gap is maintained. The near-field mode shows reasonable good fitting with cosine square shape along the x -axis, indicating FM operation. The output power in this case is, however, reduced to 2.64W.

During the experiment with 400 μm chip, the lasing power is kept at the low side of its span in the effort to avoid the onset of even higher order modes as well as to minimize

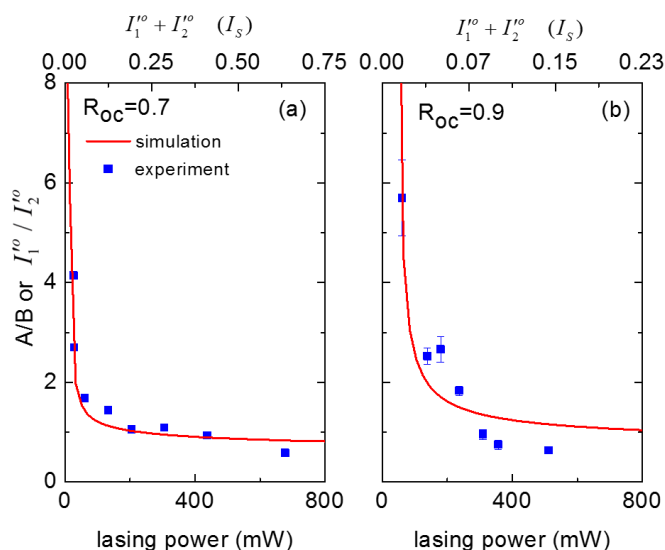


Figure 5-13. Modal ratio versus output for (a) $R_{oc} = 0.7$ and (b) $R_{oc} = 0.9$. The error bar represents one standard deviation from 10 measurements. The position represents the effort for best matching [98].

thermal refractive focusing. Strong thermal refractive focusing is founded with large incident pump power in 400 μm chip. The back reflection spot of the alignment He-Ne laser changed its position when the pump diode is turned off. It suggests the refractive index of the waveguide core is changed due to quantum heating. The detail discussion of

the TMC with thermal refractive focusing is beyond the scope of this dissertation. The near-field mode becomes unstable with $R_{oc} = 0.5$ and $R_{oc} = 0.3$ output coupler especially around the lasing threshold. For this reason, the data is not included here.

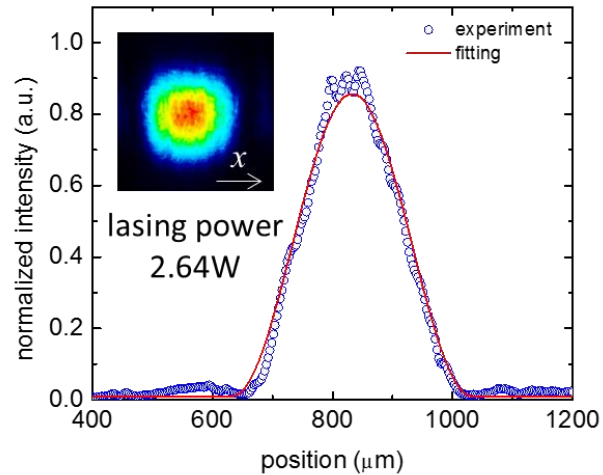


Figure 5-14. Near-field mode profile along the x -axis (blue circle) with cosine square fitting (red line) with 16mm gap in OC side and 1.6mm gap in HR side. The inset is the mode picture. The output power is 2.64W with maximal incident pump power.

Based on the results discussed above, several conclusions can be made: Firstly, according to the simulation, 400 μm chip behaves differently compared with its 220 μm counterpart regarding about the mode discrimination. Pure FM operation only lasts for a small region of incident pump power. This agrees with experiment observation. Secondly, above the threshold of 1st HOM, they exist simultaneously. The modal ratio affirms the trend predicted by the TMC model, which shows intensity or power weight of 1st HOM grows as pump power increases.

5.4 Performance optimization

Based on the TMC model introduced above, effects of design parameters on the

output modal components of given IAG planar waveguide lasers are discussed in this section. The discussion is concentrated on the IAG structure itself in both planar waveguide and fiber geometry. Therefore, only distributed loss is considered. The laser resonator is fixed to be a plane-parallel cavity with a high reflector and an output coupler with a uniform gain cross section. The mirror-facet gap is negligible. The performance matrix is firstly introduced followed by simulation results. The physical interpretation is illustrated. Finally, a general strategy for IAG laser output performance optimization are developed in the section.

5.4.1 Performance matrix

Design parameters associated with IAG laser can be divided into two categories: waveguide design and resonator configuration which are listed in table 5-1. The former directly contributes to the modal distributed loss coefficients while the latter controls the output power. After solving the CDEs, typical simulation result is given in Fig. 5-15. As discussed in section 5.3.2, the IAG laser operation is divided into 3 regions according to g_0L . For practical considerations, the IAG laser is desired to operate in Region II where only FM is lasing since the output beam quality will degrade in Region III [107].

To quantitatively express IAG lasers performance in region II for a given IAG design, three parameters are used: threshold gain ratio (TGR), maximal single mode lasing intensity I_{\max} and maximal FM extraction efficiency η_{extr} . TGR is defined as $(g_0L)_{HOM} / (g_0L)_{FM}$, which denotes the span of the incident pump within which TMC guarantees only FM operation. Since $(g_0L)_{FM}$ can be calculated according to threshold condition, TGR be used to determine $(g_0L)_{HOM}$. A large TGR is in favor of robust FM operation with proper gain. I_{\max} is defined as the output intensity of FM at $(g_0L)_{HOM}$

which represents the output capability of FM operation. η_{extr} is defined as $I_{max} / (g_0L)_{HOM}$, which stands for the efficiency performance. These three parameters form a complete mathematical expression for the FM output within Region II. Any simulated output intensity of FM in this region can be extracted out as long as g_0L is given. In addition, η_{extr} is often used in practice due to its simplicity compared with other efficiency parameters, and it is also referred as optical efficiency.

5.4.2 Performance simulation

TGR, I_{max} and η_{extr} are calculated according to the solution to the CDEs in both fiber and waveguide geometry. To represent the resonator configuration and waveguide design, a 2-D grid formed by R_{oc} and FM loss factor α_1L which serves as the input. The loss factors of the 1st HOM can be directly calculated according to section 3.2. The results are given in Fig 5-16 for 1-D planar waveguides and Fig.5-17 for fiber.

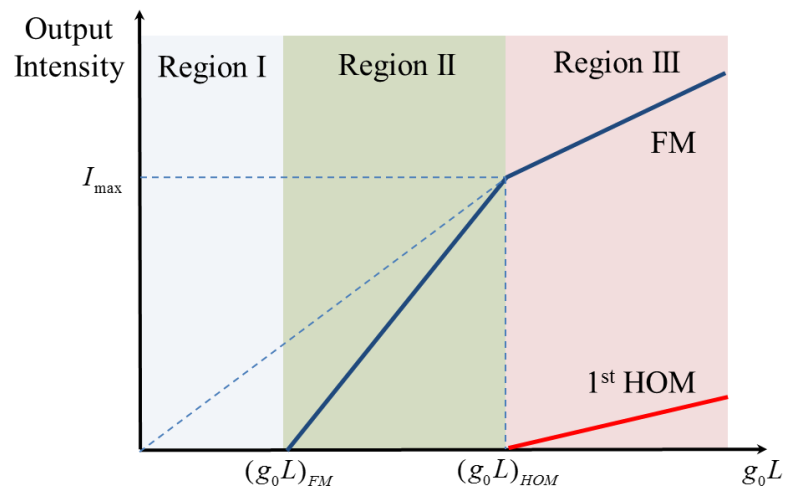


Figure 5-15. Typical simulation results by solving the CDEs.

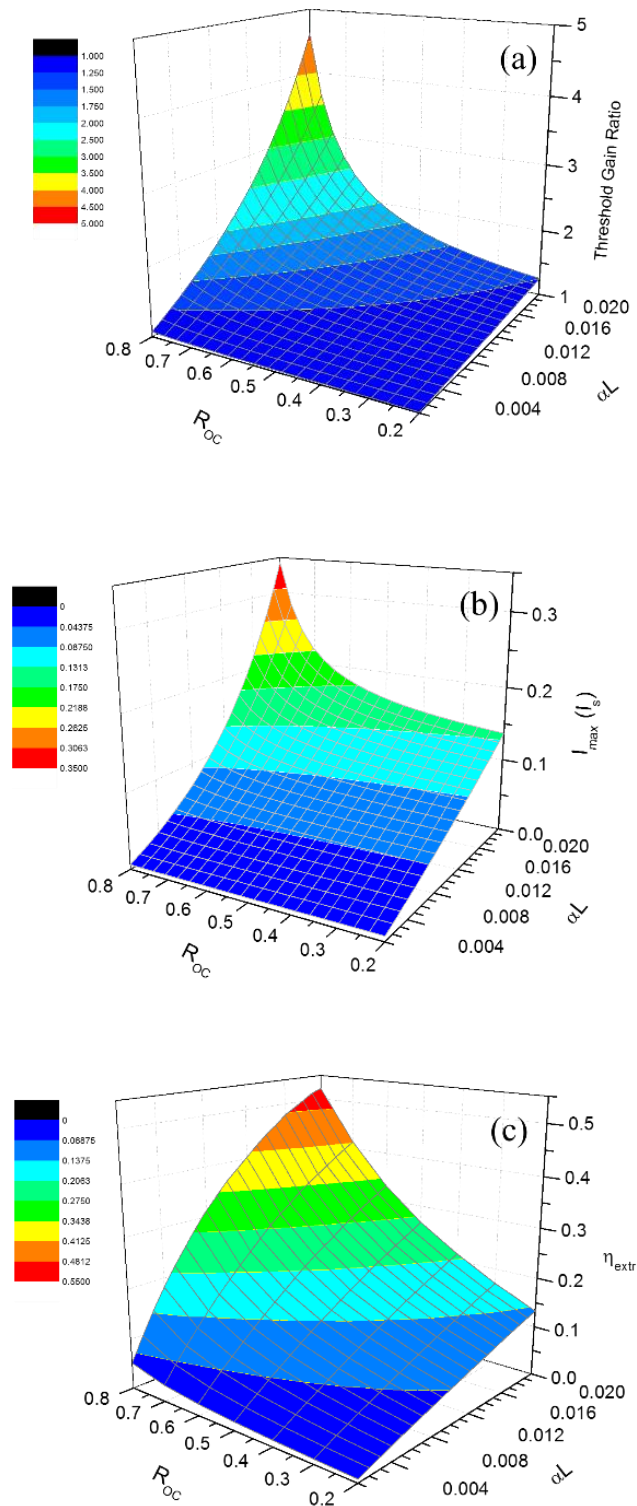


Figure 5-16. Simulation results for (a) TGR, (b) I_{max} and (c) η_{extr} in 1-D planar waveguide.

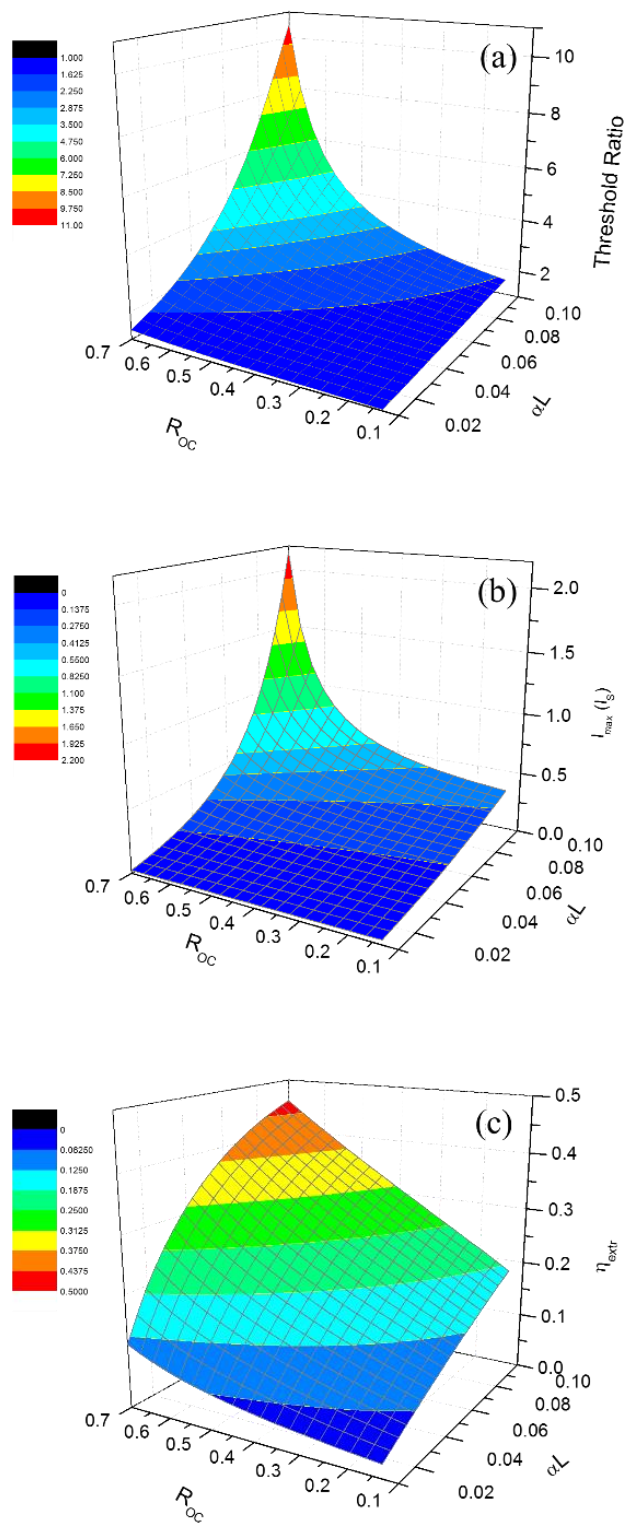


Figure 5-17. Simulation results for (a) TGR, (b) I_{max} and (c) η_{extr} in fiber.

Despite the exact shape, the general trends clearly show that a large αL and R_{oc} helps to improve TGR, I_{\max} and η_{extr} at the same time in both 1-D planar waveguide and fiber. The contribution of the resonator configuration is illustrated qualitatively, for example in uniformly 1-D planar waveguide lasers.

Consider the laser is operated in region II with spatially unsaturated gain profile shown in Fig. 5-18. In this region, the available gain for 1st HOM is presented qualitatively by the overlap area between its intensity profile (black curve) and the unsaturated gain media profile (color curves).

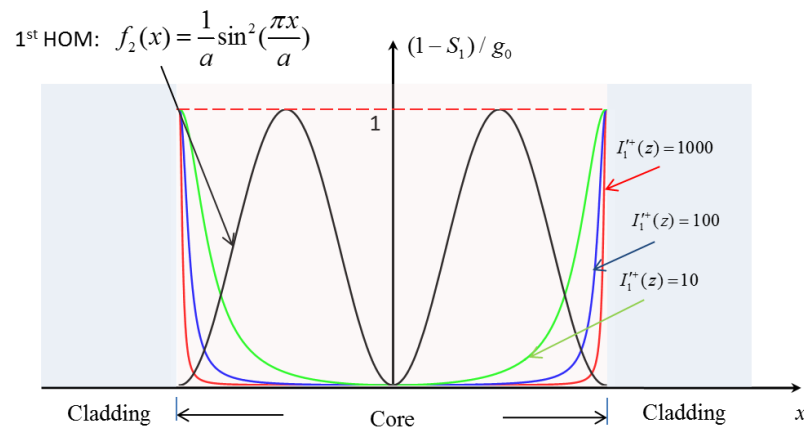


Figure 5-18. Residual spatial gain profile for 1st HOM in region II for 1-D IAG planar waveguide. The vertical axis represents the normalized unsaturated gain factor (NUGF). The black curve is the normalized intensity profile of 1st HOM. The green, blue and red curves stand for the spatial profile of NUGF with $I_1^+(z)$ to be 10, 100 and 1000.

The increase of $I_1^+(z)$ due to larger R_{oc} results in the shrink of the overlap area, especially near the core-cladding boundary. This process makes 1st HOM difficult to overcome the round-trip loss (output coupling and distributed loss) for oscillation. Consequently, TGR, I_{\max} and η_{extr} increases. Simulation shows it is possible at the region where $R_{oc} > 0.8$ and

$\alpha_1 L > 0.1$ that $(g_0 L)_{HOM}$ becomes impractically large. In this region, robust FM operation is guaranteed due to TMC. The design parameters (i.e. refractive index contrast, waveguide core thickness and physical length of the waveguide) affect the performance of IAG waveguide lasers through $\alpha_1 L$, the influence of which on TGR, I_{\max} and η_{extr} are, however, more direct. It is shown that $\alpha_2 L$ is proportional to $\alpha_1 L$. Larger $\alpha_1 L$ requires larger $g_0 L$ to reach the threshold of lossless propagation of the 1st HOM, letting alone achieving resonance.

In practice, there are other constrains to be satisfied, for instance, the availability of the pump power and the material damage threshold. When calculating TGR, I_{\max} and η_{extr} , $g_0 L$ therefore the incident pump power is assumed to be sufficient to reach $(g_0 L)_{HOM}$. If $g_0 L$ provided by the maximal available pump power is still smaller than $(g_0 L)_{HOM}$, the robust FM operation for this IAG laser is secured. The performance can be improved by selecting a proper output coupler. If $g_0 L$ provided by the maximal available pump power is larger than $(g_0 L)_{HOM}$, the output coupler with larger reflectivity is needed to rise TGR, therefore to rise $(g_0 L)_{HOM}$. In this case, the intracavity power needs more attention due to the material damage threshold. For instance, commonly used gain media for fiber laser is Nd doped phosphate glass, which has a transition temperature around 450 degree centigrade [117]. Deposited heat due to incident pump needs to be removed properly to avoid thermal failure. However, it has been reported in IAG fiber lasers that thermal damage is founded in both end pumping and side pumping schemes [53, 56, 57] even with proper thermal management. Another interesting region is where both $R_{oc} > 0.8$ and $\alpha_1 L > 0.1$ hold. The simulation shows in this region TMC is strong enough to suppress 1st

HOM. However, the resultant high intracavity intensity posts threats of thermal distortion and even thermal failure in reality. It is up to the practical case that decides which parameters is the suitable.

Based on the analysis above, the general strategy for IAG waveguide laser output performance optimization is briefly summarized as follows: Firstly, calculate TGR, I_{\max} and η_{extr} according to given IAG waveguide laser. Secondly, convert maximal available pump power to g_0L . This could be accomplished according to the model developed in chapter 4. Compare this g_0L with $(g_0L)_{HOM}$. If smaller, it means it is safe to operate at robust FM with the maximal pump power. Otherwise, change the output coupler to with larger reflectivity if possible. It is important to address that every laser system is unique, and there is no exact rule which can apply to every system without any modification. The strategy developed here only serves as guideline.

5.5 Summary

In summary, a 1-D theoretical model on TMC is proposed considering both distributed loss and coupling loss. In the model, bidirectional propagation intracavity intensity for both FM and 1st HOM are considered for gain saturation. Experiment results in planar waveguide geometry show reasonable good agreement with theoretical calculation. The results suggests robust FM operation can be achieved with the assist of both distributed loss and coupling loss. To isolate the contribution of the distributed loss to TMC, performance matrix of the IAG lasers is proposed. The influence of the waveguide design parameters and cavity configurations on TGR, I_{\max} and η_{extr} are calculated by solving the CDEs. The simulation indicates that robust FM operation can be secured with large R_{oc} and αL . However, in reality, factors such as maximal available gain and thermal

effects may impose other limitations on the performance of IAG lasers.

The model proposed in section 5.3.1 can be applied to other laser system as long as the all critical profiles and loss mechanism are known. Since the model only considers one dimension, where the gain is assumed to be uniform as discussed in chapter 4, the influence of the pump profile on TMC is not discussed in this dissertation. A comprehensive TMC model including the output power calculation can also be developed by properly integrating SRE model (discussed in chapter 4) and TMC model in. It is noted that, however, experiment support (such as near-field profiles at given pump power) are needed to carry out the simulation.

The near-field and far-field mode profiles is used to determine the FM operation in this chapter. This approach is widely used in photonic crystal fiber lasers [46]. Based on near-field imaging results, the modal ratio is used to determine the power percentage of FM and 1st HOM. It is verified by the experimental observations. However, it is worth noting that this method is valid only in region III where distinct near-field profiles helps to determine the mode ratio via fitting. As the 1st HOM component reduces in output near-field mode profiles, the fitting yields large uncertainty. The remaining challenge is to find a robust modal analysis approach can be used in region III, which helps to determine the onset of the 1st HOM. It was reported by many researchers in the integrated photonics society that the presence of 1st HOM in the waveguide is the consequence of the sudden drop of the fiber coupled output power [108, 118, 119]. In literatures, it was referred as “the power kink” [108, 120, 121]. However, after experiment trials, the power kink in IAG lasers is not as obvious as it is in ridged semiconductor waveguide lasers.

CHAPTER 6 CONCLUSION AND FUTURE WORK

6.1 Conclusion

The single-mode operation of IAG planar waveguide lasers with 220 μm -thick core is demonstrated. A theoretical model describing the guiding mechanism inside the face-pumped IAG planar waveguide laser is developed where the quadratic gain, thermal refractive focusing and index antiguiding present simultaneously. The simulation based on this theory agrees with experiment results, indicating that the lasing mode along the bounded direction is guided by the index antiguiding with negligible thermal refractive focusing while the mode along the bounded direction is guided by the thermal refractive focusing with negligible gain refractive focusing. It is also suggested that the level of involvement of thermal refractive focusing is largely determined by the incident pump and plays a crucial role in guiding modes along both bounded and unbounded directions

From the power efficiency perspective, experiment shows a maximal 2.4 W output power with 10% slope efficiency is demonstrated in CW operation. This is, as far as we know, the highest slope efficiency ever achieved in IAG lasers operated in CW mode while maintaining fundamental mode operation. A model based on spatial rate equation is developed, the simulation results of which show excellent agreement with experiment observation. The capability of fundamental mode operation in IAG planar waveguide lasers are also analyzed in both 220 μm and 400 μm IAG chips. A 1-D theoretical model based on Rigrod analysis is developed. The experiment results from two IAG chips shows reasonable agreement with simulation results. Based on this model, the performance matrix for single mode operation inside IAG planar waveguide and fiber are calculated. The results indicate that increasing distributed loss and reflectivity of output coupler help to

increase threshold gain ratio, optical efficiency and maximal single mode output intensity.

Based on the research in this dissertation, index-antiguidded proves itself as a feasible design scaling up the core size while maintaining the single fundamental mode operation. It is also worth noting this single fundamental mode CW operation requires carefully planning of both resonator configuration and waveguide design.

6.2 Future work

The possible future work focuses on 3 major topics: pulsing IAG planar waveguide lasers, developing robust modal analysis method and searching for possible pumping and cavity configuration to increasing the power efficiency.

The research in this dissertation focuses on the continuous wave operation of IAG waveguide lasers. It is also attractive to operate IAG planar waveguide lasers in pulsed mode. Reduced intracavity intensity due to large-mode-area capability of IAG structure is expected to facilitate further increase of peak intensity for either Q switched or mode-locked waveguide lasers. Passive pulsing can be achieved by inserting the actively controlled modulator or passive saturable absorber (SA). To reduce the size of the system, the latter one is favorable for IAG planar waveguide lasers. The SA can be inserted in two ways. The first one is to focus the intracavity lasing intensity onto the SA while the second one is to attach the SA parallel to the lasing direction. The high intensity field on the focusing spot is the most direct realization of nonlinear absorption of the SA, the process by which the passive Q-switching or model-locking are started. However the involvement of focusing and collimation inside the laser cavity introduce additional loss leading to the decrease of efficiency. In addition, the large core size of IAG planar waveguide lasers further reduces the intracavity intensity, making it even more difficult to increase the

intracavity intensity. The second approach, however, relies on the interaction between the SA and the evanescent field penetrating into the cladding[122]. It has been reported that both passive Q-switching [123-125] and passive mode-locking[126, 127] were achieved in this way with index guiding fiber and planar waveguide lasers. The evanescent interaction is suitable for pulsing IAG planar waveguide lasers in particular for the following reasons. Firstly, it has been shown that the intensity penetrating inside the cladding region is larger than its index guiding counterpart [128]. It enables the SA being placed far away from the waveguide core, making it flexible to fabricate proper waveguides. For the material choice, graphene is widely used due to its broadband nonlinear absorption and fast action time[129, 130]. A group of 2-D material, for example transition-metal dichalcogenides, (i.e. MoS₂, WS₂, and MoSe₂) is of great interests serving as SA due to the similar atomic structure as graphene[131, 132]. It is promising that the passive Q-switched or mode-locked of IAG planar waveguide lasers are possible in the form of evanescent field interaction with transition-metal dichalcogenides.

Besides all the discoveries in this dissertation, there are also remaining challenges on the precisely determination of the percentage of higher-order modes in the near-field imaging. Throughout this dissertation, as did in other large-mode-area waveguide lasers literatures, the near-field imaging is used as the primary method to verify fundamental mode operation. It is, however, noticed that this method is reliable for two regions: only single fundamental mode operation and obviously two modes operation. The transition period between these two regions are of great interest in determination of 1st HOM threshold, however not reliably resolved with this method. More robust method for modal component analysis is needed. For example, it was reported in the ridged waveguide lasers

literatures that there would be a sudden change of slope efficiency when 1st HOM reached the oscillation threshold. The “power kink” is the result of the reduction of the coupling efficiency into the output fiber due to the peak-shift of near field mode[133]. The same experiment with the IAG planar waveguide lasers has been done. The output from the 400 μm thick planar waveguide lasers are coupled into a single mode fiber in the effort to filtering the possible higher-order modes. The output from the fiber is measured by the power meter. The experiment does not show clear features as reported in ridged waveguide case, indicating other methods are needed.

Another possible further work is to end pump the IAG planar waveguide aiming to achieve higher efficiency since the pump power absorption per pass is higher than face pumping. In practice, high transmission pump beam shaping is needed as well as close loop control of diode laser temperature.

REFERENCE

- [1] T. Y. Fan and R. L. Byer, "Modeling and CW operation of a quasi-3-level 946 nm Nd-YAG laser," *IEEE Journal of Quantum Electronics*, vol. 23, pp. 605-612, May 1987.
- [2] B. Unal, M. C. Netti, M. A. Hassan, P. J. Ayliffe, M. D. B. Charlton, F. Lahoz, *et al.*, "Neodymium-doped tantalum pentoxide waveguide lasers," *Ieee Journal of Quantum Electronics*, vol. 41, pp. 1565-1573, Dec 2005.
- [3] B. Unal, C. Y. Tai, D. P. Shepherd, J. S. Wilkinson, N. M. B. Perney, M. C. Netti, *et al.*, "Nd : Ta2O5 rib waveguide lasers," *Applied Physics Letters*, vol. 86, Jan 2005.
- [4] A. Giesen and J. Speiser, "Fifteen years of work on thin-disk lasers: Results and scaling laws," *IEEE Journal of Selected Topics in Quantum Electronics*, vol. 13, pp. 598-609, May-Jun 2007.
- [5] D. J. Richardson, J. Nilsson, and W. A. Clarkson, "High power fiber lasers: current status and future perspectives," *Journal of the Optical Society of America B*, vol. 27, pp. B63-B92, Nov 2010.
- [6] C. Grivas, "Optically pumped planar waveguide lasers, Part I: Fundamentals and fabrication techniques," *Progress in Quantum Electronics*, vol. 35, pp. 159-239, Nov 2011.
- [7] J. I. Mackenzie, "Dielectric solid-state planar waveguide lasers: A review," *IEEE Journal of Selected Topics in Quantum Electronics*, vol. 13, pp. 626-637, May-Jun 2007.
- [8] Y. E. Romanyuk, C. N. Borca, M. Pollnau, S. Rivier, V. Petrov, and U. Griebner, "Yb-doped KY(WO4)2 planar waveguide laser," *Optics Letters*, vol. 31, pp. 53-55, 2006/01/01 2006.
- [9] M. Jelinek, "Progress in optical waveguiding thin films," *Czechoslovak Journal of Physics*, vol. 53, pp. 365-377, May 2003.

- [10] R. A. McFarlane, M. Lui, and D. Yap, "Rare-earth-doped fluoride wave-guides fabricated using molecular-beam epitaxy," *Ieee Journal of Selected Topics in Quantum Electronics*, vol. 1, pp. 82-91, Apr 1995.
- [11] M. R. Poulsen, P. I. Borel, J. Fage-Pedersen, J. Hubner, M. Kristensen, J. H. Povlsen, *et al.*, "Advances in silica-based integrated optics," *Optical Engineering*, vol. 42, pp. 2821-2834, Oct 2003.
- [12] J. Hübner, S. Guldberg-Kjaer, M. Dyngaard, Y. Shen, C. L. Thomsen, S. Balslev, *et al.*, "Planar Er- and Yb-doped amplifiers and lasers," *Applied Physics B*, vol. 73, pp. 435-438, 2001// 2001.
- [13] J. Haisma, N. Hattu, J. T. C. M. Pulles, E. Steding, and J. C. G. Vervest, "Direct bonding and beyond," *Applied Optics*, vol. 46, pp. 6793-6803, 2007/09/20 2007.
- [14] G. Spierings, J. Haisma, and T. M. Michielsens, "Surface-related phenomena in the direct bonding of silicon and fused-silica wafer pairs," *Philips Journal of Research*, vol. 49, pp. 47-63, 1995.
- [15] C. T. A. Brown, C. L. Bonner, T. J. Warburton, D. P. Shepherd, A. C. Tropper, D. C. Hanna, *et al.*, "Thermally bonded planar waveguide lasers," *Applied Physics Letters*, vol. 71, pp. 1139-1141, Sep 1997.
- [16] U. Griebner, R. Grunwald, and H. Schönnagel, "Thermally bonded Yb : YAG planar waveguide laser," *Optics Communications*, vol. 164, pp. 185-190, Jun 1999.
- [17] U. Griebner and H. Schönnagel, "Laser operation with nearly diffraction-limited output from a Yb:YAG multimode channel waveguide," *Optics Letters*, vol. 24, pp. 750-752, 1999/06/01 1999.
- [18] H. J. Baker, A. A. Chesworth, D. P. Millas, and D. R. Hall, "A planar waveguide Nd : YAG laser with a hybrid waveguide-unstable resonator," *Optics Communications*, vol. 191, pp. 125-131, May 2001.
- [19] J. R. Lee, H. J. Baker, G. J. Friel, G. J. Hilton, and D. R. Hall, "High-average-power Nd:YAG planar waveguide laser that is face pumped by 10 laser diode bars," *Optics Letters*, vol. 27, pp. 524-526, 04/01 2002.

- [20] Y. Liu, T.-H. Her, A. Dittli, and L. W. Casperson, "Continuous-wave hybrid index-antiguided and thermal-guided planar waveguide laser," *Applied Physics Letters*, vol. 103, p. 191103, 2013.
- [21] G. Stewart, C. A. Millar, P. J. R. Laybourn, C. D. W. Wilkinson, and R. M. Delarue, "Planar optical-waveguides formed by silver-ion migration in glass," *Ieee Journal of Quantum Electronics*, vol. 13, pp. 192-200, 1977.
- [22] T. G. Giallorenzi, E. J. West, R. Kirk, R. Ginther, and R. A. Andrews, "Optical Waveguides Formed by Thermal Migration of Ions in Glass," *Applied Optics*, vol. 12, pp. 1240-1245, 1973/06/01 1973.
- [23] M. Hempstead, J. S. Wilkinson, and L. Reekie, "Waveguide lasers operating at 1084 nm in neodymium-diffused lithium niobate," *IEEE Photonics Technology Letters*, vol. 4, pp. 852-855, 1992.
- [24] F. Chen, Y. Tan, and A. R ódenas, "Ion implanted optical channel waveguides in Er³⁺/MgO co-doped near stoichiometric LiNbO₃: a new candidate for active integrated photonic devices operating at 1.5 μm ," *Optics Express*, vol. 16, pp. 16209-16214, 2008/09/29 2008.
- [25] J. Siebenmorgen, K. Petermann, G. Huber, K. Rademaker, S. Nolte, and A. Tunnermann, "Femtosecond laser written stress-induced Nd:Y₃Al₅O₁₂ (Nd:YAG) channel waveguide laser," *Applied Physics B-Lasers and Optics*, vol. 97, pp. 251-255, Oct 2009.
- [26] W. F. Silva, C. Jacinto, A. Benayas, J. R. V. de Aldana, G. A. Torchia, F. Chen, *et al.*, "Femtosecond-laser-written, stress-induced Nd:YVO₄ waveguides preserving fluorescence and Raman gain," *Optics Letters*, vol. 35, pp. 916-918, Apr 2010.
- [27] J. Siebenmorgen, T. Calmano, K. Petermann, and G. Huber, "Highly efficient Yb:YAG channel waveguide laser written with a femtosecond-laser," *Optics Express*, vol. 18, pp. 16035-16041, 2010/07/19 2010.
- [28] D. P. Shepherd, S. J. Hettrick, C. Li, J. I. Mackenzie, R. J. Beach, S. C. Mitchell, *et al.*, "High-power planar dielectric waveguide lasers," *Journal of Physics D-Applied Physics*, vol. 34, pp. 2420-2432, Aug 2001.

- [29] J. I. Mackenzie, C. Li, D. P. Shepherd, H. E. Meissner, and S. C. Mitchell, "Longitudinally diode-pumped Nd:YAG double-clad planar waveguide laser," *Optics Letters*, vol. 26, pp. 698-700, 2001.
- [30] T. Bhutta, J. I. Mackenzie, and D. P. Shepherd, "Spatial dopant profiles for transverse-mode selection in multimode waveguides," *Journal of the Optical Society of America B*, vol. 19, pp. 1539-1543, Jul 2002.
- [31] D. C. Hanna, A. C. Large, D. P. Shepherd, A. C. Tropper, I. Chartier, B. Ferrand, *et al.*, "A side-pumped nd-yag epitaxial wave-guide laser," *Optics Communications*, vol. 91, pp. 229-235, Jul 1992.
- [32] T. Bhutta, J. I. Mackenzie, D. P. Shepherd, and R. J. Beach, "Spatial dopant profiles for transverse-mode selection in multimode waveguides," *Journal of the Optical Society of America B*, vol. 19, pp. 1539-1543, 2002/07/01 2002.
- [33] C. L. Bonner, T. Bhutta, D. P. Shepherd, and A. C. Tropper, "Double-clad structures and proximity coupling for diode-bar-pumped planar waveguide lasers," *IEEE Journal of Quantum Electronics*, vol. 36, pp. 236-242, Feb 2000.
- [34] L. Dong, H. A. McKay, A. Marcinkevicius, L. B. Fu, J. Li, B. K. Thomas, *et al.*, "Extending Effective Area of Fundamental Mode in Optical Fibers," *Journal of Lightwave Technology*, vol. 27, pp. 1565-1570, Jun 2009.
- [35] L. Redaelli, H. Wenzel, J. Piprek, T. Weig, S. Einfeldt, M. Martens, *et al.*, "Index-Antiguinding in Narrow-Ridge GaN-Based Laser Diodes Investigated by Measurements of the Current-Dependent Gain and Index Spectra and by Self-Consistent Simulation," *Ieee Journal of Quantum Electronics*, vol. 51, Aug 2015.
- [36] D. Jain, Y. Jung, P. Barua, S. Alam, and J. K. Sahu, "Demonstration of ultra-low NA rare-earth doped step index fiber for applications in high power fiber lasers," *Optics Express*, vol. 23, pp. 7407-7415, Mar 2015.
- [37] N. H. H. Weber, *Optical Resonators : Fundamentals, Advanced Concepts and Applications*: Springer, 2013.
- [38] C. A. Hill and D. R. Hall, "Coupling loss theory of single-mode waveguide resonators," *Applied Optics*, vol. 24, pp. 1283-1290, 1985/05/01 1985.

- [39] X. B. Wang, Q. Y. Xu, M. J. Xie, and Z. G. Li, "Coupling losses and mode properties in planar waveguide resonators," *Optics Communications*, vol. 131, pp. 41-46, Oct 1996.
- [40] U. Griebner and H. Schonngel, "Laser operation with nearly diffraction-limited output from a Yb : YAG multimode channel waveguide," *Optics Letters*, vol. 24, pp. 750-752, Jun 1999.
- [41] K. Gallo and G. Assanto, "All-optical diode based on second-harmonic generation in an asymmetric waveguide," *Journal of the Optical Society of America B-Optical Physics*, vol. 16, pp. 267-269, Feb 1999.
- [42] K. Okamoto, *Fundamentals of Optical Waveguides*: Academic Press, 2000.
- [43] C. Jauregui, J. Limpert, and A. Tunnermann, "High-power fibre lasers," *Nat Photon*, vol. 7, pp. 861-867, 11/print 2013.
- [44] M.-J. Li, X. Chen, A. Liu, S. Gray, J. Wang, D. T. Walton, *et al.*, "Limit of Effective Area for Single-Mode Operation in Step-Index Large Mode Area Laser Fibers," *Journal of Lightwave Technology*, vol. 27, pp. 3010-3016, Aug 1 2009.
- [45] J. Limpert, A. Liem, M. Reich, T. Schreiber, S. Nolte, H. Zellmer, *et al.*, "Low-nonlinearity single-transverse-mode ytterbium-doped photonic crystal fiber amplifier," *Optics Express*, vol. 12, pp. 1313-1319, 2004.
- [46] J. Limpert, T. Schreiber, S. Nolte, H. Zellmer, A. Tunnermann, R. Iliew, *et al.*, "High-power air-clad large-mode-area photonic crystal fiber laser," *Optics Express*, vol. 11, pp. 818-823, Apr 2003.
- [47] J. Limpert, N. D. Robin, I. Manek-Honninger, F. Salin, F. Roser, A. Liem, *et al.*, "High-power rod-type photonic crystal fiber laser," *Optics Express*, vol. 13, pp. 1055-1058, Feb 2005.
- [48] X. Ma, C. Zhu, I. N. Hu, A. Kaplan, and A. Galvanauskas, "Single-mode chirally-coupled-core fibers with larger than 50 μm diameter cores," *Optics Express*, vol. 22, pp. 9206-9219, 2014/04/21 2014.

- [49] F. Stutzki, F. Jansen, H. J. Otto, C. Jauregui, J. Limpert, and A. Tunnermann, "Designing advanced very-large-mode-area fibers for power scaling of fiber-laser systems," *Optica*, vol. 1, pp. 233-242, Oct 2014.
- [50] J. Limpert, O. Schmidt, J. Rothhardt, F. Rösler, T. Schreiber, A. Tünnermann, *et al.*, "Extended single-mode photonic crystal fiber lasers," *Optics Express*, vol. 14, pp. 2715-2720, 2006.
- [51] J. R. Marciante, "Gain Filtering for Single-Spatial-Mode Operation of Large-Mode-Area Fiber Amplifiers," *IEEE Journal of Selected Topics in Quantum Electronics*, vol. 15, pp. 30-36, Jan-Feb 2009.
- [52] A. E. Siegman, "Propagating modes in gain-guided optical fibers," *Journal of the Optical Society of America A*, vol. 20, pp. 1617-1628, Aug 2003.
- [53] Y. Chen, T. McComb, V. Sudesh, M. Richardson, and M. Bass, "Very large-core, single-mode, gain-guided, index-antiguidded fiber lasers," *Optics Letters*, vol. 32, pp. 2505-2507, Sep 2007.
- [54] A. E. Siegman, Y. Chen, V. Sudesh, M. C. Richardson, M. Bass, P. Foy, *et al.*, "Confined propagation and near single-mode laser oscillation in a gain-guided, index antiguided optical fiber," *Applied Physics Letters*, vol. 89, p. 251101, Dec 2006.
- [55] A. E. Siegman, "Gain-guided, index-antiguidded fiber lasers," *Journal of the Optical Society of America B*, vol. 24, pp. 1677-1682, Aug 2007.
- [56] V. Sudesh, T. McComb, Y. Chen, M. Bass, M. Richardson, J. Ballato, *et al.*, "Diode-pumped 200 μm diameter core, gain-guided, index-antiguidded single mode fiber laser," *Applied Physics B*, vol. 90, pp. 369-372, Mar 2008.
- [57] W. Hageman, Y. Chen, X. Wang, L. Gao, G. U. Kim, M. Richardson, *et al.*, "Scalable side-pumped, gain-guided index-antiguidded fiber laser," *Journal of the Optical Society of America B*, vol. 27, pp. 2451-2459, 2010.
- [58] W. N. Li, M. Lu, Z. Yang, H. T. Guo, P. F. Wang, and B. Peng, "Fabrication and characterization of Yb³⁺-doped gain-guided index-antiguidded fiber with D-shaped inner cladding," *Journal of the Optical Society of America B-Optical Physics*, vol. 28, pp. 1498-1501, Jun 2011.

- [59] M. Lu, W. Li, K. Zou, S. Dai, W. Wei, and B. Peng, "Yb³⁺-doped 200 μm diameter core, gain guided index-antiguidded fiber," *Applied Physics B*, vol. 98, pp. 301-304, Feb 2010.
- [60] P. G. Yarandi, S. Karbasi, and A. Mafi, "Improving the Power Efficiency in End-Pumped Gain-Guided Index-Antiguidded Fiber Amplifiers," *Journal of Lightwave Technology*, vol. 30, pp. 3203-3210, 2012.
- [61] Y. Zhu, K. Duan, H. Shao, B. Zhao, E. Zhang, and W. Zhao, "Theoretical analysis of output performance of GG-IAG fiber laser by multipoint distributed side pump," *Optics Communications*, vol. 285, pp. 5359-5363, 11/1/ 2012.
- [62] X. Shen, W. Wei, H. Zou, and L. L. Zhang, "Analysis of dual-end-pumped Nd³⁺-doped index-crossover gain guided-index antiguidded fiber laser," *Optics Communications*, vol. 366, pp. 205-209, May 2016.
- [63] X. Shen, H. Zou, H. T. Tang, and W. Wei, "Threshold characteristics analysis of a uniformly side-pumped Yb³⁺-doped gain-guided and index-antiguidded fiber laser," *Optics and Laser Technology*, vol. 68, pp. 1-5, May 2015.
- [64] Y. Chen, V. Sudesh, T. McComb, M. C. Richardson, M. Bass, and J. Ballato, "Lasing in a gain-guided index antiguidded fiber," *Journal of the Optical Society of America B-Optical Physics*, vol. 24, pp. 1683-1688, Aug 2007.
- [65] W. Koechner, *Solid-State Laser Engineering Sixth Revised and Updated Edition*. New York, NY: Springer Science, Inc, 2006.
- [66] F. Mitschke, *Fiber optics*. Germany: Springer, 2009.
- [67] A. E. Siegman, *Lasers*. CA: University Science, 1986.
- [68] M. B. E. Wolf, *Principle of Optics: 7th edition*, 7th ed. UK: Cambridge University Press, 2001.
- [69] P. Y. Amnon Yariv, *Optical waves in crystals*. USA: John Wiley & Sons, 1984.
- [70] K. M. Gundu, P. G. Yarandi, and A. Mafi, "Beam-quality factor of single-mode gain-guided fiber lasers," *Optics Letters*, vol. 35, pp. 4124-4126, Dec 2010.

- [71] P. G. Yarandi, K. M. Gundu, and A. Mafi, "On the beam profile and beam quality of gain-guided index-antiguided fibers with finite cladding boundary," *Journal of the Optical Society of America B*, vol. 28, pp. 2430-2435, 2011/10/01 2011.
- [72] R. F. Cregan, B. J. Mangan, J. C. Knight, T. A. Birks, P. S. Russell, P. J. Roberts, *et al.*, "Single-mode photonic band gap guidance of light in air," *Science*, vol. 285, pp. 1537-1539, Sep 1999.
- [73] L. Lavoute, P. Roy, A. Desfarges-Berthelemot, V. Kermene, and S. Fevrier, "Design of microstructured single-mode fiber combining large mode area and high rare earth ion concentration," *Optics Express*, vol. 14, pp. 2994-2999, Apr 2006.
- [74] P. Russell, "Photonic crystal fibers," *Science*, vol. 299, pp. 358-362, Jan 2003.
- [75] L. Dong, X. Peng, and J. Li, "Leakage channel optical fibers with large effective area," *Journal of the Optical Society of America B-Optical Physics*, vol. 24, pp. 1689-1697, Aug 2007.
- [76] L. W. Casperson and T.-H. Her, "Thermal refraction focusing in very-large-core step-index antiguided fiber lasers," *Journal of the Optical Society of America B*, vol. 30, pp. 3095-3101, 2013/12/01 2013.
- [77] L. W. Casperson and T.-H. Her, "Thermal refraction defocusing in very-large-core step-index antiguided fiber lasers," *Journal of the Optical Society of America B*, vol. 31, pp. 2858-2863, 2014/11/01 2014.
- [78] L. W. Casperson, A. Dittli, and T. H. Her, "Thermal refraction focusing in planar index-antiguided lasers," *Optics Letters*, vol. 38, pp. 929-931, Mar 2013.
- [79] E. Hartl and G. Muller, "Transition from Gain Guiding to Index Guiding and Characterization of 1.55- μ m Bridge-Contacted Ridge-Wave-Guide Lasers," *IEE Proceedings-J Optoelectronics*, vol. 134, pp. 22-26, Feb 1987.
- [80] L. Casperson and A. Yariv, "The Gaussian mode in optical resonators with a radial gain profile," *Applied Physics Letters*, vol. 12, pp. 355-357, 1968.
- [81] J. Hu and C. R. Menyuk, "Understanding leaky modes: slab waveguide revisited," *Advances in Optics and Photonics*, vol. 1, pp. 58-106, 2009/01/01 2009.

- [82] L. W. Casperson, "Beam modes in complex lenslike media and resonators," *Journal of the Optical Society of America*, vol. 66, pp. 1373-1379, 1976.
- [83] T. Y. Fan, "Heat generation in Nd:YAG and Yb:YAG," *IEEE Journal of Quantum Electronics*, vol. 29, pp. 1457-1459, 1993.
- [84] M. Abramowitz and I. A. Stegun, Eds., *Handbook of Mathematical Functions with Formulas, Graphs, and Mathematical Tables* (National Bureau of Standards Applied Mathematics Series 55. U.S. Government Printing Office, Washington, D.C., 1970, p.[^]pp. Pages.
- [85] H. Kogelnik, "On the Propagation of Gaussian Beams of Light Through Lenslike Media Including those with a Loss or Gain Variation," *Applied Optics*, vol. 4, pp. 1562-1569, 12/01 1965.
- [86] L. W. Casperson, "Gaussian light-beams in inhomogeneous media," *Applied Optics*, vol. 12, pp. 2434-2441, 1973.
- [87] L. W. Casperson, "Laser power calculations - sources of error," *Applied Optics*, vol. 19, pp. 422-434, 1980.
- [88] P. F. Moulton, "An investigation of the co-mgf2 laser system," *IEEE Journal of Quantum Electronics*, vol. 21, pp. 1582-1595, 1985 1985.
- [89] W. P. Risk, "Modeling of longitudinally pumped solid-state lasers exhibiting reabsorption losses," *Journal of the Optical Society of America B*, vol. 5, pp. 1412-1423, Jul 1988.
- [90] D. G. Hall, R. J. Smith, and R. R. Rice, "Pump-size effects in Nd:YAG lasers," *Applied Optics*, vol. 19, pp. 3041-3043, 1980/09/15 1980.
- [91] M. J. F. Digonnet and C. J. Gaeta, "Theoretical analysis of optical fiber laser amplifiers and oscillators," *Applied Optics*, vol. 24, pp. 333-342, 02/01 1985.
- [92] K. Kubodera and K. Otsuka, "Laser performance of a glass-clad lindp 4o12 rectangular wave-guide," *Journal of Applied Physics*, vol. 50, pp. 6707-6712, 1979.

- [93] S. D. Jackson and T. A. King, "Theoretical modeling of Tm-doped silica fiber lasers," *Journal of Lightwave Technology*, vol. 17, pp. 948-956, May 1999.
- [94] H. Shu, Y. Chen, M. Bass, J. F. Monjardin, and J. Deile, "Numerical modeling of alkali vapor lasers," *Optics Express*, vol. 19, pp. 19875-19885, Oct 2011.
- [95] Y. G. Zhu, K. L. Duan, H. M. Shao, B. Y. Zhao, E. T. Zhang, and W. Zhao, "Theoretical analysis of output performance of GG-IAG fiber laser by multipoint distributed side pump," *Optics Communications*, vol. 285, pp. 5359-5363, Nov 2012.
- [96] R. Gerlach, D. Wei, and N. M. Amer, "Coupling efficiency of waveguide laser resonators formed by flat mirrors - analysis and experiment," *IEEE Journal of Quantum Electronics*, vol. 20, pp. 948-963, 1984.
- [97] J. L. Boulnois and G. P. Agrawal, "Mode-discrimination and coupling losses in rectangular-waveguide resonators with conventional and phase-conjugate mirrors," *Journal of the Optical Society of America*, vol. 72, pp. 853-860, 1982.
- [98] Y. Liu, L. W. Casperson, and T.-H. Her, "Transverse mode competition in index-antiguided waveguide lasers," *Applied Physics Letters*, vol. 107, Dec 14 2015.
- [99] C. Wang, T. H. Her, L. Zhao, X. Ao, L. W. Casperson, C. H. Lai, *et al.*, "Gain Saturation and Output Characteristics of Index-Antiguided Planar Waveguide Amplifiers With Homogeneous Broadening," *Journal of Lightwave Technology*, vol. 29, pp. 1958-1964, 2011.
- [100] W. W. Rigrod, "Homogeneously broadened cw lasers with uniform distributed loss," *IEEE Journal of Quantum Electronics*, vol. 14, pp. 377-381, 1978 1978.
- [101] J. I. Mackenzie, C. Li, and D. P. Shepherd, "Multi-watt, high efficiency, diffraction-limited Nd : YAG planar waveguide laser," *IEEE Journal of Quantum Electronics*, vol. 39, pp. 493-500, Mar 2003.
- [102] W. F. Krupke, "Ytterbium solid-state lasers - The first decade," *IEEE Journal of Selected Topics in Quantum Electronics*, vol. 6, pp. 1287-1296, Nov-Dec 2000.

- [103] E. A. J. Marcatili and R. A. Schmelzter, "Hollow metallic and dielectric waveguides for long distance optical transmission and lasers," *Bell System Technical Journal*, vol. 43, pp. 1783-1809, 1964.
- [104] J. J. Degnan and D. R. Hall, "Finite aperture waveguide laser resonators," *IEEE Journal of Quantum Electronics*, vol. QE 9, pp. 901-910, 1973 1973.
- [105] J. Degnan, "The waveguide laser: A review," *Applied Physics*, vol. 11, pp. 1-33, 1976/09/01 1976.
- [106] A. W. Snyder, "Coupled-Mode Theory for Optical Fibers," *Journal of the Optical Society of America*, vol. 62, pp. 1267-1277, 1972/11/01 1972.
- [107] S. Wielandy, "Implications of higher-order mode content in large mode area fibers with good beam quality," *Optics Express*, vol. 15, pp. 15402-15409, Nov 2007.
- [108] M. F. C. Schemmann, C. J. Vanderpoel, B. A. H. Vanbakel, H. Ambrosius, A. Valster, J. A. M. Vandenheijkant, *et al.*, "Kink power in weakly index-guided semiconductor-lasers," *Applied Physics Letters*, vol. 66, pp. 920-922, Feb 1995.
- [109] X. R. Wang, Y. Chen, W. Hageman, G. U. Kim, M. Richardson, C. D. Xiong, *et al.*, "Transverse mode competition in gain-guided index antiguided fiber lasers," *Journal of the Optical Society of America B*, vol. 29, pp. 191-196, Feb 2012.
- [110] R. L. Abrams, "Coupling losses in hollow waveguide laser resonators," *IEEE Journal of Quantum Electronics*, vol. QE 8, pp. 838-&, 1972.
- [111] S. Avriillier and J. Verdonck, "Coupling losses in laser resonators containing a hollow rectangular dielectric waveguide," *Journal of Applied Physics*, vol. 48, pp. 4937-4941, 1977.
- [112] H. Kogelnik and T. Li, "Laser Beams and Resonators," *Applied Optics*, vol. 5, pp. 1550-1567, 10/01 1966.
- [113] J. Goodman, *Introduction to Fourier Optics*. Englewood, Colorado: Roberts & Company Publisher, 2013.

- [114] J. W. Goodman, *Introduction to Fourier Optics*, the second edition ed.: The McGraw-Hill Companies, INC., 1988.
- [115] W. W. Rigrod, "Gain saturation and output power of optical masers," *Journal of Applied Physics*, vol. 34, pp. 2602-2609, 1963.
- [116] C. Wang, T.-H. Her, L. Zhao, X. Ao, L. W. Casperson, C.-H. Lai, *et al.*, "Gain Saturation and Output Characteristics of Index-Antiguidded Planar Waveguide Amplifiers With Homogeneous Broadening," *Journal of Lightwave Technology*, vol. 29, pp. 1958-1964, Jul 1 2011.
- [117] J. H. Campbell and T. I. Suratwala, "Nd-doped phosphate glasses for high-energy/high-peak-power lasers," *Journal of Non-Crystalline Solids*, vol. 263, pp. 318-341, Mar 2000.
- [118] Y. Yoshida, M. Sasaki, K. Shibata, Z. Kawazu, K. I. Ono, H. Nishiguchi, *et al.*, "Kink and power saturation of 660-nm AlGaInP laser diodes," *IEEE Journal of Quantum Electronics*, vol. 41, pp. 828-832, Jun 2005.
- [119] M. Achtenhagen, A. A. Hardy, and C. S. Harder, "Coherent kinks in high-power ridge waveguide laser diodes," *Journal of Lightwave Technology*, vol. 24, pp. 2225-2232, May 2006.
- [120] M. Buda, H. H. Tan, L. Fu, L. Josyula, and C. Jagadish, "Improvement of the kink-free operation in ridge-waveguide laser diodes due to coupling of the optical field to the metal layers outside the ridge," *IEEE Photonics Technology Letters*, vol. 15, pp. 1686-1688, Dec 2003.
- [121] R. Gordon and J. Xu, "Lateral mode dynamics of semiconductor lasers," *IEEE Journal of Quantum Electronics*, vol. 35, pp. 1904-1911, Dec 1999.
- [122] A. Choudhary, S. J. Beecher, S. Dhingra, B. D'Urso, T. L. Parsonage, J. A. Grant-Jacob, *et al.*, "456-mW graphene Q-switched Yb:yttria waveguide laser by evanescent-field interaction," *Optics Letters*, vol. 40, pp. 1912-1915, 2015/05/01 2015.
- [123] A. Choudhary, S. Dhingra, B. D'Urso, T. L. Parsonage, K. A. Sloyan, R. W. Eason, *et al.*, "Q-switched operation of a pulsed-laser-deposited Yb:Y2O3 waveguide using graphene as a saturable absorber," *Optics Letters*, vol. 39, pp. 4325-4328, 2014/08/01 2014.

- [124] R. Mary, G. Brown, S. J. Beecher, F. Torrisi, S. Milana, D. Popa, *et al.*, "1.5 GHz picosecond pulse generation from a monolithic waveguide laser with a graphene-film saturable output coupler," *Optics Express*, vol. 21, pp. 7943-7950, 2013/04/08 2013.
- [125] Y. Tan, S. Akhmadaliev, S. Zhou, S. Sun, and F. Chen, "Guided continuous-wave and graphene-based Q-switched lasers in carbon ion irradiated Nd:YAG ceramic channel waveguide," *Optics Express*, vol. 22, pp. 3572-3577, 2014/02/10 2014.
- [126] A. G. Okhrimchuk and P. A. Obraztsov, "11-GHz waveguide Nd:YAG laser CW mode-locked with single-layer graphene," *Scientific Reports*, vol. 5, p. 11172, 06/08/online 2015.
- [127] J. Wang, Z. Luo, M. Zhou, C. Ye, H. Fu, Z. Cai, *et al.*, "Evanescent-Light Deposition of Graphene Onto Tapered Fibers for Passive Q-Switch and Mode-Locker," *IEEE Photonics Journal*, vol. 4, pp. 1295-1305, 2012.
- [128] T.-H. Her, X. Ao, and L. W. Casperson, "Gain saturation in gain-guided slab waveguides with large-index antiguiding," *Optics Letters*, vol. 34, pp. 2411-2413, 2009.
- [129] J. D. Zapata, D. Steinberg, L. A. M. Saito, R. E. P. de Oliveira, A. M. Cárdenas, and E. A. T. de Souza, "Efficient graphene saturable absorbers on D-shaped optical fiber for ultrashort pulse generation," *Scientific Reports*, vol. 6, p. 20644, 02/09/online 2016.
- [130] A. Martinez and Z. Sun, "Nanotube and graphene saturable absorbers for fibre lasers," *Nature Photonics*, vol. 7, pp. 842-845, 11/print 2013.
- [131] J. Du, Q. Wang, G. Jiang, C. Xu, C. Zhao, Y. Xiang, *et al.*, "Ytterbium-doped fiber laser passively mode locked by few-layer Molybdenum Disulfide (MoS₂) saturable absorber functioned with evanescent field interaction," *Scientific Reports*, vol. 4, p. 6346, 09/12/online 2014.
- [132] H. Zhang, S. B. Lu, J. Zheng, J. Du, S. C. Wen, D. Y. Tang, *et al.*, "Molybdenum disulfide (MoS₂) as a broadband saturable absorber for ultra-fast photonics," *Optics Express*, vol. 22, pp. 7249-7260, 2014/03/24 2014.
- [133] M. F. C. Schemmann, C. J. van der Poel, B. A. H. van Bakel, H. P. M. M. Ambrosius, A. Valster, J. A. M. van den Heijkant, *et al.*, "Kink power in weakly

index guided semiconductor lasers," *Applied Physics Letters*, vol. 66, pp. 920-922, 1995.

APPENDIX A SCANNING FABRY PEROT INTERFEROMETER

A.1.1 Introduction

Determination the spectral of the light source is of great importance for applications where its spectral plays an important role. The conventional approach is to employ dispersion elements, such as prism or diffraction gratings, to separate the different wavelength either in spatial domain or in time domain. It works for black-body based light sources since black-body radiation results in a broad spectral. However, due to resonation, the spectral of the laser has equally spaced spikes with a Lorentz or Gaussian shape envelope. The spikes are often referred as longitudinal mode, which has a very narrow linewidth (around MHz level). The envelope can be measured with dispersion spectrometer whose spectral resolution is around sub-nanometer level. To resolve finer longitudinal mode structure, the interferometric method is preferred. Due to its compact size and high spectral resolution, Fabry-Perot interferometry is often used. Further improvement towards automation is made by using piezo actuator to change the cavity mirror separation. This instrument is often referred as scanning Fabry-Perot spectrum analyzer (SFPI) and is widely used in both characterizing ultra fine spectral structures and serving as a tunable filter.

In this note, the home-build SFPI is documented. The principle of SFPI is firstly introduced first. Then the setup will be explained in detail. More instrument response curve is measured with an ultra narrow linewidth external cavity diode laser (ECL). Finally, the

measurement result of the index-antiguided (IAG) planar waveguide laser will be included.

A.1.2 Principle

The Fabry-Perot interferometer (FPI) consists of two reflective mirrors which are separated with a fixed distance. The constructive interference results in multiple transmission peaks in frequency domain as shown in Fig. A-1.

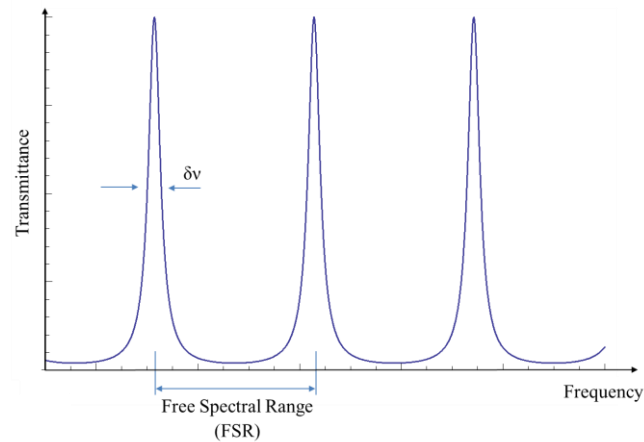


Figure A-1. The transmission curve of the FPI in frequency domain

The spectral separation between two adjacent peaks is referred as free spectral range (FSR) described as

$$FSR = \frac{c}{2L}, \quad (1.1)$$

where c is the speed of light in vacuum; L is the separation of the two cavity mirrors. The width (FWHM) of each individual peak is expressed as $\delta\nu$. The ratio between FSR and $\delta\nu$ is called finesse (F) and is related with the reflectivity of cavity mirrors:

$$F = \frac{FSR}{\delta\nu} = \frac{\pi\sqrt{R_1R_2}}{1-R_1R_2}, \quad (1.2)$$

where R_1 and R_2 are the intensity reflectivity of the left and right cavity mirror respectively. As shown, the spectral response of a FPI is determined by the length of the cavity and the reflectivity of the cavity mirrors. In order to scan, the separation of the cavity mirrors need to vary slightly. The movement of the transmission peaks samples through the incident unknown spectrum, which is reflected by the transmitted signal of the interferometer. In order to avoid spectrum overlap, the FSR of FPI should be larger than the spectrum under test such that only one transmission peak is used when scanning.

A.1.3 Setups

To remove the cross coupling between transverse mode and longitudinal mode, two identical plano-concave high reflectors are used as the cavity mirrors and the separation is set to be the same as its radius of curvature. This configuration is called confocal resonator where all the longitudinal modes excited due to transverse mode are degenerated. The confocal configuration also reduces the alignment complexity when coupling light into

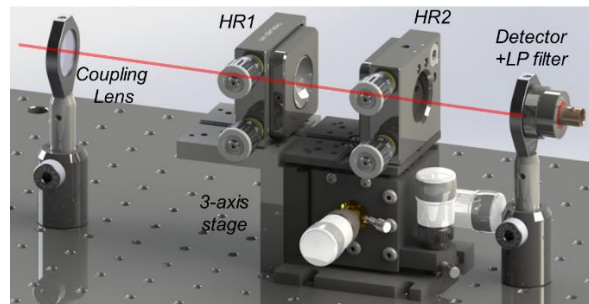


Figure A-2. Schematic diagram of the home-built SFPI, the red line denotes the incident beam; HR: curved high reflector; LP filter: long pass filter @ 1000 nm.

SFPI, which may otherwise require extensive effort. The schematic diagram is given in Fig.A-2.

The radius curvature of the high reflector is 50 mm, which is the separation between two cavity mirrors. Two mirror mounts are epoxied on a 3-axis translation stage. The stage has 3 piezo actuators to control the motion along each the axis. A long-pass filter (cut-off wavelength = 1000 nm) is used to filter out the background light. A fast PIN detector is used to capture the transmitted signal. The calculated mirror finesse is 784.6 and the FSR is calculated to be 1.5 GHz. $\delta\nu$ is then determined to be around 2 MHz, which is the minimum value can be obtained. It is worth noting that the parameters given above are calculated based on ideal condition. Other factors such as imperfection of curved surface, cavity misalignment will lead to the reduction of the total finesse. A more direct consequence is that $\delta\nu$ will become larger.

When scanning, a function generator is used as shown in figure 3. The function generator provides a triangle wave to the piezo driver (PZT amplifier in figure 3), which is then translated into the linear motion of the stage. Due to the limited bandwidth of the piezo

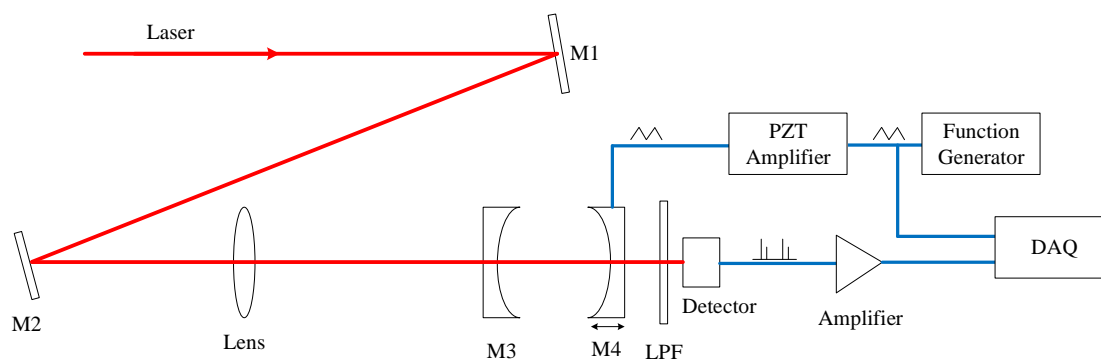


Figure A-3. Scanning setup configuration of SFPI

actuator, some nonlinearity is expected around the turning points of the triangle wave. The amplified detector signal together with the triangle voltage are acquired by NI DAQ.

A.1.4 Instrumental response curve

An external cavity diode laser (ECL) is used to measure the instrumental response curve of the SFPI. The ECL is lasing at 1064 nm with single longitudinal mode, the linewidth of which is 100 kHz. Since it is one order of magnitude smaller than the minimal δv , the transmitted signal represents the response of the SFPI. The scanning triangle wave and the captured transmitted intensity signals are given in Fig. A-4. The results show a periodic sharp peaks. The separation represents the FSR, which is 1.5 GHz. This data is used to calculate the convert unit, which in this experiment is 0.02309 MHz/ μ s. The individual peak is zoomed in and shown in Fig. A-5.

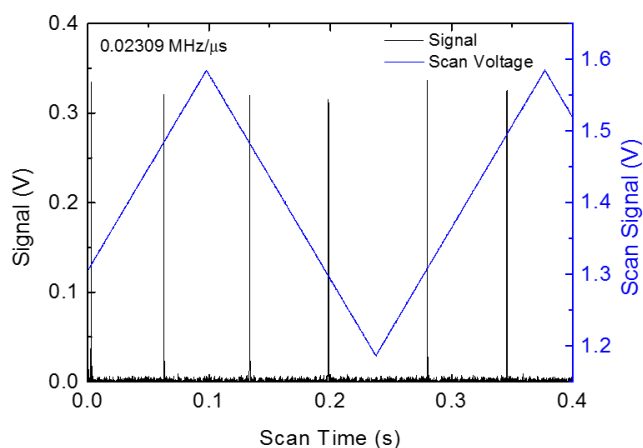


Figure A-4. The scanning triangle wave and transmitted intensity signal. The data is acquisition rate is 40 kHz.

The resolution of the SFPI is 4 MHz, which is larger than the theoretical value. As mentioned in previous section, this could be because of the reduction of finesse due to cavity

misalignment or mirror defects. Though it could be improved, yet extensive alignment will be necessary which renders the practicability. Another important information has to be tested before any useful measurement could be taken, which is the scanning range with different peak-to-peak (p-p) voltage value of triangle wave. Larger spectral range is scanned when the p-p voltage is increased. The corresponding more equally spaced spikes is used to calculate the exact spectral range scanned. The result is given in Fig. A-6. The

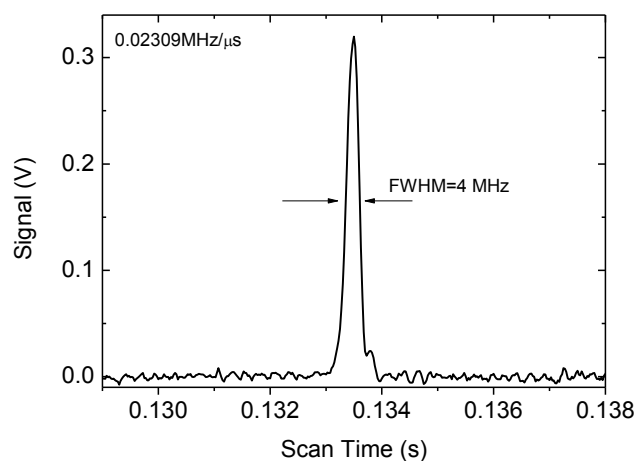


Figure A-5. Individual instrument response spike measured with ECL. The width (FWHM) is measured to be 4 MHz.

scan rate is 8.69 GHz/V. Finally, the overall specification of the SFPI is summarized in table A-1.

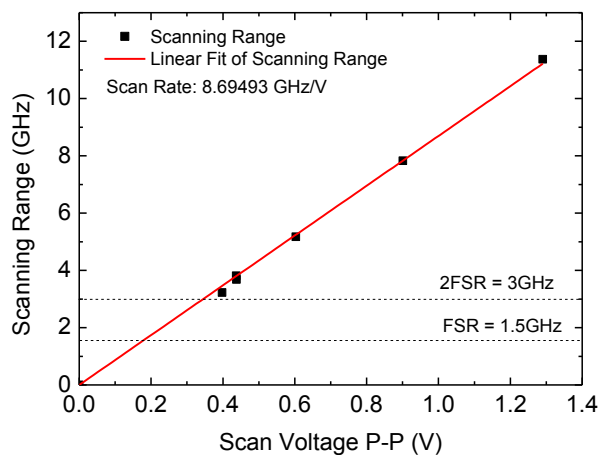


Figure A-6. Scanning ranges at different scanning p-p voltage. The horizontal dash lines represents the spectral ranges of one FSR and two FSRs respectively. The scan rate is determined to be 8.69 GHz/V

Table A-1. Specification of the home-built SFPI

Configuration	Confocal
Cavity length	50 mm
Cavity mirror radius of curvature	50 mm (concave)
Cavity reflectivity	> 99.8%
Working wavelength	1064 nm
Free spectral range (FSR)	1.5 GHz
$\delta\nu$	4 MHz
Mirror finesse	1569
Scan rate	8.69 GHz/V